Stick-Slip Friction

Håkon Nordhagen

Thesis submitted for the degree of
Candidatus Scientiarum

Department of Phyiscs
University of Oslo

January 2003

Acknowledgments

The work presented in this thesis was carried out in the Condensed Matter Group at the Department of Physics, University of Oslo during the period 2000-2002. This research group has also been a part of the Cooperative Phenomena Program initiated by Professor Torstein Fossan Jøssang and my supervisor, Professor Jens G. Feder, in 1973.

One decade ago, Jens Feder presented the original idea behind the experiments in this thesis. My motivation for carrying out these experiments came after a lecture in statistical mechanics held by Professor Feder. As we strolled down the hall after the lecture, he started to talk about a wonderful experiment using a carpet and a sandpaper, mentioning words like "self-organized criticality" and "earthquakes," which at that time I knew almost nothing about.

Jens's creativity and sometimes rather unusual way of attacking scientific problems (or problems in general), has been a great inspiration to me. Throughout my work in this group I've not only learned about cooperative effects in physical systems, but also gained insight, through Jens and Torstein, into the crucial and important cooperative phenomenon between academia and industry.

During the period when most of the experiments and simulations in this thesis were worked out, I had the pleasure of collaborating with Wesley Andrés Watters Farfán who at that time was a Fullbright Fellow from the USA. Wesley has during these years taught me a lot about everything, and deserves a lot of credit for bringing this thesis to print.

I would also like to thank the following persons Anders-Malthe Sørenssen, Thomas Walmann, Espen Jettestuen, Dag Dysthe, Joakim Bergli and Renaud Toussaint for their help and enthusiasm for my project.

The final credit goes to my *wonderful* girlfriend, who has supplied the most important content of my life.

Abstract

The primary goal of the work in this thesis was to investigate the macroscopic and microscopic nature of dry contact friction at very low velocities. Experiments were carried out using a sandpaper and carpet as contacting surfaces. The force required to pull the sandpaper across the carpet was recorded and analyzed on a computer. The very low speed at which the sandpaper was pulled (10-100 microns per second) gave rise to a so called stick-slip motion. That is, the motion of the sandpaper consists of varying distance and time. The distributions of both jumps and duration times were found to follow power-laws spanning up to 3 orders of magnitude. A scaling relation between event duration time and event magnitude has also been found. An analytic relation between the scaling exponents is found, and the experiments are found to follow this relation. The statistical independence of the events is supported by the agreement between theory and the experiment for the time between events of a given magnitude. These properties of the system are often taken as signs of Self-Organized Criticality (SOC), which is a category of non-equilibrium dynamical systems where the complex behavior, both in space and time, can be described statistically with power laws with non trivial exponents. By varying parameters such as the normal force, sandpaper coarseness and the elasticity of the system we have investigated how the statistics of the events are affected. However, no (clear) additional scaling laws, such a finite-size scaling, have been observed in the experiments. This raises questions about criticality of the system.

The force released when a single carpet fiber snaps is often too small for the resolution in the force measurements, but the sound is easily heard. Using a microphone and a sound card we are able to resolve these very fine details of the friction process.

We have also found a way of imaging the real contact area between the surfaces: by using an infrared camera and a transparent grid as a surface, we are able to see where the contact occurred because of the heat generated when there is a slip. We have not directly used the information collected using these two methods, but rather showed their potential if they are further developed.

Simulations were carried out to test whether our theories about the microscopic processes could lead to the macroscopic behavior observed in the experiments. We have come up with a stochastic model where each contact point between the surfaces are connected with springs of individual strength thresholds. The crucial ingredient in our model compared to other models is that

whenever a spring is stretched longer than its threshold allows, the force, or the elastic energy, is spread globally to all other contact points. This can lead to avalanches of breaking springs if sufficiently many springs are close enough to their threshold. We believe this kind of avalanche is what happens during a slip. Results from the simulations show distributions of avalanche size following a power law with exponents close to what we get from experiments. A numerical model for halting events in stick-slip motion is also presented. This model describes the halting of events that are relatively short lasting, but where the motion of the slider during a slip is considerable.

Contents

Chapter 1

Introduction

Friction represents a universal attitude of matter, and has always raised challenges to mankind. Even though evolution 'has known' for millions of years how to manage friction for its own benefit, for example joints supplied by liquid lubricants, it took a long time before any species took direct practical advantage of friction.

The first practical use of friction probably took place about 100 000 years ago, when frictional heating was used as a tool for making fire. A surviving portion of a potter's wheel with a pivot hole smoothed with bitumen dated at 3 500 B.C, shows that the "practical laws" of friction have been known for a long time [1].

Little academic interest in friction existed until the 15th century. Leonardo da Vinci suggested that friction was proportional to the normal load, but independent of the apparent area of contact. He introduced the concept of the coefficient of friction, μ, as the ratio of friction force F to normal load N. That is $\mu = F/N$. Leonardo concluded that for "polished and smooth" surfaces, "every frictional body has a resistance of friction equal to one-quarter of its weight". Although this general result is incorrect, the realistic value of μ for the materials he used might not have been far from 0.25.

Amontons (1699) [2], Coulomb (1785) and Morin (1833) all reached Leonardo's conclusions, but novel questions about friction were asked :

- Does friction depend on the type of surface or the velocity ?
- Does the time of contact influence the friction ?
- Why is the friction independent on the apparent area of contact ?

The purely empirical friction laws stated by Amontons-Coulomb were not explained until 1950 when Bowden and Tabor proposed a "microscopic" interpretation of friction [3]. They found that the apparent contact area was larger than the real area of contact, which alone determined the magnitude of the friction force. The real area of contact was also shown to be proportional to the

normal force. That is, the microscopic irregularities of the surfaces, also called asperities (a term introduced by Coulomb), touch and push into each other, and the sum of these contact points is the real contact area. The adhesive (or cohesive) forces [1] acting between the contact points was believed to be the main cause of friction. Friction has later been found to be related to the irreversible process of bringing asperities together and deforming them, and then separating them again. Despite this finding, no explicit physical mechanism for friction was proposed.

With the invention of the "surface force apparatus" and the "atomic force microscope" in the last 30 years, it has been possible to directly study both the mechanisms of friction at the atomic scale, and the topology of apparently smooth surfaces. Even though these technological advances have brought science closer to a detailed understanding friction, there is still a big knowledge-gap between understanding friction at the microscopic scale and understanding friction at the macroscopic scale. For example, nobody has so far been able to compute μ, given the details about the materials in contact. James A. Greenwood, a professor in physics and a well known person among tribologists, summed up the situation in 1992 when he wrote, "If some clever person would explain why friction exists, and is proportional to the true area of contact, our problem would be solved".

It remains of fundamental interest to find out how the collective behavior of all the asperities in contact gives rise to the most common, well-defined macroscopic friction laws. By addressing the two first questions posed by Coulomb and Amontons, we encounter the main topic of this thesis: at low sliding velocities there is no well-defined μ, and the friction may consists of a mixture of static and dynamic friction, called stick-slip friction. Squeaking doors and the sound produced when sliding the bow on a violin are good examples of regular stick-slip motion. A candidate for more irregular stick-slip friction is the dynamics of earthquakes. Here the periods of stick represents the time where stress is being built up around borders of continental plates, and slips events are expressed through sudden movement of the earth's crust. Amontons and Coulomb assumed friction was independent of the velocity, but stick-slip motion gives a clear indication that this is not always the case. In fact, it can be shown that if we measure a steady friction, or velocity when pulling or pushing a macroscopic body, there will always on some smaller length scale be a stick-slip motion of atoms or groups of atoms [4]. Therefore, learning more about stick-slip friction might be fruitful in understanding more about the collective behavior of asperities in contact and the resulting macroscopic friction laws.

We have carried out stick-slip friction experiments where a sandpaper is being pulled over a carpet (described in chapter 3). The carpets that are used in the experiments are made up of small fiber loops where the sandpaper gets a good grip. By measuring the force required to pull, and recording the sound produced by the breaking carpet fibers, we have been studying the behavior

[1] Adhesion is often defined when two different materials are involved, while cohesion is used when similar materials are in contact.

of the interacting surfaces at very small velocities $\dot{x}(t)$. We believe the carpet-sandpaper system can be regarded as a way of looking at the microscopic details of stick-slip motion through a "macroscopic window". That is, all stick-slip events in our experiment are more easily observed, and visualized, than in a "normal" friction experiment, where the stick-slip events often only happen on the molecular scale.

When the sandpaper is pulled with an elastic string at a very slow rate ($10\mu m/s$), highly irregular stick-slip motion is observed. This suggests that very complex dynamics is governing the system. The experiments were analyzed by calculating the magnitudes of the slips events, and their distribution was found to obey the same functional form as that of the distribution of earthquakes: a power-law distribution. That is, the probability that a slip event or earthquake, X, is larger than some event magnitude x, can be written as $\sim x^{-b}$, where $b \sim 2/3$ both for earthquakes and our experiments. Many systems that are out of equilibrium and with a seemingly very complicated behavior, are found to give similar statistics. This class of systems all have in common that events happen at a much shorter time scale than the driving of the system, and where the probability of an event happening is described by a power-law distribution. The concept of self-organized criticality (SOC) was introduced in 1988 as way of describing this class of systems [5, 6]. In 1993 Feder and Feder [7] performed the original carpet experiment, and found that the distribution of slip event magnitudes followed a power law. They were the first to experimentally show the possibility of SOC in a stick-slip process. However, the authors did not explore the dependence of the result on system parameters such as load, elastic properties and different surface types. A cellular automaton model for the carpet sandpaper system was proposed, but the statistics of their simulations did not have the same properties as their experiments.

In addition to reproducing the experimental results in [7], we have, with the introduction of the temporal aspects of the slips, made a distinction between two different types of stick-slip motion depending on the type of surface: stick-creep motion (SCM) and stick-slip motion (SSM). In SSM, all the gripping carpet fibers will loose their grip during big slip events, and macroscopic motion of the slider is easily observed. In SCM, there will at all times be carpet fibers that are gripping to the sandpaper, even during the largest slip events that can last more than 100 seconds. Surfaces with a low density of carpet fibers yields SSM, whereas a high density will give SCM. Both SCM and SSM will produce a power law distribution of slip sizes, but with different exponents b. We have also, for SCM, found that the distribution of event duration times is distributed as a power law.

As an exploratory study, we have in chapter 3 explained novel methods of both visualizing the dissipation and geometry slips/creeps using as infrared camera, and obtaining details about individual breakings of fibers using a microphone and a sound card in a PC. In chapter 4 we describe how the statistics of the slips event magnitudes depend on experimental parameters such as sandpaper coarseness, normal force and elasticity in the pulling system. A model describing the triggering and propagation of creep events is proposed in chapter

5. This model predicts the same distribution of creeps as obtained from SCM experiments, that is, $b \sim 2/3$. In chapter 6 we present a model for the halting of slip events. That is, once a slip has been triggered (all hooked fibers let go) we describe a possible model for halting the slip event. A discussion and a summary of our findings are presented in chapter 7.

Chapter 2

Friction

When the word "friction" is mentioned, what first comes to mind is a picture of two surfaces rubbing against each other. This kind of friction is called contact or sliding friction, and is partly responsible for not letting everything drift apart, and for in general slowing things down. Another kind of friction is viscosity.

In general the macroscopic motion of bodies surrounded by an external medium will be accompanied by irreversible frictional processes. This results in converting the kinetic energy of the bodies into heat, and ultimately bringing the motion to a halt. We say that the energy is dissipated. Joule established through systematic studies that work could be converted to heat, while Carnot found that there is an upper limit to the efficiency of a heat engine. Thus the physics of friction is of fundamental interest both for engineering purposes and for a better understanding of the principles of physics. The rest of this thesis will focus on the first kind of friction, namely the friction between solid bodies in contact.

In this chapter we will present a short summary of the most important results that have lead us to the present knowledge about friction.

2.1 Common ideas about friction

It is known from experience that when two solid objects make contact they will resist relative motion along the plane of the contact area. From situations where friction is handled to our own benefit, like ice-skating, skiing, and driving a car, we have learnt some of the basic laws of friction :

- the magnitude of friction is dependent on what combination of materials we choose
- the visual topology or roughness of the surfaces affects the amount of friction
- the amount of friction is drastically reduced when one of the surfaces is lubricated (using an agent such as oil).

- as long as the relative velocity of the surfaces is not very small, the friction force is rather stable

- for small relative velocities, the friction can be very irregular, sometimes even bringing the bodies at rest

The behavior of the frictional forces is sometimes very much dependent on the actual speed at which the surfaces move over each other: squeaking doors do not squeak when you open them very fast, the tone from a violin is partly decided by how fast the player moves the bow over the strings, and to decelerate a car uniformly and stop it without a jerk, the driver must ease up on the brake in the final moments. Other, not so obvious factors that can decide the amount of friction are the actual area of contact between the surfaces, the magnitude of the normal force pressing the surfaces together, the humidity, the temperature and material properties to mention a few. These frictional factors are often encountered in our daily life and their effect is most often predictable and taken for granted.

The motivation for exploring the different aspects of friction must have had its origin in solving practical problems. An illustration from 2400 B.C (Figure 2.1) shows how lubricants are used when a big statue is being pulled to reach its destination. A nice summary of the historical development in understanding friction can be found in the thesis of Elise Bergli [8]. A more thorough analysis of the history of tribology[1]. I will here only restate the conclusions about friction reached by Leonardo da Vinci, Amontons and Coulomb. These conclusions now help to constitute the classic laws of friction:

- The force F required to move a load, is proportional to the load N: $F = \mu N$

- The friction is independent of the apparent area of contact A_a

- The coefficient of friction μ is independent of velocity and the apparent contact area

These classical friction laws have outlived a variety of attempts to explain them on a fundamental basis in terms of, for example, surface roughness or molecular adhesion. Friction is not well-understood in terms of physics.

Modern techniques, such as the atomic force microscopy (AFM) and the scanning tunneling microscope (STM) allow scientists to reveal details about friction on a the smallest length scales. Together with a wide accessibility of computational power and the development of computational physics this has triggered a widespread interest in friction. Therefore, a majority of the articles about friction treat the problem from a microscopic point of view. It is therefore natural to review some of the modern findings of the details about friction.

[1]See can be found in the book by Dowson [1]

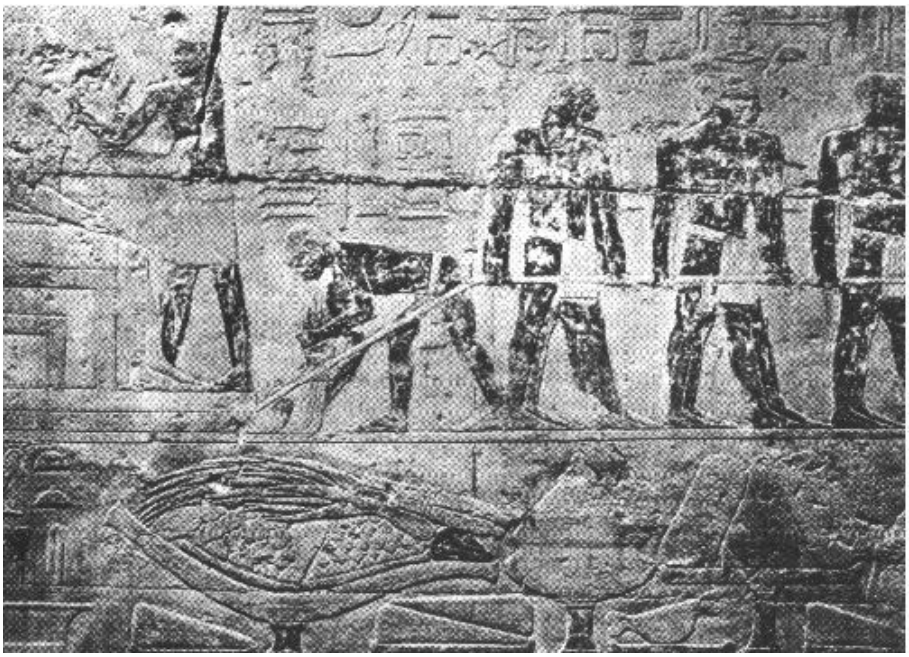

Figure 2.1: The picture shows the transporting of the statue of Ti (2400 B.C). The person who applies the lubricant (the tribologist) between the sledge and wooden planks is seen in front of the sledge. The lubricant consisted of water which has a great lubrication effect on wood. The picture is taken from [1].

2.2 Friction on the microscopic scale

The scientific interest in friction increased during the industrial revolution as the industry saw need for better and more reliable machinery. Much scientific work was put into experimental studies, specially on lubricants, but little pioneering theoretical work was produced. An exception is Hertz's theory for elastic contact in 1880 [9], but it took more than 70 years before his work was used in connection with dry friction.

From the 1940s, scientists have been lucky to enjoy, and to take advantage of a very rapid development of highly sophisticated measurement technology, such as the surface force apparatus and the atomic force microscope used to determine frictional mechanisms at the atomic scale. The influential work by Bowden and Tabor [3] (1950) were among the first to exploit this "new" technology in the field of tribology.[2] They were able to explain the fact that the friction is independent of the apparent area of contact, and pointed out that there was a crucial difference between the apparent area of contact, A_a, and

[2]The word "tribology", is often used about studies of friction and wear of materials.

the real area of contact, A_r. It was shown that A_r alone determined the magnitude of friction, and that A_r was proportional to the normal force. Thus, the mechanisms responsible for friction was found to take place at discrete contact points between the surfaces. We therefore, in the next section, review some of the recent findings in contact physics.

Surfaces in contact

All naturally occurring surfaces are rough, even though they may feel "smooth". The detail of the roughness may have different properties depending on what scale you look at it. Establishing a theory for surfaces in contact has proven to be a difficult task. A wide range of fields within physics have to be combined to understand all the underlying mechanisms at work when two surface are pressed together. Even though these fields are well known separately, they are still somewhat disjointed.

Consider two solid surfaces placed in contact, as in Figure 2.2. From the figure one can see that only a small fraction of the apparent contact area, A_a, is close enough for it to contribute any frictional force. It is possible to simplify

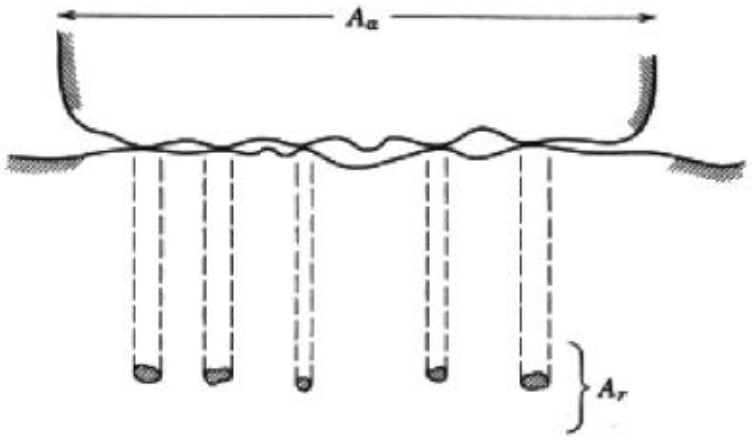

Figure 2.2: Schematic view of a contact interface, showing the apparent (A_a) and real (A_r) areas of contact. The picture was taken from [10].

the contact problem by saying that all interaction between the surfaces takes place where there is atom-to-atom contact. This is because the powerful atom-to-atom forces are effective only at very short range, that is, of the order of magnitude of a few Ångstrøm (10^{-10}m). These regions of contact will from now on be referred to as *junctions*. The sum of the junction areas make up the real area of contact, A_r. What we see is that the roughness of the surfaces determines the surface contact, as was also noted by Bowden in his memorable

words in a BBC broadcast from 1950 [3] : *Putting two solids together is rather like turning Switzerland upside down and standing it on Austria - the area of intimate contact will be small.*

Many workers have found a correlation between roughness parameters and friction, where in some cases the friction increases with the average roughness [11], which is the result we intuitively expect. Opposite effects have also been reported (see [12] and references therein).

Elastic contact

In order to get an idea about the physics at a junction, the situation can be simplified by modeling the two contacting asperities at the junction as two elastic spheres pressed together. Continuum models that predict the contact area for various geometries of the asperities were, as mentioned, developed by Hertz [9]. Imagining the junction as two spheres pressed together, Hertz found that, if the deformation is truly elastic, the area of contact, A_r, is related to the load N pressing the spheres together, as

$$A_r = KN^{\frac{2}{3}} \ , \tag{2.1}$$

where N is the normal load, and K is a constant depending upon the local radius of curvature and the elastic constants of the materials. The linear relationship between friction [3] and load seen in the classical friction laws, does not follow from equation (2.1) – new theories were needed.

In reference [13] a more realistic situation is considered, in which many small elastic junctions take part in A_r, it can be shown that equation (2.1) no longer holds and that the true area of contact can be written as :

$$A_r = K'N^n, \tag{2.2}$$

where both K' and n depend on the form and the properties of the surfaces, and n takes a value between 0.67 and ~ 1.0, depending on the size of the covering spheres.

Plastic contact

Indentation experiments suggest that plastic deformation of the asperities at the junction takes place even for a small normal force. When two surfaces are pressed together, the material at the junctions will start to deform, and as the local pressure becomes high enough, the material will start to deform plastically. New junctions will continue to appear and grow in size as the surfaces get closer, and this will go on until the contact pressure integrated over all the junctions (A_r) equals the force pressing the surfaces together (N). That is,

$$A_r p_m = N \ , \tag{2.3}$$

[3] According to the classical friction laws, the friction force is assumed to be proportional to A_r.

where p_m is the smallest yield pressure[4] of the two materials [3]. Note that p_m is not related to the elasticity of the material, but rather to the kind of process by which the deformation takes place. This is illustrated by comparing rubber and a metal: rubber is elastically "soft" and plastically hard, while it's the opposite way for most metals.

By considering all junctions to be in a state of incipient plastic flow [4], that is, $Mg = p_m A_r$, where M is the mass of the body on top and g is the gravitational constant, one can estimate A_r from experimentally obtained values of p_m. A steel cube with sides 10 cm, $Mg \sim 100N$ and $p_m \sim 10^9 N/m^2$ for steel, placed on a steel table will give a value of $A_r \sim 10^{-7} m^2 = 0.1 mm^2$. This is only a fraction, or 10^{-5} of the apparent area of the cube. Typical junction sizes obtained from experiments suggests an area of $\sim 10\mu m$ per junction. This gives a total of about 1000 junctions between a steel cube of 100cm^2 in contact area, and the steel table.

Forces acting between surfaces in contact: Adhesion theory

Attractive and repulsive forces between surfaces can be said to take place only between touching atoms, while atoms separated more than a few Å, play essentially no part in determining the interaction.[5] The interactions between the touching atoms might be of various electromagnetic origins such as dipole-, ionic-, dispersive- and inductive forces, but their total sum results in a stable equilibrium separation between the surfaces.

The work or force required to separate two surfaces in contact, a phenomenon known as adhesion, is indeed a big study on its own, and is today receiving great scientific attention. The master thesis of Elise Bergli [8], will serve as a splendid reference at this point. I will try to summarize, from her work, what has been done in this area of research.

The forces of adhesion

The strength of the interacting forces between materials in contact are often very small, but can be considerable for materials such as clean metals, chewing gum, and model clay. Two solid bodies situated adjacent to each other will adhere. Reasons for not observing adhesion can be explained by three phenomena: a small value for the real contact area, contamination of the surfaces, and residual elastic stresses which break up the adhesion joints (elastic springback).

The interaction at the junctions is usually modeled using the well-known two particle Lennard-Jones potential. With the concept of surface energy γ, the adhering force between spheres of radii R_1 and R_2 is found to be $2\pi R \Delta\gamma$. Here $\Delta\gamma$ is the work done to separate unit areas of media, and $R = \frac{R_1 R_2}{R_1 + R_2}$ [3].

Using Hertz's contact theory as a foundation, new theories where the material properties have been included, have been developed. When two bodies are

[4]The pressure before the material starts to deform plastically

[5]In particular the long range van der Waals interaction gives a negligible contribution to the attraction.

brought into contact the idea is that adhesion forces will flatten the surfaces somewhat, and this will lead to a finite contact area. The results indicate that the total energy in a junction contact, is a sum of the stored elastic energy, the mechanical energy in the applied load and the surface energy. The force required to separate the surfaces is given as

$$F = -\alpha\Delta\gamma\pi R\,, \tag{2.4}$$

where α is a constant dependent on the material properties.

Bowden and Tabor proposed that cold-welding would take place over the junctions, and that the friction force was equal to the force S required to shear these junctions. A plowing force in certain situations is also needed. The total friction force could therefore be related to the pressure yield strength, p_m, and the shear strength, p_s, of the junctions (from equation 2.2),

$$F = A_r * p_s = \frac{Np_s}{p_m}. \tag{2.5}$$

The coefficient of friction could then be given as $\mu = p_s/p_m$. What happens to the surface when a pull-off force is applied, is that some of the material will continue to be attached while the surfaces depart. This will create a "neck" of material before the surfaces suddenly let go [3]. This wear of material was presumed by Bowden and Tabor to be the main cause of friction. But later experiments have shown that substantial friction can exist even without wear [14].

For a theory of adhesion to be practically useful, possible plastic, as well as elastic deformation of the asperities must be considered.[6] That is, net energy dissipated to permanent deformation of the asperities is most likely to occur, to some degree, in most real situations. Strong correlations among many of the mechanical properties, like Young's modulus, elastic strain and hardness, makes the dynamics of adhesion a very complex system.

As we see, the dynamics behind friction is very complicated even before any lateral motion of the surfaces has been initiated. We will now see what happens when the contacting surfaces start to move in the plane of contact.

2.3 Sliding friction

As we have seen, classical and "well known" laws of friction, maintain that the friction coefficient is roughly independent of important variables such as contact area, normal force, and velocity. We have also seen that a microscopic picture of the physical processes, which are believed to give rise to friction, are quite complicated, and that these processes are not easily generalized.

So what does sliding friction depend on? Clearly, friction depends primarily on the nature of the sliding surfaces, and the lubricants and the contaminants at

[6] No mathematical theory of adhesion has yet been worked out, and this makes any calculation of adhering forces impossible

the interface. Discussions regarding lubricants and contaminants on the surfaces will not be treated further. The focus of this thesis will be directed toward understanding the connection between microscopic and macroscopic details of dry sliding friction.

Possible mechanisms of sliding friction

As we saw in the last section, Bowden and Tabor believed the main cause of friction came from the force required shear cold-welded junctions (equation (2.2)). This might be a reasonable explanation for friction between materials like clean metals, but there are materials where adhesion is a very small component of the total friction force and the classical friction laws still hold. We will briefly discuss some of the possible mechanisms at play in contact friction.

Adhesion

We have all experienced that friction between clean metals results in wear of the surfaces. The wear of a non-lubricated bicycle chain is a good example. In Figure 2.3 the effects of friction wear between metals is illustrated: wear debris has been traced using a radioactive metal.

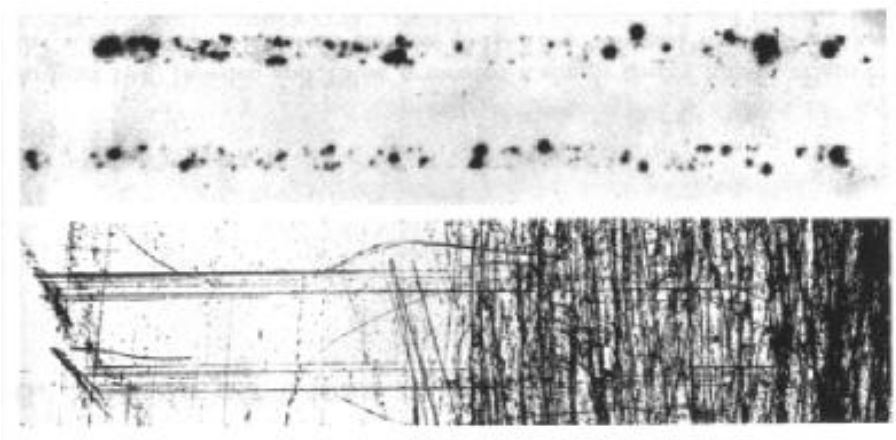

Figure 2.3: Micrograph (bottom) and autoradiograph (top) showing a copper surface with roughness 250Å(unscratched) and 5000Å(scratched part) after a radioactive copper block has been slid over it. The load is 4kg and speed 0.1 cm/s). Debris has been left behind as black dots in the picture. Note how little dependence the roughness has on the wear of the block. The figure is taken from [4].

The adhesion theory neatly explains many of the experimentally observed effects of friction, such as the existence of a static frictional strength, the proportionality of friction force and the normal force, and the weak dependence

of friction on the surface roughness [10].[7] There are, however, some problems with this approach. From equation (2.2), $\mu = p_s/p_m$, which gives $\mu = 1/5$ for an ideal plastic material. Most metals have a $\mu > 0.5$. This calls for additional mechanisms of friction.

Plowing – elastic solids

In addition to adhesion as a mechanism of friction, there is always a plowing or grooving frictional term. If one hard surface is slid over a soft surface, the hard surface will tend to dig into to the softer and produce a groove. The energy required to produce the groove must be supplied by the friction force. Similarly, sharp asperities slid over a soft surface produce scratches, which will cause a friction force. This grooving is not necessarily permanent, but there is always energy dissipated because all surfaces deform imperfectly. This is related to the internal friction and hysteresis of solids.

Experiments with rubber and wood show, as with metals, that the mechanisms of friction is a combination of adhesion and plowing. The difference is that in metals the plowing is often plastic, while it is more elastic for materials like wood and rubber. The hysteresis losses in elastic materials are often so high that it becomes very important in the total amount of friction.

Geometric friction

If someone, without any prior knowledge about friction, is asked what he or she believes is the main mechanism for sliding friction, the person will most probably ascribe the friction effect to the roughness of the surfaces. They picture the asperities in the materials to bump into each other, or being lifted over one another, with the result of heat production (which we often feel is the net effect of friction).

Rabinowicz [10] comments in a section entitled **Other contributions to the friction force** (apart from adhesion) that the effect of geometric friction – or *"the roughness component of friction .."* as he likes to call it: *"..arises from the need to lift one surface over the roughness of the other .. there might be a negative roughness component of friction, since θ (the asperity inclination θ contributes with $tan(\theta)$ to μ) will take on negative as well as positive values. Summing up for all the contacts, we note that regions of positive θ and negative θ coexist, so to some extent the roughness friction terms tend to cancel out. What remains is usually a contribution of about 0.05 to the overall friction coefficient, representing a fluctuating force superposed on the main adhesive component of the friction force."*

A new crack at friction

No one has yet been able to confirm and predict the results of friction through calculations using first principles. The goal is to construct the friction force

[7] Most of the work is being done in inducing shear displacement of the junction interface.

either analytically or through computer simulations using molecular dynamics or methods of finite elements. Attempts at this have failed because of the mismatch between asperities on the surfaces, resulting in no friction at all.

Two alternative solutions to the problem have recently been proposed. In a paper in Nature (2001) [15] Mardar and Gerde propose a dynamical description of friction through the evolving of self-healing cracks. The idea can be visualized and simplified by regarding the surfaces as a carpet lying on the floor. If you want to move the carpet, without lifting it off the floor or rolling it together, you can do two things: the carpet can be slid over the floor, or you can form a ridge in one end by pushing it toward the center and then move the ridge across the carpet until it reaches the other end. A net movement of the rug is the result. This traveling ridge is in Mardar's theory supposed to represent a crack (a re-healing crack) traveling through one of the surfaces. The two surfaces at the ridge are no longer in contact, just as the two halves of a material break contact and come apart on a crack. An illustration of the idea is pictured in Figure 2.4. In a mathematical treatment of the problem, using techniques from continuum

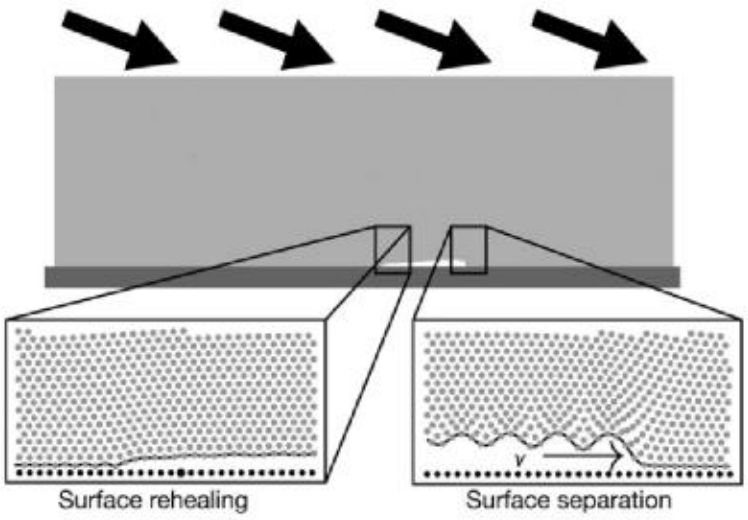

Figure 2.4: A self healing crack traveling through a compressed strip. The figure is taken from [15].

mechanics, they have succeeded in predicting a minimum shear force required to initiate a propagating crack. This force is also found to be proportional to the compressive force, as in Amontons-Coulomb's law. The idea is that once this minimum force is applied, self-healing cracks are formed, causing the surfaces to slide over one another.

It is still not clear whether this a possible and a true description of frictional processes. Only experiments can find out.

Quantitative laws of sliding friction

A way to roughly characterize the variations in the friction coefficient is by a "factor of 10" rule [10]: if you change a parameter like load, sliding speed or roughness by a factor of 10, the friction coefficient will change up or down by 10% or less. However, this is not a great variation and is generally not of any particular importance. One exception to this is the low-magnitude region of the sliding speed parameter. Sliding two surfaces over each other with decreasing speed, one suddenly reaches a velocity where the surfaces get "stuck" and the friction rises abruptly.

Apparently there are two friction coefficients for a given pair of surfaces: one coefficient before there is any motion, μ_s, and one after motion starts, μ_k. These are often referred to as the static and the kinetic (or dynamic) coefficient of friction. In Figure 2.5, μ_k and μ_s are illustrated from a typical friction experiment. It is always assumed that $\mu_s > \mu_k$.

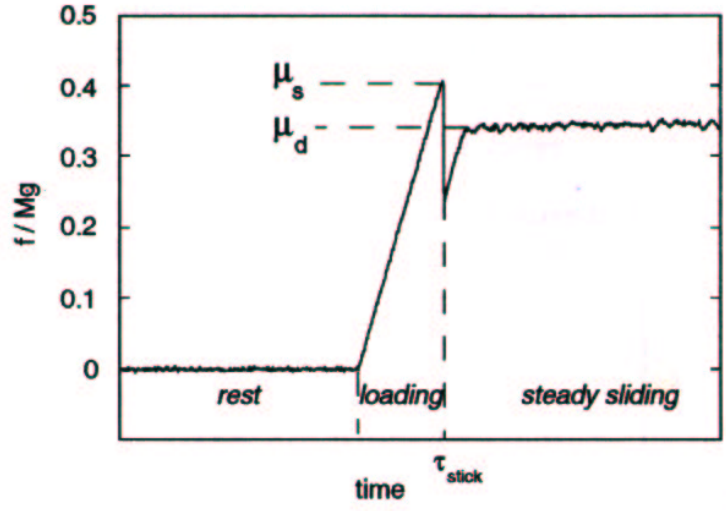

Figure 2.5: The force required to pull paper on paper is recorded. The pulling starts after a time at rest, and then the static μ_s and dynamic μ_k (labeled μ_d in the figure) friction coefficients are found. The picture is taken from [14].

It is common to show static and dynamic friction separately in tables of friction coefficients. Experiments have shown that this is a gross oversimplification and that this kind of "phase transition" from static to kinetic friction is hard to justify both from theory and from experiments. For many engineering purposes tables for μ_s and μ_k are useful, but their real/exact value (see for example [10] page 117-118) must be regarded with great skepticism. A plot of the distribution of 110 measured values for μ_s for steel on steel plotted in Figure 2.6, gives an

impression of the fluctuation present at low sliding velocities v. Strong fluctua-

Figure 2.6: A histogram showing the distribution of static friction coefficients for steel on steel surfaces. The time of contact is held constant in these experiment. The standard deviation is about 20% of the mean value. Tabled values for steel-on-steel μ_ss show a value of 0.58 (taken from [16]).

tions in μ_s are not unexpected, since that $A_r/A_a \sim 10^{-6}$ for a 1cm high block of metal (see page 10). Thus macroscopic randomness may not simply average out, and the classical friction laws may only exist in an average sense [17].

Aside from large fluctuations in the measured value of μ_s, it is widely known that μ_s is also a function of the time of contact. An example of this effect is shown in figure 2.7 (a), where μ_s varies most markedly at short times of static contact ($\sim$ 0.1 second). For longer times of sticking, mu_s increases only by a few percent for every tenfold increase in time [10].

The value of μ_k is in most cases slightly influenced by the relative velocity, v, of the surfaces, as is illustrated in Figure 2.7 (b). The scale of the time axis is in this case dependent on both the experimental setup and the materials in contact.

It is clear from Figure 2.7 b) that the friction as a function of v does not vary much when we stick to the parameter space for which the sliding speed is relatively high. That is, the "factor of 10" rule is roughly valid in this regime. However, if we let v go to zero, we will see that deviations from the classical friction laws will produce critical effects such as periodic or irregular stick-slip motion.

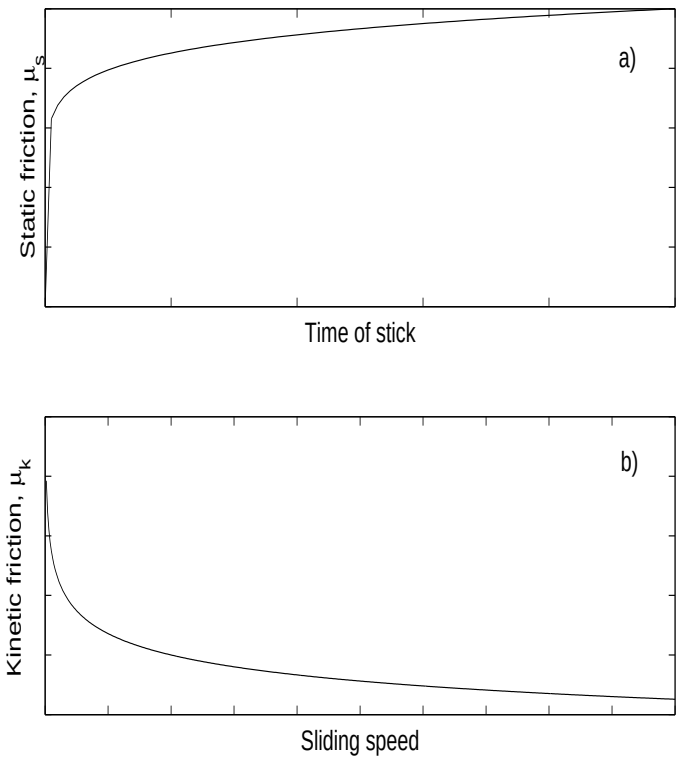

Figure 2.7: Figure (a) shows a typical plot of μ_s as a function of time: $\mu_s \sim$ constant + $t^{1/10}$. The largest change in μ_s is for small t. Figure (b) shows the velocity dependence of μ_k : $\mu_k \sim v^{-1/10}$. Also, the change in μ_k is greater for small values of v. The figures are reproduced from [10] (compare with Figure 2.8 where a velocity strenghtening effect also is present).

2.4 Friction at low sliding velocities

Friction at low sliding velocity often leads to a non-steady motion. That is, below a certain sliding velocity and given that the pulling spring is soft enough, it is often possible to see that the motion is made up of periods where the bodies hardly move, and periods where there are sudden motions.[8] This is called stick-slip motion (SSM) and is caused by the fact that the friction force does not remain constant as a function of distance, time or sliding velocity. Reasons for SSM can be found by inspecting Figure 2.8, which shows how the friction force varies for steady sliding at low velocities.[9] The observed "velocity weakening"

[8] At the microscopic scale there is no state where the bodies have no relative motion under a shear stress. There will always thermally activated creep [10].

[9] Steady sliding can always be obtained by using a stiffer loading machine or smaller mass.

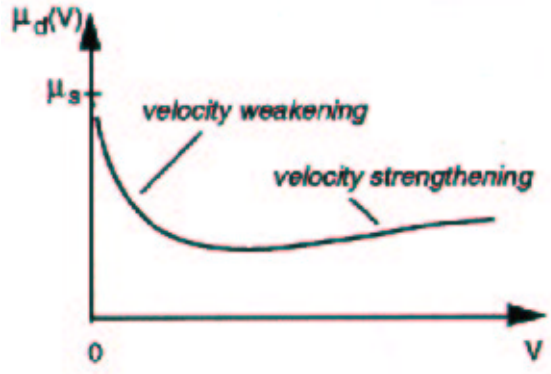

Figure 2.8: A typical plot of the friction force as a function of velocity V for steady-sliding speeds typically in the range 0.1 – 100 $\mu m/s$. For V = 0 the $\mu_k = \mu_s$ (μ_k is labeled μ_d in the figure). The figure is taken from [14].

effect in Figure 2.8, should be expected for the sake of continuity of μ at low velocities. When the sliding velocity is in the "velocity weakening" regime, a slight change in velocity (acceleration)[10] will be amplified because of the rather strong dependence between friction and velocity. A stick-slip cycle is initiated with a deceleration: it will consist of an elastic loading, or stick, while μ_k increases, followed by a stress relaxation, or slip, when the external forces have exceeded $M\mu_s$. Here, M, is the mass of the sliding body.

Emerging aspects of friction

From slowly driven friction experiments on different materials such as rocks [18], metals [19] and on paper [20], one interesting aspect of dry friction emerges: the characteristics of dry slow sliding friction, as shown in Figure 2.8, are essentially material independent.[11] Moreover, the statements of the classical friction laws have to be revised or refined as suggested by Rabinowicz [14, 10]:

- μ_s depends on the history of the sliding surface, and it increases slowly with the duration time after the sliding has stopped, or the slider has been put in contact with the surface (see Figure 2.7 (a)). From experimental observations on rock [18] and metals [10], this effect is likely to be related to a slow plastic relaxation of the junctions, leading to an increased real area of contact, A_r, and thereby a higher μ_s. A fit to experimental data

[10] For example caused by homogeneities, or hysteresis in the surfaces.

[11] However, the characteristics of the classical friction laws can roughly be said to be material dependent, ranging from friction mainly caused by adhesion in metals and diamond, to friction dominated by plowing in elastic solids [3].

[18] suggests a functional form of the static coefficient of friction:

$$\mu_s(t) \sim a + b\, ln(t)\ , \tag{2.6}$$

where a and b are material dependent parameters, and t is the time after the sliding has stopped.

- μ_k will, when measured in the steady sliding regime, decrease at the lowest velocities as illustrated in Figure 2.7(b) and 2.8. One can in this velocity range define a characteristic length $D_0 \sim 1\mu m$, such that, if subjected to a sudden change in sliding velocity, friction is found to evolve to its new steady-state value over the slip-distance D_0 [18]. This velocity weakening effect of the coefficient of friction is thus described by the length, D_0, which can be seen as the average sliding distance after which a given set of contacts has been destroyed and replaced by a fresh one [21].

- The aging of μ_s and the velocity dependence of μ_k are related behavior which result from creep of the surface contact and a consequent increase real contact area with the time of contact.

- One can also talk about a velocity threshold where $v > v^*$, above which μ_k starts to increase again. This is called velocity-strengthening, and is also illustrated in Figure 2.8. So when the pulling velocity is increased, the motion crosses-over from a creep dominated regime when $v < v^*$, to a regime dominated by a global inertia (steady-state) for $v > v^*$ [14]. In friction experiments with rocks, the slope of the velocity strengthening region is known to be both negative and positive, depending on the rock type and parameters such as the temperature.

These general laws of low-velocity friction dynamics are well explained by an heuristic model [20]. In this model the sliding dynamics consist of a single degree of freedom, namely the translation of the center of mass of the slider, which undergoes a noise-activated motion in a periodic pinning potential and where the "strength" of the pinning potentials are assumed to increase with their age. Such a phenomenological approach is useful for analyzing experimental data and suggesting the underlying mechanisms, but a number of questions remain unanswered :

- At the scale of the contacting asperities, what is the basic mechanism for the pinning force at the junctions ?

- Does the macroscopic motion depend on the pinning of only one junction, or are the junctions and the asperities involved in a collective affair resulting in a macroscopic pinning or motion ?

- Can macroscopic friction be described or modeled without knowing all the details at the smallest scales ?

The last two questions touch at the heart of this thesis, namely the problem surrounding the collective behavior of asperities and whether interactions among them plays a crucial role in determining the dynamics of macroscopic friction. We will see that in the very slow sliding regime and for certain surface parameters, stick-slip motion can be characterized by inspecting the distribution of the slip event magnitudes.

Irregular stick-slip motion

It is well known that stick-slip motion (SSM) can be very irregular [3, 20]. As mentioned earlier, strong fluctuations in μ_s will be present when the ratio A_r/A_a is small, and the deterministic nature of SSM will depend on this fact. That is, if the surface properties on the scale of the asperities making up the junctions lead to a highly fluctuating real area of contact, A_r, or if the material is not homogeneous, then non-deterministic SSM is expected. Otherwise, when the ratio A_r/A_a is bigger, the microscopic fluctuations in μ_s will lead to a more periodic and possibly deterministic SSM [14]. A large normal load therefore seems to have a regulating effect on SSM, such as reported for rock experiments where the nominal pressure is of order $1 - 10$ MPa and the SSM regularity is good [18]. Releasing the pressure will lead to more irregular SSM.

Irregular SSM can be analyzed by calculating the individual slip magnitudes (defined later) from force measurement required to pull or positioning systems, and by "listening" to the energy dissipated by the slip event (seismology). Statistics of the slips events, both in the temporal and spatial domain, may give information about the underlying dynamics. For some sliding parameters the distribution of slip magnitudes will be exponential with a characteristic scale [17]. While for other sliding surfaces, often for very slow sliding velocities ($10\ \mu m/\mathrm{s}$), the distribution of slips will follow a power law. That is, the probability $p(x)$ for the slider to slip for example a distance $X \in [x, x + \Delta x]$ is given as:

$$p(x)\Delta x \sim x^{-\beta}\Delta x \ , \tag{2.7}$$

where β has a non-trivial value (< 2). Equation (2.7) states that there is no characteristic length scale in the system besides possible finite size effects [22]. The crossover from an exponential to a power law distribution of slip magnitudes is often obtained by decreasing the velocity even further. As an analogy to critical systems this crossover to a scale invariant distribution of event sizes might be related to an increased correlation length in the system [6].

Stick-slip experiments that find a power law distribution of slip sizes are not numerous [17, 7, 23, 24], and questions have been asked whether a power law distribution of slips is interesting at all (see page 433 in [14]).

These special distribution of slip events (power laws) have tempted people to ask whether the often very irregular observed behavior of SSM is possible to understand without going into the details of the complex interaction between the two sliding surfaces. In the search for an answer to this challenging question, a great number of articles, from both in the physics and geology/geophysics

community, have tried to explain these results. Most of these articles are based on simulations or theoretical derivations, and most of them lack confirmations through experiments.

Very simple spring-block models and cellular automaton type models have been found to produce power law distributions of slip magnitudes [7, 6, 25]. Spring block models are not well suited for a description of the physics in our experiments. We believe the reasons for this lies in the negligible elastic interaction among the contacting asperities. Instead we have proposed an alternative type of model which we have found to reproduce the experimental results. This model will be presented in chapter 5.

Analogies between stick-slip motion and other systems such as vortex pinning in super conductors, charge density waves, and avalanches in rice piles [6, 4] have raised question whether there exists a universality in these type of systems. A new field of interest in the physics community, called self-organized criticality (SOC), has emerged and aims at explaining the mechanisms in these systems. We will now briefly review SOC and see how it differs from other non-equilibrium systems.

2.5 Generic Scale Invariance: a property non-equilibrium systems?

In equilibrium systems with generic parameter values, correlations fall off rapidly – most often exponentially as $e^{-r/\xi}$ – in space, being set by the correlation length ξ. Only by carefully adjusting the system parameters to a critical point, or by considering a system with certain symmetries, can we make ξ diverge and cause algebraically decaying correlations described by a power law. [12] Systems behaving in this way are often referred to as being "self-similar" or "scale invariant", reflecting the way that power laws, unlike exponentials, lack a characteristic time or length that decides the scale for the decay. In other words the system repeatedly moves into a state where things are finely balanced and a small disturbance in one part of the system can trigger massive changes across its entirely.

In equilibrium systems, this behavior is rather the exception than the rule. The classical example of this behavior can be seen when a ferroelectric magnet is heated. Above a certain temperature, T_C, the spontaneous magnetization vanishes. [13]

In non-equilibrium systems - those driven externally in some fashion and so prevented from reaching thermodynamic equilibrium – the situation is quite different. Here, scale-invariance is now recognized to occur abundantly, and its

[12] An algebraically decaying function, or a power law is on the form $f(\psi) \sim \psi^{-a}$. The function f might for example be a correlation function and ψ the length or time (often the order parameter of the system).

[13] The magnetization, M, actually goes as $(T_C - T)^{\beta}$ (a power law) when $T \to T_C$ (from below), and where β is a universal scaling exponent (with a value between 0.3 and 0.4) roughly identical for large groups of apparently diverse physical systems.

most famous manifestations are in power law distributions of both (arbitrary) spatial and temporal parameters [26]. A well known example of this kind of system, and of great relevance to this thesis, is the Gutenberg-Richter law [23] of earthquakes.

Two classes of Generic Scale Invariance

In the search for the origin of the scale invariance in nature, two main classes of systems are considered:

- "Ordinary" non-equilibrium systems are known to resemble equilibrium ones in that they need parameter tuning or special symmetries to produce scale invariant behavior. The removal of the detailed balance constraint is an important factor to achieve this.[14] The scale invariance observed in experiments can often be predicted from an appropriate Langevin equation, or equations containing local conservation laws or certain symmetries [22]. The timescale at which the relaxation of the dynamics takes place is comparable to the timescale on which the system is driven with.

- Self-organized criticality (SOC) is a different class of systems that exhibit scale-invariant behavior, and differ mainly from the "ordinary" systems in that the system is driven slowly away from the ground state. However, the timescale of the driving is very large compared with the relaxation of the system. SOC systems relax on a much shorter timescale than they are perturbed.

Of the two classes, the SOC-class is of greatest relevance to the carpet experiment, and a more detailed description of SOC will follow. A good description of the "ordinary" class of systems can be found in [22] and references therein.

Self Organized Criticality

In 1987 Bak, Tang, and Wiesenfeld introduced the idea of self-organized criticality (SOC) [27] which was aimed at categorizing or explaining systems with a seemingly irregular behavior, but that for some reason gives rise to a frequency spectrum $P(f)$ that decays as $1/f$ over several decades of frequencies [27, 28].[15] Solar activity, the resistance in conductors, the flow of big rivers and an hourglass [6, 29] are examples of such systems, where the $1/f$ frequency spectrum indicates that there exist temporal correlations over a wide range of timescales. This is a clear indication of some sort of cooperative effect in the system. Despite the ubiquity of such signals in nature, no underlying mechanism was proposed until the arrival of the concept of SOC, and the $1/f$ spectrum was believed to reflect the intrinsic dynamics of a self-organized critical system. The power spectrum from our experiments is found to be described by a power law with

[14] Detailed balance: in thermal equilibrium the rate of any process that leads to a given state must equal the rate of the inverse process that leads from the state.

[15] The power spectrum often goes as $1/f^{\varphi}$ where $\varphi \sim 1$.

Another puzzle which was targeted by the SOC-hypothesis, was the empirical observation that very many spatially extended objects, such as the shapes of coastlines, mountain landscapes and fracture surfaces appeared to be self-similar "fractal" structures [26].[16] This "fractal" shape of objects formed under conditions where $1/f$ frequency spectrum is observed in the time series, was believed to be the fingerprint of a SOC-system.

Sandpiles and earthquakes

Bak et al. suggested a "simple" dynamical system with extended spatial degrees of freedom that naturally evolves into self-organized critical structures of states which are barely stable [27]. Their proposed model has later come to be known as the "sandpile model". The model can be visualized as a pile of sand where one grain of sand is dropped at the time, and where the dynamics is expressed through avalanches of sand taking place when the slope of the pile gets steep enough. That is, as sand is added at the top of the pile, the slope of the pile builds up to a "critical" state where it fluctuates around an angle of repose. Adding more grains of sand when the pile is in this "self-organized critical" state, will trigger sand-avalanches of all sizes. This "critical" angle of the slope can be said to be the "attractor" of the pile-dynamics. The authors [28] then state that "Once the critical point is reached, the system stays there". The behavior of systems at the self-organized critical point is characterized by scaling relations (relations between power law exponents) – and the systems obey "finite-size scaling" just as equilibrium statistical systems at the critical point [31]. When the pile is at this critical state, the introduction of a new grain of sand may have a wide range of results: from just the displacement of a few grains, to an avalanche causing sand to be transported off the pile. Both the size and lifetime of these events span a wide range of magnitudes, reflecting the lack of both a timescale and a length scale for the system. The distribution of avalanche sizes and lifetimes, that is, the probability of having an avalanche lasting a certain time or having a certain magnitude, was found to yield a power law distribution of avalanches. In a numerical study of a "lattice sandpile" [27] it was found that the size-distribution $P(s)$ of avalanches with energy s could be described in a simple way, using a power law, reflecting the self-similarity of the system. That is, $P(s) \sim s^{-\beta}$, where β normally lies between 1 and 2 depending on various parameters of the studied system. Also the distribution of lifetimes of the avalanches could be described as a power law. Later, experiments, performed here at University of Oslo, using rice instead of sand [32], gave the experimental evidence for power laws in granular media.

Other systems where the dynamics is dominated by a wide range of events, or avalanches, and where the driving rate is much longer than the relaxation time are also found to be well suited to be described as SOC-systems. The number of articles published on experimental SOC systems are great and they cover fields

[16] Fractals are mathematical constructs characterized by a never-ending cascade of similar structural details that are revealed upon magnification on all scales. See [30] for a description of fractals.

such as, avalanches of granular media [32], earthquake dynamics [33, 28], noise in ferromagnets (Barkhausen noise)[34], flux lines in high-T_c superconductors [35], microfracturing [36], lung inflation [37], and friction [7, 24].

The scientific interest in SOC-models [5, 7, 22, 28, 25], and the following interpretations and "philosophy" around SOC [38, 5, 39, 22, 40, 6] is even greater, and the precise significance of SOC is still controversial. It is therefore an ambitious task to try to summarize the essential properties of a SOC system. The key features of SOC are:

- There is a large number of meta-stable states, that is, their number should increase with the number of sub-systems (e.g asperities, grains of sand).
- The dynamics is driven very slowly away from the ground state.
- The system, after a possible initial transient, should be stationary in the asymptotic time limit.
- There are recognizable relaxation events (e.g avalanches) where the input energy (driving force) is expelled from the system.
- The distribution of these event-magnitudes is a power law except for those events that feel the size of the system (finite-size effects).
- The power spectrum should be of the form $1/f^{\varphi}$ where φ has a value ≥ 1.
- The initial conditions should have no impact on the stationary state.
- The power law for event magnitudes should be obtained without fine tuning of the parameters of the system. The fine tuning can only be achieved by a limit procedure [38]. SOC systems is in this sense not sensitive to fine tuning.

The main purpose of the carpet experiment (in [7]) was to show that stick-slip friction can, in special situations, be regarded as a self-organized critical process. In this thesis, we have not focused on questions about whether this is true or not, but one can loosely say that our experimental results show that the carpet-sandpaper system exhibits most of the key features (listed above) of a SOC-system.

Chapter 3

The experiments

In this chapter we will discuss the stick-slip experiments (section 3.1) and the methods used to obtain the data in section 3.2. We will in section 3.2 also discuss the amount of noise present in the collected data, and by what means this can be reduced. Novel methods of obtaining information about the slip events will be discussed in section 3.3.

3.1 The Feder-Feder experiment

The apparatus is essentially the same as that used by Feder and Feder to obtain a power law distribution of slip event magnitudes in slowly-driven stick-slip motion [7]. A picture of the experimental setup is shown in Figure 3.1. In this experiment a rigid circular slider with small, rigid asperities (sandpaper mounted on a hard plastic disk) is loaded and dragged across a plane of elastic looped fibers that are sometimes bundled (a carpet). The force needed to drag the slider is measured using a strain gauge. The mounting of the strain gauge is pictured in Figure 3.2.[1] That is, the measured strain gauge deflection is proportional to the force that is applied. The deflection is proportional to the output voltage of the gauge and is measured by a multimeter.

[1] The workings of a strain gauge is explained in section 3.2.

Figure 3.1: A photography of the experimental setup is shown. The pulling direction is towards the bottom of the picture.

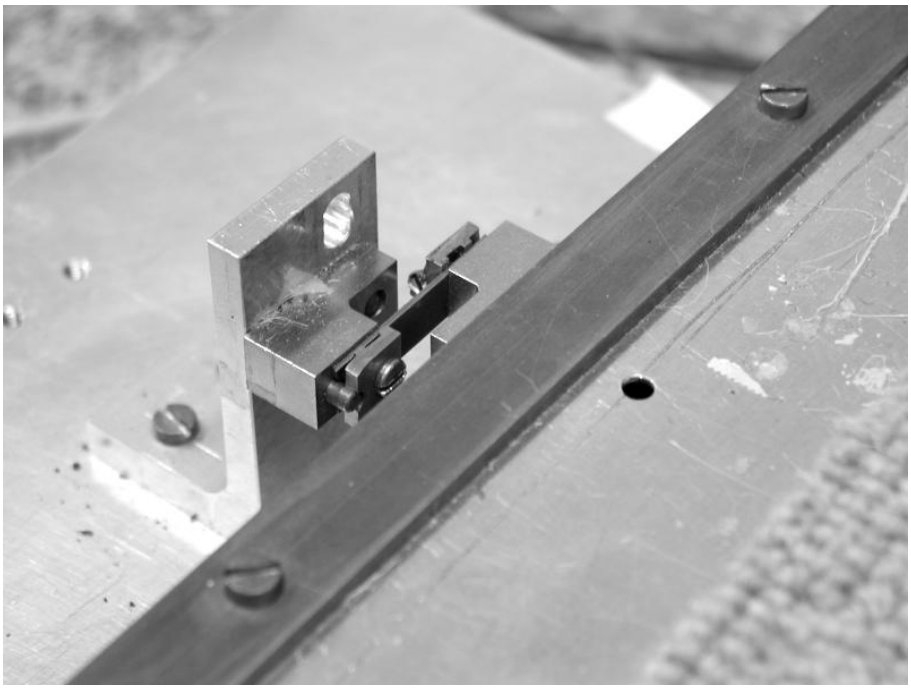

Figure 3.2: A top view picture of the strain gauge mounted to the apparatus is shown. The pulling direction is to the left in this picture.

In Figure 3.3 the force required to pull the slider across a carpet is shown for a typical experiment. Note that the force builds at the beginning, and drops suddenly at about 0.5×10^4 seconds. This dramatic rise and drop in force at the beginning of the experiment is characteristic of the interval in which the system "forgets" its initial state. After this drop in force, the measurements fluctuate around a mean pulling force value (in Figure 3.3 this corresponds to about 19V).

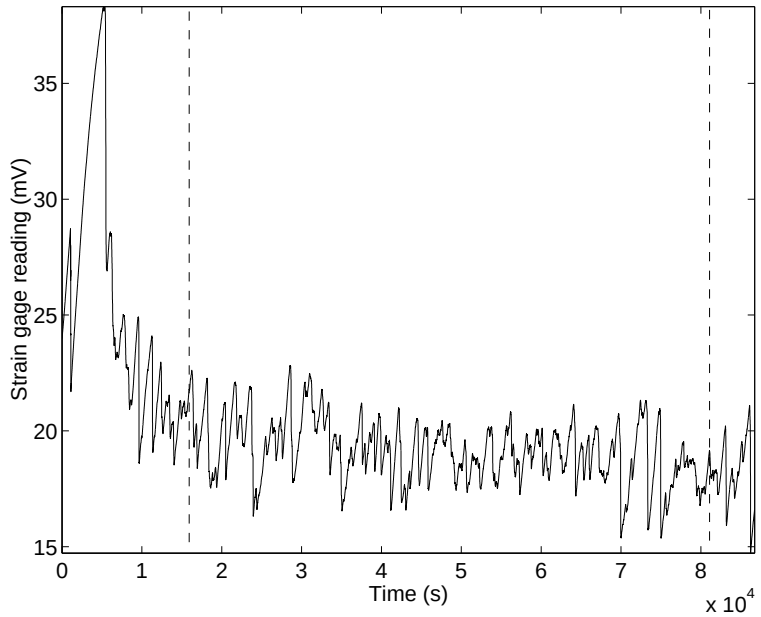

Figure 3.3: Raw data from experiment A. The region for which we have selected to measure event magnitudes is marked with vertical dashed lines. Note that the force builds at the beginning of the experiment, and drops suddenly at about 1.7×10^7 seconds. This dramatic rise and drop in force (strain gauge deflection) at the beginning of the experiment is characteristic of the interval in which the system "forgets" its initial state. This behavior is observed in all experiments.

These measurements of the force in time $F(t)$ are used to calculate the magnitudes, x, of slip events. All slip events will be referred to as just "events". An event magnitude here is defined in the following way, and is illustrated in Figure 3.4:

- **The change in force from any time t_1 when the time derivative of the force becomes negative ($F'(t_1) < 0$) until some later time t_2 when this derivative becomes positive again ($F'(t_2) > 0$). That is, the magnitude m is given by $F(t_2) - F(t_1)$.**

When the slider is driven slowly enough, about 10 μm/sec, the distribution in magnitudes of values for ΔF follows a power law distribution as shown in Figure

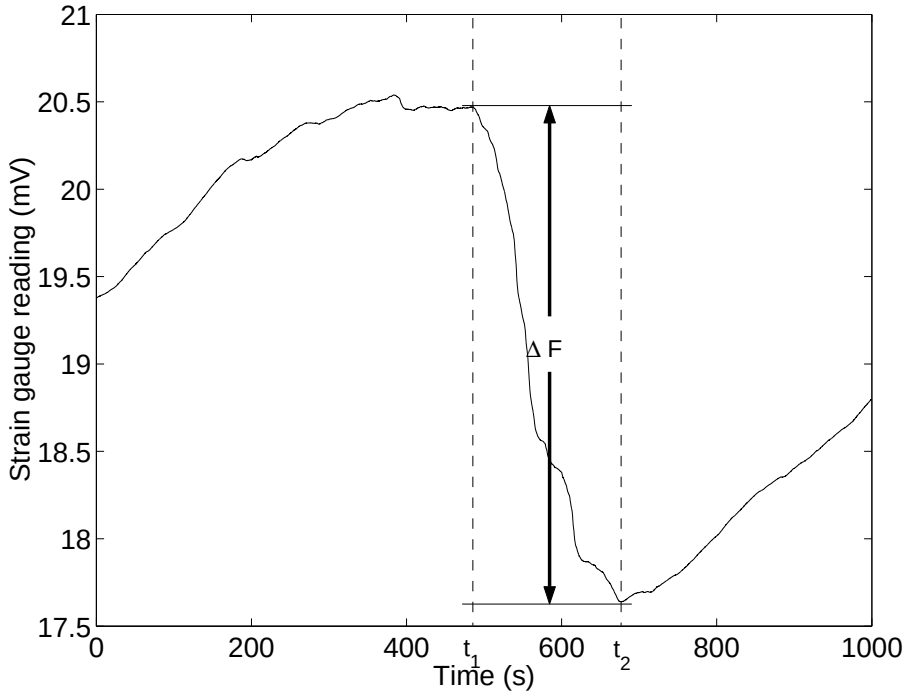

Figure 3.4: Raw data from experiment A (Figure 3.3) is magnified, and our method of calculating an event magnitude is illustrated. The event magnitude is given as $\Delta F = F(t_1) - F(t_2)$ ($\Delta F \sim 3$mV in this case). The duration time of an event is given as $t_2 - t_1$ (duration time is about 200 seconds for the shown event).

3.5. A similar power law was obtained by Feder and Feder in their original study (1991) and for this reason they suggested that stick-slip motion in the carpet-sandpaper system might become self-organized critical (SOC) [7]. The concept of SOC was discussed in section 2.5.

The number N of earthquakes recorded per year, of magnitude[2] greater than m, is given as

$$N(m) \sim m^{-b} \,, \tag{3.1}$$

where b takes a value between 0.8 and 1.2, depending on the size of the earthquake and its geographical location [23, 18]. This is often referred to as Gutenberg-Richter's law of earthquakes. Earthquakes occur by slippage along a pre-existing fault, and are therefore a frictional phenomenon. In [7] it is claimed that the magnitude of an event calculated from the carpet experiment is proportional to a quantity termed the *seismic moment* in the discussion of earthquakes (see

[2]See appendix E for explanation about the earthquake magnitude.

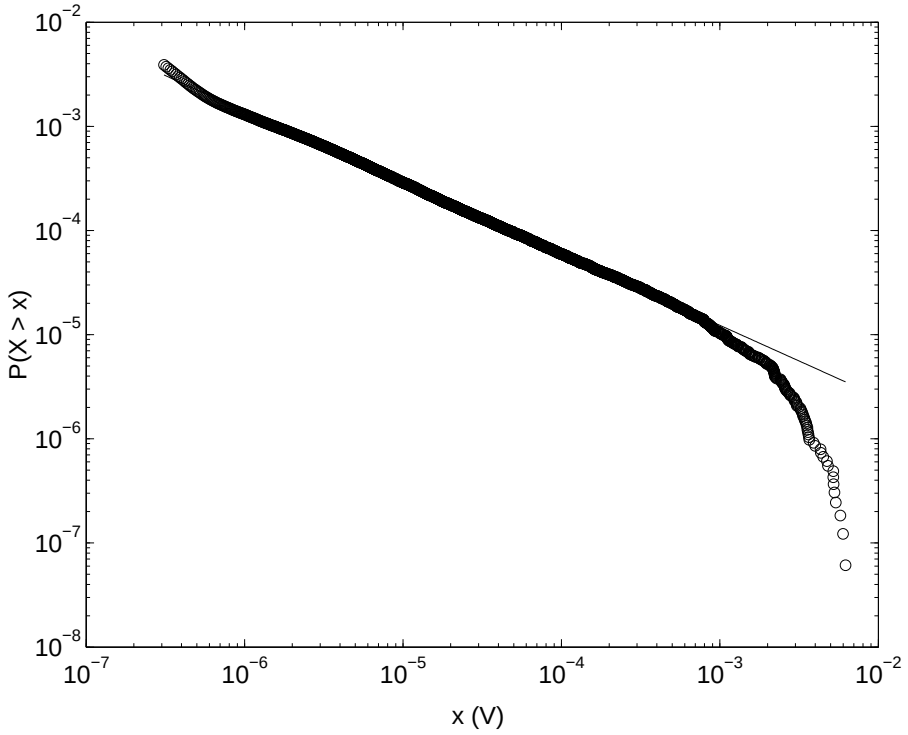

Figure 3.5: The cumulative distribution $P(X > x)$ of event magnitudes x. The slope of the log-log plot has a value of about -0.66±0.05 spanning about 3 orders of magnitude in the x-direction.

appendix E for details about the seismic moment). This analogy to the seismic moment allows us to both study earthquakes related processes at a more "near-field" approach, and from the field of earthquake dynamic learn more about fundamental frictional processes.

The apparatus

A schematic of the apparatus, and a blowup of the slider is shown in Figure 3.6. The carpet is taped onto an aluminum plate, which rests on a row of glass cylinders (pipettes 5 mm in diameter and 20 cm in length). The pipettes will help keep the plate from bulging while the slider moves over it. We will disregard the motion and friction induced in the pipettes since the the maximum deflection of the strain gauge is only about 1.5 mm.

The rectangular board which the pipettes rest on, is again fastened to a bigger rectangular aluminum board (fixed support), which is clamped to the same table as the motor. A strain gauge, which measures the amount of force

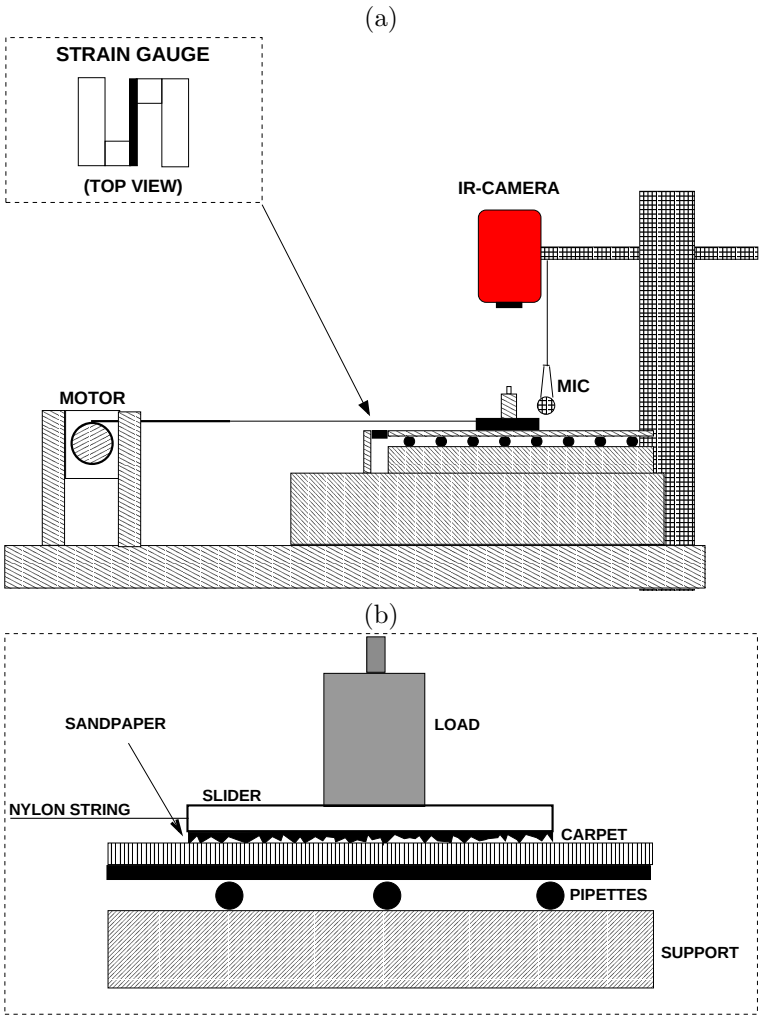

Figure 3.6: The experimental setup is shown in (a). The aluminum board that supports the slider is 900mm long and 250mm wide. The distance between the motor and the board is about 1200mm. The elastic string is 1100mm long, and has a thickness (varying with experiment) between 0.45 and 0.70 mm. The inelastic part of the string is long enough for the elastic part to have a constant length throughout the experiment. A close-up drawing of the slider with mass is shown in (b). The varying normal force is fastened to the slider using clay. The string is fastened to the plastic slider, as close as possible to the carpet without touching, using a knot. The slider is about The microphone (for sound recording) is mounted inside the slider as shown in Figure 3.19 (not as shown in the schematic drawing)

that is exerted on the slider, is mounted between the aluminum plate and the fixed support as shown in Figure 3.6 (a). The slider is pulled by a motor using a composite string. The portion that winds around a spool[3] connected to the motor axis, is a relatively stiff 1.6 mm brake-wire for bikes, and the remainder which is attached directly to the slider is an elastic nylon string (fishing line) with a thickness (r_{line}) 0.45, 0.60 or 0.70 mm.[4]

The motor we use is a $24V$ (AC) synchronous motor running at about 250 rounds per minute. The motor is driven with AC current from the wall ($250V$, $50Hz$) which is transformed down to $24V$ using a transformer, and then delivered to the motor. A gear-box modified to adjust the motor speed (the gear ratios of the gear-box can be adjusted by changing the number of gears) is connected to the motor. Tests show that the motor delivers a fairly constant speed even when torques within our range of interest are applied. The derivative of the rising force in experiments shows a slight periodicity as we will see later (Figure 3.14). We believe this is due to the fact that the wheels in the gear-box are not 100% fastened and can, apart from rotate, also move slightly in the directions normal to the main axle and thereby cause a periodic variation in the pulling force.

The use of an infrared camera and a microphone, shown in Figure 3.6 (a), is discussed in section 3.3.

Surface properties

After trying a number of different types of carpets/surfaces, we have observed that for different kinds of loop densities and loop compositions in the carpets, there can be two qualitatively different kinds of event behavior.

When the loop density is low, and the loops are made up of single or few threads (as pictured in Figure 3.8 (b)), the events are very brief in time and all the gripping loops seem to loose their connection with the sandpaper whenever the slider moves during the biggest events.[5] In Figure 3.7 an event from an experiment carried out on this kind of carpet is plotted. We have chosen to call this kind of behavior **stick-slip motion (SSM)**. The carpet used in the original paper by Feder and Feder [7] was of this kind.

If we choose a carpet with much higher density of loops, where all the loops are composed of very fine fibers (as pictured in Figure 3.8 (a)), the slider will move in events with longer duration time. We have chosen to call these kind of events "creeps". The event plotted in Figure 3.4 is from an experiment with this type of carpet, and can be categorized as a creep because of its long duration time. In experiments carried out on this kind of surface there will at all times, also during the events, be loops that are hooked to the sandpaper. The slider will,

[3]The spool is 60 mm in diameter and made of brass. Tracks on the spool directs the inelastic wire onto the spool in order to keep a constant pulling speed.

[4]A fishing line is used. The label is Maxima.

[5]For the smallest events the movement of the slider is not observable, but the sound produced by the breaking fibers can easily be heard.

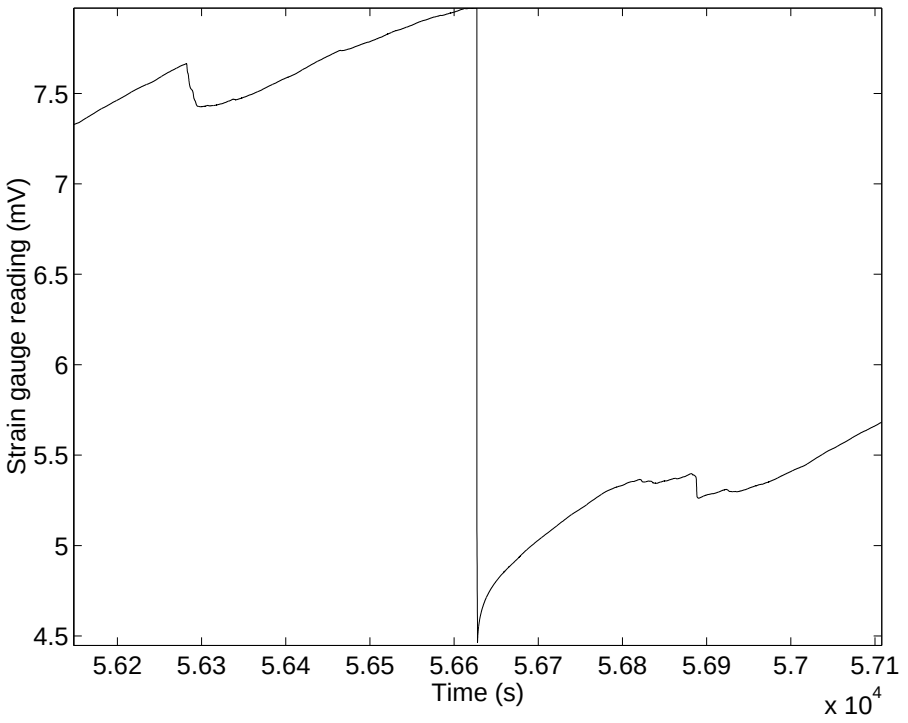

Figure 3.7: A single event (the biggest one in the figure) from an experiment with a low loop-density carpet, that is, a carpet of the type in Figure 3.8 (b), is plotted. Compare the duration time of the event with the event plotted in Figure 3.4.

when slowly driven, exhibit what we have chosen to call **stick-creep motion (SCM)**. The concept of SCM and SSM will be discussed further in chapter 4.

We will primarily report experimental results from two basic experimental configurations. We will call these experiment A and experiment B. The precise configuration of experiment A is :

- Carpet labeled SU4 (blue), pictured in Figure 3.8 (a). This carpet has a high loop density, and will produce events with a long duration time.
- Sandpaper coarseness 60. That is, the average particle diameter is 269 μm (determined by sieving).
- Pulling velocity is 10 μm/s
- Diameter of nylon string is 0.60 mm, length 1100 mm
- Normal force is 0.5 kg

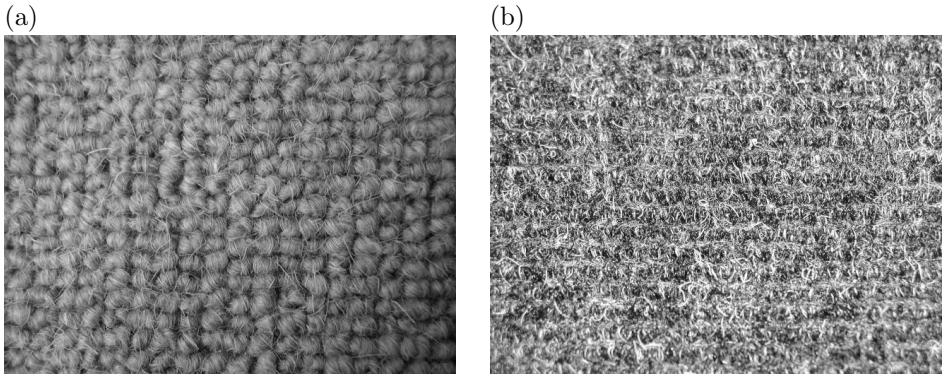

Figure 3.8: Close up pictures of two of the carpets used in the experiments. The high loop-density (producing SCM) carpet used in experiment A is shown in (a), and the low loop-density carpet used in experiment B (producing SSM) is shown in (b).

- Strain gauge LCL-010

We will also report from the basic configuration, called experiment B, which is basically the same as experiment A, but with a different type of carpet. The carpet used in experiment B (pictured in 3.8 (b)) differs from A in the sense that the fiber loops are not bundled together, and that the individual loops are much thicker (lower density of loops) than in A. Regardless of whether the experiment produce SCM or SSM, all "slips" or "creeps" will be referred to as "events".

3.2 Acquiring data

In order to measure and quantify the processes going on between the carpet and the sandpaper, we have been using, as the main measurement instrument, a strain gauge for recording the force required to pull the slider. The basic working of the strain gauge will be explained. We will also in this section discuss other ways to collect information from the experiment, such as using a microphone to record the sound or an infrared camera to get a picture of the dissipation and the geometry of the events.

The strain gauge

Strain gauges are based on a discovery done by Lord Kelvin 150 years ago. He found that conductors subjected to mechanical strain, $\epsilon = \Delta L/L$, where L is the length of the conductor, exhibit a change in their electrical resistance R, ΔR.

This strain sensitivity in the resistance is called the gauge factor (GF) and is given by the unit-less factor:

$$GF = \frac{\Delta R/R}{\epsilon}. \tag{3.2}$$

The gauge consists of a grid, or grids of very fine semiconductor material, with resistance R, bonded to the strained surface by a layer of epoxy. When the surface is strained, the strain is transmitted to the grid material through the adhesive.

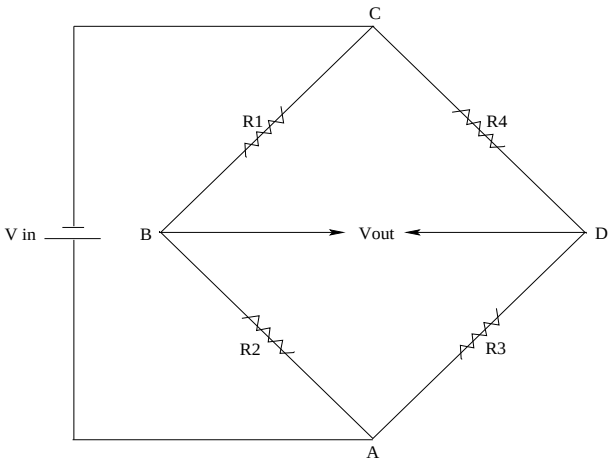

Figure 3.9: A schematic drawing/view of the electronic components inside the LCL-010 strain gauge. When all the resistances are variable (as in the LCL-010 we use), this is called a full Wheatstone bridge.

The strain gauge we used to obtain the force in time ($F(t)$), is a so-called full [Wheatstone] bridge thin-beam load cell, consisting of 4 variable resistances as shown in Figure 3.9. A picture of the strain gauge is shown in Figure 3.10 (a). The potential we measure, V_{out}, is given by (see appendix C for more details about the deduction):

$$V_{out} = V_{in}\left[\frac{R_3}{R_3 + R_4} - \frac{R_2}{R_1 + R_2}\right]. \tag{3.3}$$

Two of the gauges (resistances) are wired in compression and two in tension as pictured in 3.10 (b).

When a force is applied to the beam as illustrated in Figure 3.10 (b), the gauges will either compress or stretch. In this way one can effectively double the bridge output for the same strain. If all R's are equal, V_{out} will vanish. If there is a difference in the resistances, the bridge will become unbalanced and we will measure a potential difference at V_{out} (see equation (3.3)). In appendix

(a) (b)

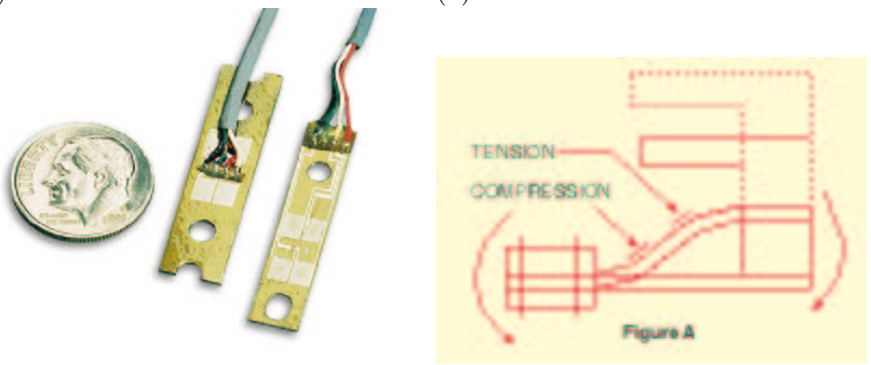

Figure 3.10: To the left (a) is a picture of the LCL-010, where the size is compared to an American dime. Two different gauges are shown, but we use the one to the right in (a). In (b) is an illustration how the gauges are placed in both compression and tension. The pictures are taken from www.omega.com.

C it is also shown that the change in V_{out} is proportional to the sum of the individual changes in the resistances when the tension gauges are on opposite legs (equation (C.8)). With all strain gauges in a bridge at the same temperature and mounted on the same material, any changes in temperature affect all gauges in the same way. Because the temperature changes are identical in the gauges, the ratio of their resistances does not change, and therefore the output voltage of the gauge does not change. This makes the fullbridge strain gauge insensitive to temperature fluctuations. Variations in the temperature does however effect any material by altering their internal structure and therefore their elastic as well as electric properties. This will of course again affect the gauge factor in equation (3.2). Most metallic gauge alloys, however, exhibit a nearly linear gauge factor variation with temperature over a broad range, which is less than $\pm 1\%$ within $\pm 100^0 C$. Consequently we assume, for practical reasons, that the room temperature and the gauge factor is constant in all the experiments.

For the strain gauge to work properly, an excitation voltage of at least 5V DC(max 12V) must be applied across the Wheatstone bridge at V_{in}. According to equation (C.8), the change in output voltage for a given level of strain increases in direct proportion to the excitation voltage. Increasing excitation voltage thus improves signal to noise ratio (SNR), but a practical limit is reached when the ill effects of gauge self-heating become predominant. An optimum excitation voltage is best determined by an experimental procedure:

With no load applied, we examined the zero point of V_{out} while the excitation level, V_{in}, was progressively raised. Once instability in the zero reading was observed, we lowered the excitation until stability returned. We found that the optimal value of V_{in} was very close to $7V$, so this is the value used for V_{in} in all experiments.

The strain gauge used primarily is an Omega LCL-010 thin beam load cell. We used a Metrix AX322 stabilized power supply, for the excitation voltage. The multimeter, a Keithley 2002, records measurements at 13-14 Hz from V_{out} on the bridge, and these are transmitted to a computer by means of a GPIB interface board.

The elastic properties of the system

For any period of time when asperities, that is fibers, in the carpet are gripping on the slider, the system can be simplified and visualized as shown in Figure 3.11. That is, in the experiments the slider is clamped to the carpet such that practically no fibers break while the pulling force increases.[6]

In Figure 3.11, the spring constant k_3 represents the effective spring constant for the strain gauge, k_1 refers to the effective spring constant of the nylon string used for pulling the slider, and k_2 represents the sum of the spring constants for the carpet fibers. The force constants of all the other parts of the system are assumed to be of infinite magnitude compared to k_1, k_2 and k_3. The mass of the slider and the platform are represented by M in the figure. We also have that x_1

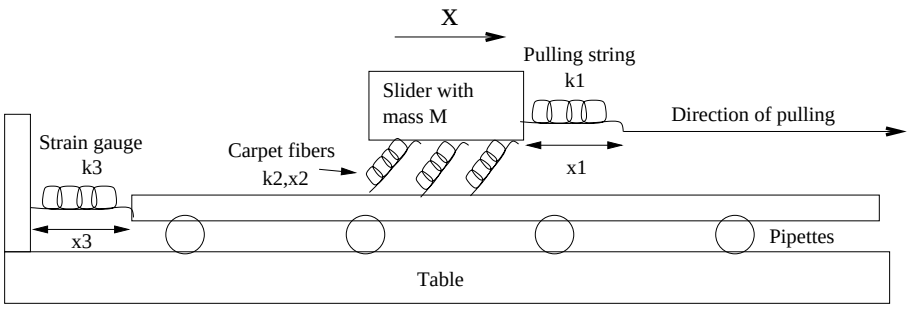

Figure 3.11: A simplified view of the system when the slider is "stuck" to the carpet. That is, the pulling force builds up, while no carpet fibers break. The carpet fibers are imagined to be leaf springs with an effective force constant k_2. All parameters in the figure are described in the text.

is the total amount by which the nylon string is stretched from its equilibrium length, x_3 is the total amount by which the strain gauge (SG) is deflected from its straight equilibrium configuration, and x_2 is the mean elongation of the gripping carpet fibers.[7]

Assuming the motor pulls with a constant average velocity v, and that all "springs" begin at their equilibrium lengths, then:

- The force measured is $k_3 x_3$ (in the left direction).

[6]This is often the case at the start of experiments. The force then builds up to a value much higher than the stationary value, before dropping down. This can be seen in Figure 3.3.

[7]Note that no sub index is used to symbolize the different x's in the figure.

- The force applied to the system is $k_1 x_1$ (in the right direction).
- At rest we have $k_1 x_1 = k_3 x_3$ (whatever value of x_2, that is $k_2 x_2 = k_1 x_1 = k_3 x_3$).
- The total elongation of the nylon line, strain gauge and the carpet fibers after a time t is $x_1 + x_2 + x_3$, is equal to the distance pulled by the motor, vt.

In other words we have the following equations:

$$x_1 = \frac{k_3}{k_1} x_3 \tag{3.4}$$

$$x_2 = \frac{k_3}{k_2} x_3 \tag{3.5}$$

$$x_1 + x_2 + x_3 = x_3 \left(\frac{k_3}{k_1} + \frac{k_3}{k_2} + 1 \right) = vt. \tag{3.6}$$

We can then write:

$$x_3(t) = \frac{k_1 vt}{k_1 + k_3 + \frac{k_1}{k_2} k_3} = \sigma t \ , \tag{3.7}$$

where $\sigma = \frac{v k_1}{k_1 + k_3 + \frac{k_1}{k_2} k_3}$. The value of σ is the rate at which strain gauge is deflected when the slider is "stuck" to the platform and the attached fibers and the nylon string are stretching (see slope of plot in Figure 3.13). By measuring the output (in mV) of the strain gauge as a function of applied weight we found a conversion from units of Volts to units of Newton. We found that 1V of output from the strain gauge corresponds to ∼3.6N of applied force.

We measured the value of k_1 by putting a heavy load (about 5kg) on a scale and then lifting it with the elastic nylon string (0.70 mm in diameter and 1150 mm long). The weight of the load and the elongation of the string were recorded at discrete steps. Between each measurement the string was allowed to "relax" for about 5 minutes before the measurement was made (see Figure 3.12). The value of k_1 was found to be ∼500N/m.

A rough estimate of the effective spring constant of the strain gauge can be found by considering the full deflection and the maximum load of the gauge. A full scale deflection of the strain gauge is about 1.3mm, and the maximum load is about 4.5kg.[8] The value of k_3 ∼4.5*9.8/0.0013 N/m ∼ 30 kN/m, which is about 60 times larger than k_1. The idea of using the rather elastic nylon string is to ensure that the pulling force remains nearly constant throughout a slip event.

By inspecting the slope in Figure 3.13 we find that the tension rise (in the no-slip case) is about $9 \times 10^{-3} V / 4000 s \times 3.6 N/V \sim 8 \times 10^{-6}$N/s. We then needed to make an estimate for how much deflection of the strain gauge this tension rise

[8] Data is supplied by the vendor (Omega).

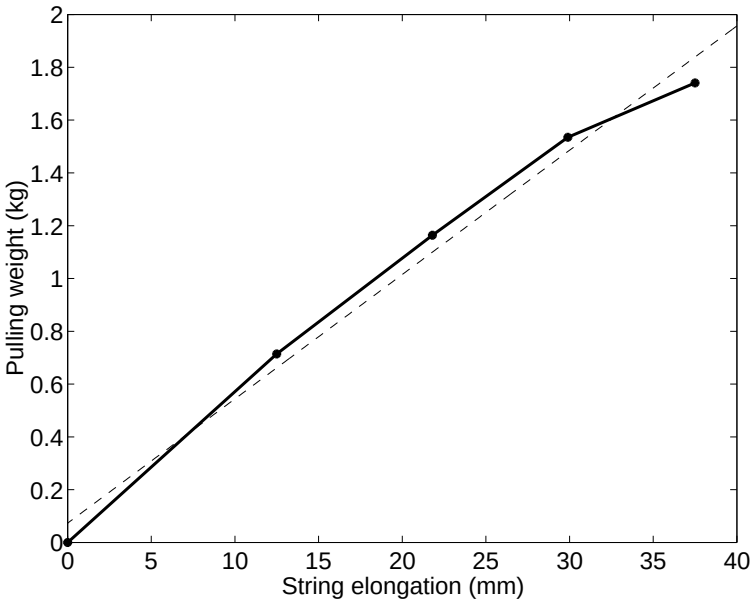

Figure 3.12: The elongation of the pulling string (0.7mm in diameter) as the function of the load. A linear regression to the data gives a slope of about 500N/m, which is the effective spring constant of the string.

corresponds to. Again we used a rough estimate: we assume that a full deflection (at $\sim 45N$) of the gauge corresponds to about 1.3mm. We can then estimate that $\sigma \sim 8 \times 10^{-6} N/s \times 1.3 \times 10^{-3} m/45N \sim 2 \times 10^{-10} m/s$. We are now in a position to estimate k_2 as well. We separate k_2 from the expression for σ in equation (3.7):

$$k_2 = \left(\frac{1}{k_3} \left(\frac{v}{\sigma} - 1 \right) - \frac{1}{k_1} \right)^{-1}, \tag{3.8}$$

and insert the values of $v = 10 \times 10^{-6} m/s$, k_1=500N/m, k_3=30kN/m and $\sigma = 2 \times 10^{-10}$m/s into this expression. We then get a value of $k_2 \sim k_3 \sigma / v \sim \frac{6 \times 10^{-6}}{10^{-5}} \sim 3/5$N/m, which means that $k_3 > k_1 \gg k_2$. This, rather unexpected small value for k_2 might have its origin in the fact that the total number of fibers that are connected to the slider is not constant. That is, fibers break and regrip all the time, altering the value of k_2, without us being able to resolve it.

From the Figures 3.12 and 3.13 we observe that the slope is not fully constant at all times, as it should be according to equation (3.7) if the elastic properties of the system were constant and linear. Deviation from a linear slope in the force in time curve show in the figures may have various origins:[9]

[9]We would expect a linear slope, according to linear elasticity theory, if we assume that all force constants in the system were linear (for small strains).

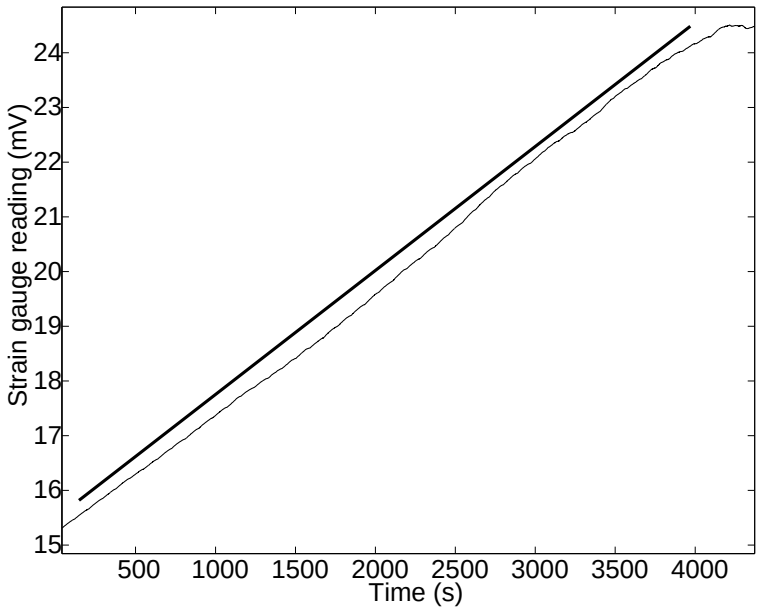

Figure 3.13: The tension rise is illustrated for a normal experiment where the slider sticks to the carpet (no-slip case) and the nylon string is fastened to the wire (thin solid line). The fat solid line is a linear fit, with a slope of about $\sim 8 \times 10^{-7} N/s$, to the tension rise. We observe slight changes in the slope as the force increases, indicating that the elastic properties of the system are not perfectly constant, or we may have nonlinear responses as the stress builds up. Changes in the slope may also be caused by small slips (this is discussed in more detail later).

- Possible non-linear elastic properties of components in the apparatus. All the force constants, k_1, k_2 and k_3 may have strong temperature dependencies. This has not been investigated further.

- Our assumption that the high gear ratio in the gear-box causes the motor to operate with a torque less than its maximum torque, may not be true, and the motor can be overloaded for high pulling forces. See Figure 3.14 for the instantaneous derivative of the signal when the pulling wire is fastened directly to the slider platform.

- As the force builds up, an increased number of contacts between the slider and the carpet is possible. This will alter the force constant k_2 in the system and thereby the slope in Figure 3.13.

- The steel wire we have used is practically non-elastic, but small damage, or bends to the wire may drastically alter its elasticity.

If we take a closer look at the instantaneous derivatives of the strain gauge readings in the same experiment as shown in Figure 3.13, we obtain the plot shown in Figure 3.14. In this plot we find regular fluctuations in the derivative that perhaps can be ascribed to the total force supplied by the motor. We know that the wheels inside the gear-box are not perfectly fastened to the gear-box: if we apply tangential force to a wheel inside the gear-box, we can slightly displace it. By using a larger and more solid driving system, we might diminish

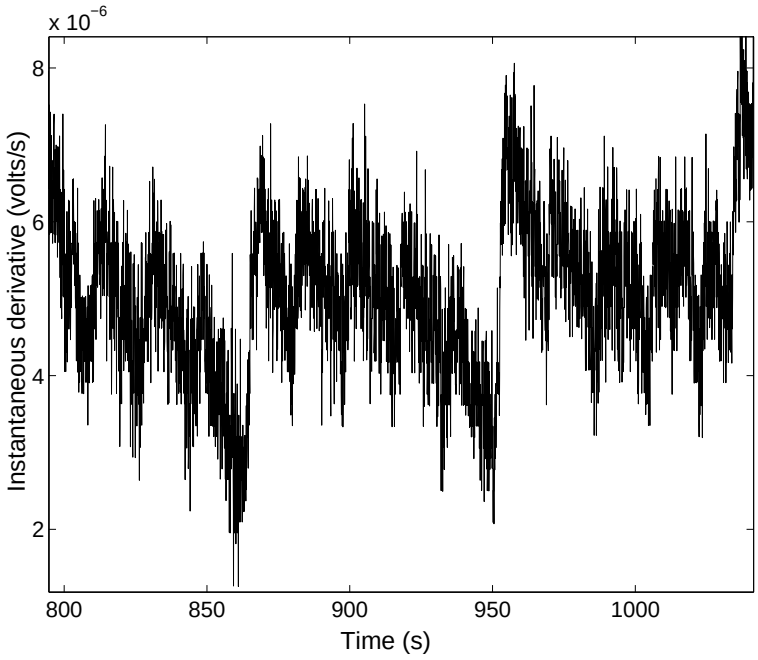

Figure 3.14: The derivatives of the strain gauge measurements when the string is attached directly to the platform. Note the multiple periodicity in the signal, which may originate from fluctuations in the force that is supplied by the motor.

the unwanted fluctuations in the derivative of the buildup shown in Figure 3.14. However, we believe the small variations in driving force have a minimal effect on event sizes we calculate in the experiments.

Noise analysis

The DC signal that we measure (V_{out}) from the strain gauge ranges from several mV to about 30 mV for the largest force. The largest pulling force corresponds to about 50 N. The multimeter gives us a nominal resolution of 1 nV, that is 1×10^{-9}V. The force measurements will therefore theoretically give us a dynamical range of about 7 orders of magnitude. However, two main source of

noise – electrical and mechanical – put a limit to the practical dynamic range we can resolve.

Unwanted signals or noise provide natural limits to the precision that can be achieved and may have many sources such as pickup from the main power lines, interference by nearby electrical machinery, spurious signals due to bad electrical contacts, thermocouples and faulty electronic components. Mechanical sources of noise can for example be vibrations or faulty components in the experimental setup or disturbances such as air movement. The mechanical noise is found to dominate over the electrical noise.

Electronic sources of noise

Thermoelectric effects occur at the junction between two metals. A voltage V, which is a function of the temperature difference, ΔT, is created over the junction:

$$V = k\Delta T. \tag{3.9}$$

The value of k can be found from empirical data tables for specific metals.[10] A copper-constantan connection produces a voltage about 40 $\mu V/^0C$ while a copper-solder connection about $3\mu V/^0C$. Thermoelectric effects can be reduced by using similar metals to as high a degree as possible.

Magnetically induced voltages may occur when the wiring is located in a time varying magnetic field. Examples of typical sources of induced voltages are electrical equipment like computers, power supplies or other current carrying wires. Besides moving the wiring as far as possible from the mentioned sources, using shielded twisted pair cables and forming minimum but equal loop areas on each side of the fullbridge, helps in controlling these external noise sources.

After reducing the thermocouple and the magnetically induced noise effects as suggested above, we have undertaken several experiments to locate and quantify other origins of noise in V_{out}. In these experiments there was no strain applied to the strain gauge, and the mean amplitude of the noise fluctuations was measured for different configurations of the circuit and apparatus.

The raw noise-signal for the best configuration (that is, strain gauge dismounted and placed in a thermos bottle) is shown in Figure 3.15 . On average, and without any special steps taken, such as insulating the strain gauge, we find for the chosen configuration of the circuit that about 99 % of all noise fluctuations are less than 2×10^{-7} V in amplitude, the mean absolute amplitude of the noise is about 8×10^{-8} V and the standard deviation is about 5×10^{-8} V.

If we plot the distribution of these noise amplitudes, we observe in Figures 3.16 (a) and (b) that the noise amplitudes are Gaussian distributed, except for in the highest absolute amplitudes where it deviates somewhat from the normal distribution.

By looking at the Fourier-transformed signal, we can tell whether the noise has some hidden periodic component and whether there are correlations in the signal. This can be done by calculating the power spectrum density, using the

[10] Also called the Seebeck coefficient.

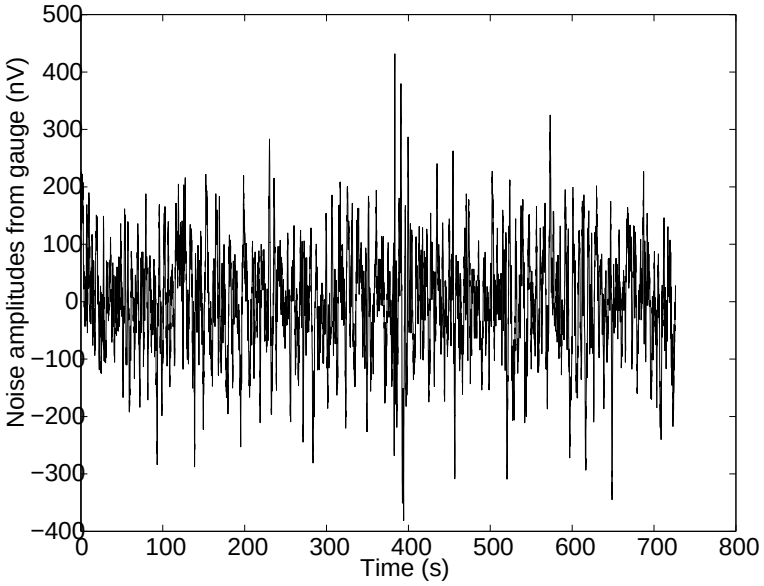

Figure 3.15: Readings from the strain gauge, while the gauge is dismounted and placed within a thermos bottle.

Periodogram method explained in appendix D. The power spectrum density of the signal with the chosen configuration, that is dismounted and inside a thermos bottle, is shown in Figure 3.17. Note that in Figure 3.17 the four round peaks which have their maximum values at 11,19,27 and 35 mHz. These peaks do not occur when we use a battery instead of the power supply across V_{in}. We therefore believe that these high in frequency, but low in amplitude, components of the noise arise from the intrinsic noise of the power supply. However, using a relatively stable supply (a 9V battery) will not diminish the amount of noise in the output signal, but rather lead to a drift in V_{out}.

To try and rationalize the observed fluctuations in the signal, we have to look deeper into the physics of the components of the circuit. Whenever some parameter of a more or less dynamic system is observed in a thermal environment, such as moving electrons in a resistor, we must expect to find fluctuations or noise in that parameter. This noise depends directly on the irreversible "viscosity" or "friction" (here resistance) which that variable is subjected to, and also on the temperature of the environment. This phenomenon got its name, "Johnson noise" from experiments done by J. B. Johnson in 1928, and was later explained by H. Nyquist in 1928 [41, 42]. The magnitude of Johnson noise V_j in a source resistance is given by (see [43]):

$$V_j = \sqrt{4kTR\Delta f}, \tag{3.10}$$

where k is Boltzmann's constant ($1.38 \times 10^{-23} J/K$), T is the absolute temper-

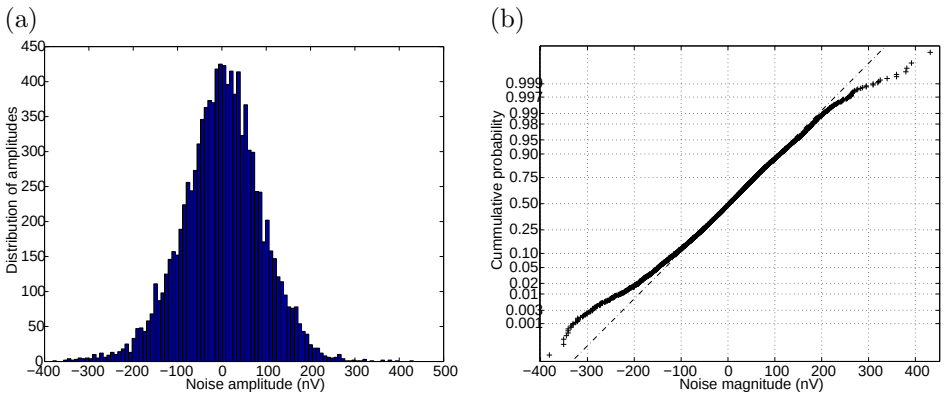

Figure 3.16: (a) An histogram of noise amplitudes shows in what range of voltage magnitudes we can expect noise in our system. The amplitudes are calculated by subtracting values on a baseline that represent a local average (see Figure 3.15(b)) from the raw signal. (b) The cumulative distribution of a pure Gaussian variable is plotted in dashed line (–), and the noise amplitudes are plotted as crosses (++). The purpose of a normal probability plot is to graphically assess whether the noise amplitudes could come from a normal distribution. If the data is normal, the plot will be linear. Other distribution types will introduce curvature in the plot.

ature of the resistance (assumed to be not much above room temperature, or 300 K), R is the resistance (about 1000 ohms for the individual strain gauge resistances), and Δf is the noise bandwidth in Hz (about one half the conversion rate [readings per second] of the integrating digital voltmeter, in this case about 7 Hz). Thus, for one of the resistances (about $1k\Omega$), V_j is approximately 1.073×10^{-8} V, more than a full order of magnitude lower than the largest measured fluctuations. We know that there are at least 4 such sources of noise (resistors) in the strain gauge, but these couldn't account for all the observed noise. The amount of noise can be diminished slightly (by only about 1×10^{-8} V) by insulating the strain gauge in a thermosbottle and by waiting at least two hours after starting the input voltage.

Noise performance specifications for the Keithley 2182 nanovoltmeter (a more sensitive apparatus than the one we used) indicates that the intrinsic noise of the apparatus is between 3.5×10^{-8} V and 7.0×10^{-8} V. We have not been able to obtain an estimation of the intrinsic noise of the multimeter (2002) we used, but we have reasons to believe that the amount of intrinsic noise is slightly higher in the 2002 we used than in the 2182 nanovoltmeter.

The period of time over which the multimeter averages the analog signal from the strain gauge between each digital output has a significant influence on the total noise in the signal. When the rate of measurements is doubled on the Keithley 2002 (our instrument) from 13Hz to 26 Hz, the magnitude of the largest noise fluctuations is increased by two orders of magnitude. We therefore

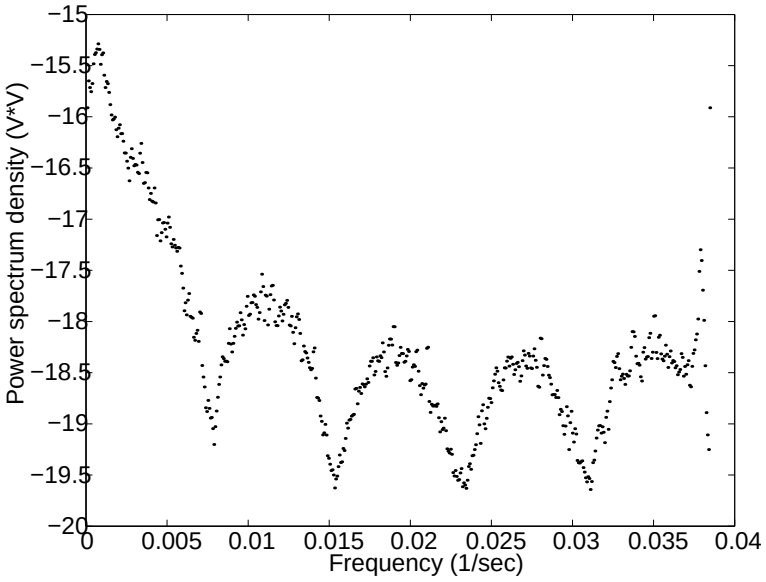

Figure 3.17: The power spectrum of the signal obtained using the periodogram method , plotted on a single-log plot(along the y axis). Four frequency peaks are observed, and are believed to arise from the power supply because they do not show up in experiments where a battery is used as an excitation source.

selected a rate of measuring (as a compromise between resolution and noise) of 13Hz.

To summarize, we believe the least noisy configuration of the electronic components in the experiment is achieved using shielded and twisted-pair cables grounded (only at one place) to the negative input of the multimeter, placing the system as far as possible from electronic noise sources, using metals on both sides of connections that are as similar as possible.

Mechanical sources of noise

When we mount the strain gauge, other sources of noise suddenly start to become prominent. Vibrations in the table the experiment rests on, and varying air movements around the sliding board will cause unwanted strains in the gauge when the gauge is mounted. When the strain gauge is mounted to the support but disconnected from the moving board, the mean absolute value and the absolute standard deviation of the noise amplitudes lies close to $2.5 \times 10^{-7} V = 250$ nV. When the strain gauge is connected to the moving board as well, as it is during the experiments, both the standard deviation and mean noise amplitude increases to about $3.5 \times 10^{-7} V = 350$ nV.

This means that the major source of noise in experiments comes from me-

chanical sources and temperature variations. Efforts to reduce this kind of noise could include isolating the whole system in a glass chamber and putting the whole setup on a stabilized table. This has not been done.

3.3 Simultaneous measurements

As mentioned earlier, we have explored novel methods of acquiring details about the complex dynamics believed to govern the physics of stick-slip motion and stick-creep motion. The methods of measuring events discussed in this section are independent of whether the motion is of the stick-creep or stick-slip type, and these will be referred to as just "events".

Using only the force readings from the strain gauge, we are given limited access to the fine temporal and spatial details of the friction dynamics. We cannot, for instance, say anything about the geometry of the events. Neither can we, because of slow reading rate and because of the ever present noise, resolve the smallest events that are too fast, or too small to be recognized by our naive way of measuring their magnitude.

In this section we describe a procedure for obtaining simultaneous measurements of displacement, sound, and temperature in the carpet experiment. That is, to the strain-gauge measurements we have added spatio-temporal measurements of the temperature of fibers in the carpet, using an infrared camera, as well as the displacement of the slider (also from the camera images), and the sound produced by the events is measured using a microphone (see Figure 3.19). These simultaneous measurements, when conducted in the regime of very slowly-driven motion, will enable us to determine more accurately the duration, geometry and magnitude of the events that occur in SSM and SCM. An estimation of the total energy dissipated in individual events will also be made possible using these methods.

Difficulty with measuring all events

In the previous section (3.1) we described the procedure used to measure the magnitudes of the SSM and SCM events from the strain gauge signal, $F(t)$. This procedure has an important shortcoming. That is, there are many small-magnitude events that merely modify the otherwise constant slope of the rise in tension as a motor pulls on the slider when it is stuck. These small events are examples of stick-creep motion (SCM), in which at least some fibers are at all times attached to the slider. Since the derivative $F'(t)$ of the force in time does not become negative during these minute creep events, they are not counted.[11] A more correct method calculating the magnitude of the events would also include a procedure for quantifying slips where $F'(t)$ does not become negative. These attempts at more sophisticated methods for calculating the magnitudes of events from the $F(t)$ data are frustrated by fluctuations in the slope of the tension rise that occur for different reasons. The other causes for fluctuations

[11] see the definition of a event on page 28

in F', apart from the smallest events, can include electrical noise as well as any marked change in the number of attached asperities, because this will modify the elastic properties of the interaction between the slider and the carpet.

Noise from the motor

We sometimes find a regular pattern in the fluctuations in F' (see Figure 3.18, and 3.14), which we believe are caused by the wheels in the gear-box. Attempts at developing more sophisticated methods for measuring event magnitudes, in which the onset of an event is indicated by a sudden decrease in the value of F' instead of a change in sign, have so far been frustrated by these fluctuations.

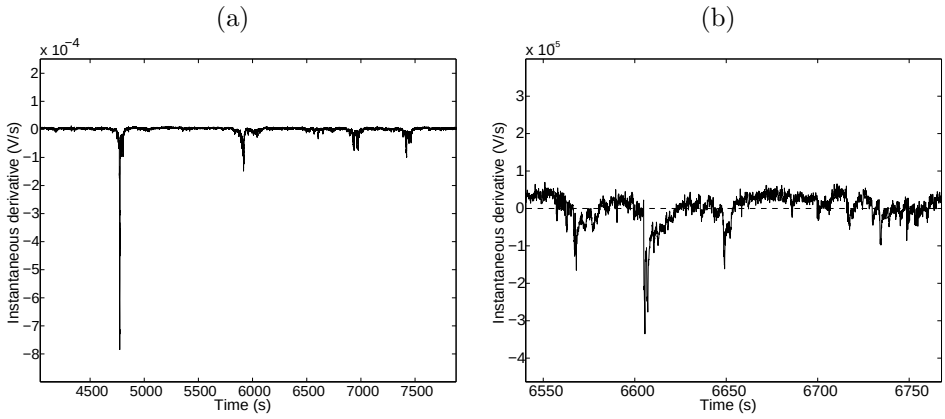

Figure 3.18: (a) shows the instantaneous derivatives of experiment A (the exact configuration used to obtain data for experiment A is supplied on page 33). Events can easily be observed in the signal as clusters of negative values, however, when the signal is magnified (b) we find wild fluctuations that makes the task of calculating the event magnitudes very difficult.

Measuring events using a microphone

Sound measurements, obtained using a microphone, 10 mm × 10 mm, mounted inside the slider immediately above the sandpaper, can be used to detect the snapping sound (a "click") of even a single fiber losing its grip to the sandpaper, or breaking.[12] A picture of the slider with the microphone mounted on it can be seen in Figure 3.19. The sound is sampled at 44.1 kHz, with a resolution of 16 bits, using a Creative Labs Sound Blaster card in a PC. In Figure 3.20 the sound amplitudes (top) are plotted together with the strain gauge readings (bottom) for the first big event in a slowly driven experiment.

[12]The microphone is taken from an Ericsson T-65 mobile telephone.

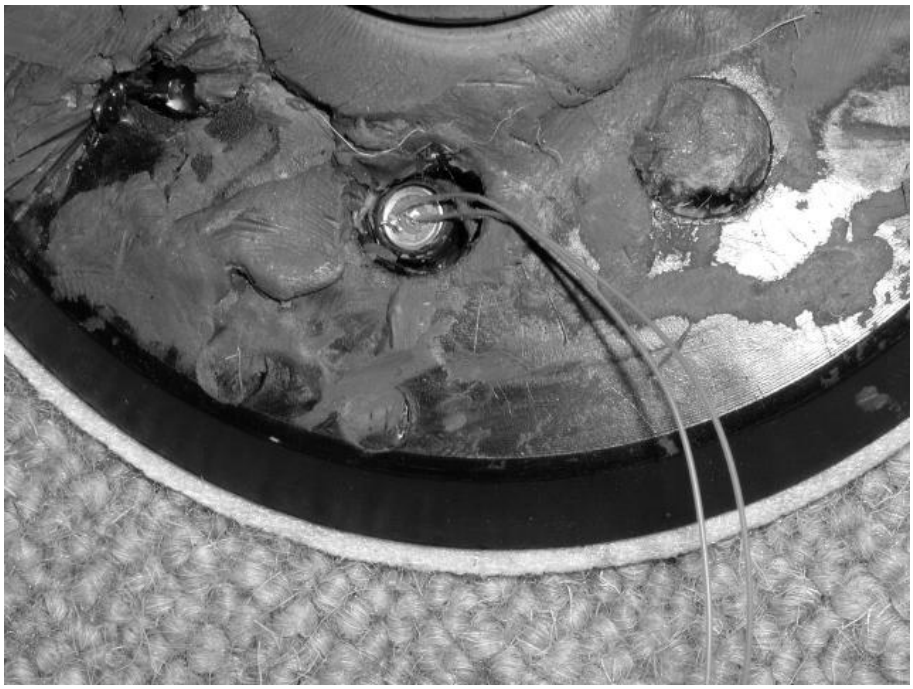

Figure 3.19: A picture of the microphone mounted inside one of the holes in the slider. The microphone is mounted such that the membrane lies right above the sandpaper without touching it. The microphone is 10x10 mm in size. The two wires sticking out are connected to a soundcard in a PC.

A practical problem when recording sound at 16 bit and 44kHz, is the huge amount of sound data that is created. For practical reasons we therefore rely on methods to extract only the useful sound information, that is, only those sound amplitudes (samples) that are greater than the sound amplitudes produced by the background are saved. This is done by thresholding the sound amplitudes data as follows:

- the sound is recorded into 40 second-buffers which is then read into Matlab (using wavread).

- In Matlab, all sound amplitudes (absolute values) greater than 0.01, that is, those that corresponds to the clicking sounds, are kept in a matrix, while the rest is thrown away. Sound amplitudes lie between -1 and 1, and when the slider is at rest, all of the amplitudes are less than ± 0.01.

- The time, which is the sample number divided by the sampling frequency, at which the amplitudes occur, is kept in another matrix.

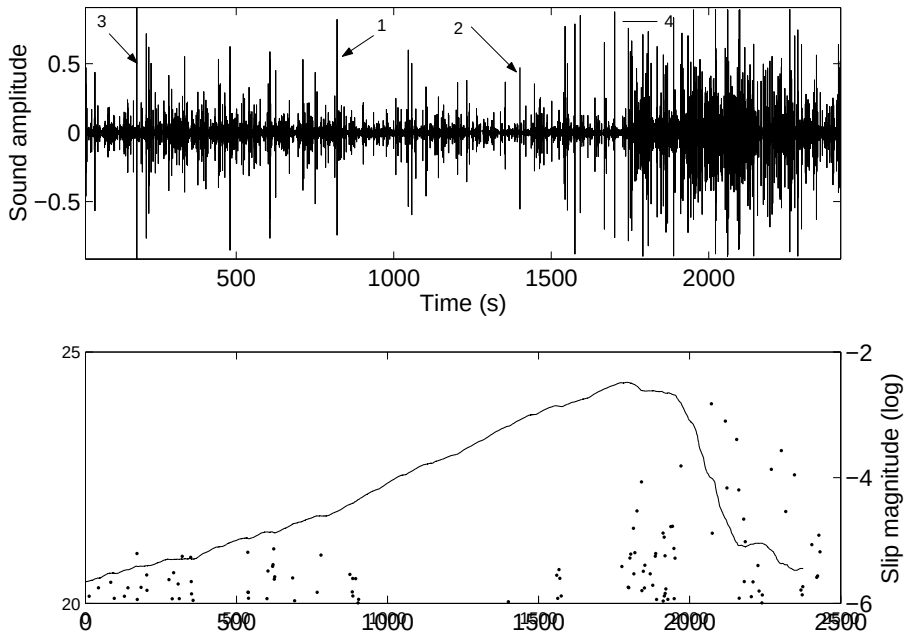

Figure 3.20: The force in time (bottom) is plotted in solid, while the event magnitudes, calculated using the scheme described in the text, are plotted with dots. The sound recorded with a microphone (top) is plotted for the same experiment. Four of the events are marked and zoomed in on (in the audio data) as shown in Figure 3.21.

This method of sampling drastically reduces the amount of sound data. The biggest problem regarding this way of "filtering" out the irrelevant data, is that time is "lost", due to input/output processes in the recording PC, when the buffer (which is eventually put to a file before being read into Matlab) is initiated. Correlating the sound data to the strain gauge reading is, because of this "loss" of time, hard to accomplish. However, this could be solved by recording the sound directly into the memory using Matlab, and then treating the sound data without first writing it to a file.

Clicking sounds produced by breaking fibers

Each "click" (sound) produced by a breaking fiber will produce a characteristic sound that can be heard when listening carefully. These "clicks" are in great detail picked up by the microphone. The four "clicks" that are pointed at in Figure 3.20(top) are shown in Figure 3.21. One see from these figures that the audio signal is made up of individual pulses that have different shapes (plot 1,2 and 6). Each of these pulses are believed to be the result of a breaking fiber. The temporal resolution of the audio samples is high enough to discern individual

breakings of fibers. In plot 4, a region with a seemingly very high density of pulses, is zoomed in on. In plot 5, a selected region with a high density of events from plot 4 (marked) is magnified and further zoomed in on in plot 6. This suggests that we can study how and when individual fibers break.

By comparing the starting times of the pulses obtained from the sound data and those obtained from $F(t)$, one can use more sophisticated methods of finding the size and the magnitude of the events. Using the sound data, it is also possible to decide whether an event is really caused by frictional processes or if it is just a result of intrinsic noise in the gauge reading. That is, event magnitudes calculated from $F(t)$ that are smaller than what we assume to be the noise threshold (about 3.5×10^{-7} V) can be tested against the sound data to see if really is an event. However, this depends on a correct timing between the clock of the sound recorder and the clock on the multimeter.

The energy dissipated in a breaking fiber

By integrating over the square of the amplitudes that constitute a pulse, we can calculate some of the energy that is dissipated when a fiber breaks. When using only one microphone, attenuation of the sound across the slider is a problem. The amplitude of a sound wave produced by a breaking fiber (a "click") which is received at the microphone, depends on the position of the breaking fiber. That is, the sound amplitude is proportional to the distance from the microphone. A calculated "click"-energy will therefore depend on where the breaking fiber is, relative to the microphone. It is possible to combine several microphones, and distribute them throughout the slider and then analyze the signal much as is done in seismic arrays. In this way, we can possibly locate the breaking fiber and calculate the energy independent of the location of the fiber. This has not yet been explored and is left for future projects.

Because of the low strain gauge sampling rate (13 Hz), an event calculated using the strain gauge, will normally consist of a great number of pulses (or "clicks"). That is, as we saw from the plots in Figure 3.21, the "macroscopic" events, those event magnitudes measured with the strain gauge, can from the audio data be divided into a large number of pulses. One could imagine that there at least has to be a certain number of pulses (fibers breaking) within the strain gauge sampling interval for us to be able measure it as an event (using the strain gauge). This number pulses then has to be a function of the sampling frequency and would therefore be strongly dependent on the force-measuring apparatus. In the ultimate apparatus we should be able to measure, from $F(t)$ and its derivative, the magnitude single fibers breaking. The question is then, if we used only a microphone to determine the event magnitudes, how much time will we allow between separate pulses in order to merge them into one event magnitude? Will the distribution of events be dependent on how much time we allow between pulses? These are questions that will be put on hold for future projects.

Moreover, these sound measurements can be obtained at rates very much higher than what is customary for our strain-gauge measurements (44.1 kHz

as opposed to 13 Hz). Therefore, the sound measurements can be correlated with the strain-gauge measurements and used to determine more accurately the starting and ending times of SCM or SSM events. These measurements can therefore be used to produce an accurate distribution in the time that elapses between subsequent events (which may also exhibit power-law behavior) and can assist with computing more accurately the distributions of event magnitudes and lifetimes from the $F(t)$ measurements.

Analyzing the events using the sound data

We have analyzed the sound data recorded in the experiment shown in Figure 3.20. Because of the large temporal resolution of the sound data (44kHz) it is not clear how much time, ΔT, we shall allow between two pulses ("clicks") in order to merge them into one event. One pulse is a sequence of the sound amplitudes that is greater than the background noise. Examples of pulses are shown in Figure 3.21 1,2 and 6.

We have studied how the distribution of event magnitudes, waiting times and duration times varies with ΔT. The values chosen for ΔT are 1,10,100,1000,10000, 25000 and 50000 samples (one sample is 1/44100 second). This yields respectively about 150000, 98000, 73000, 23000, 8000 and 2500 events. The event magnitudes are calculated by summing the absolute values of all the sound amplitudes in the merged pulses.

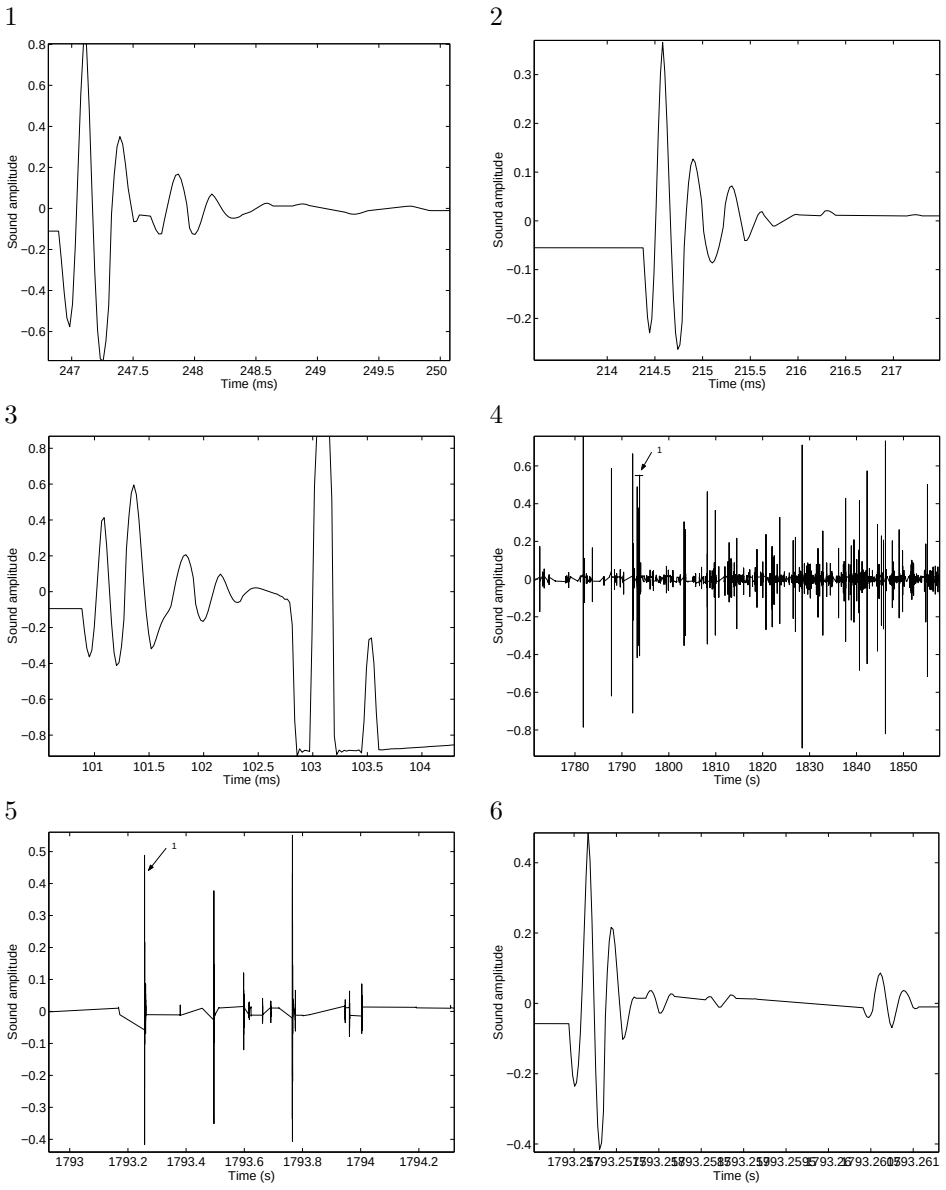

Figure 3.21: The figures are named according to the marked events in Figure 3.20. Each of numbered event are zoomed in on. In plot 4, a range of "clicks" has been magnified, and one can observe the great number of "clicks", or pulses which constitute the signal. A marked region (1) in plot 4 has been further magnified and plotted in plot 5. A single pulse in plot 5 has been selected and magnified in plot 6. We believe the pulses seen in plot 1,2,3 and 6 are produced by the breaking of single fibers.

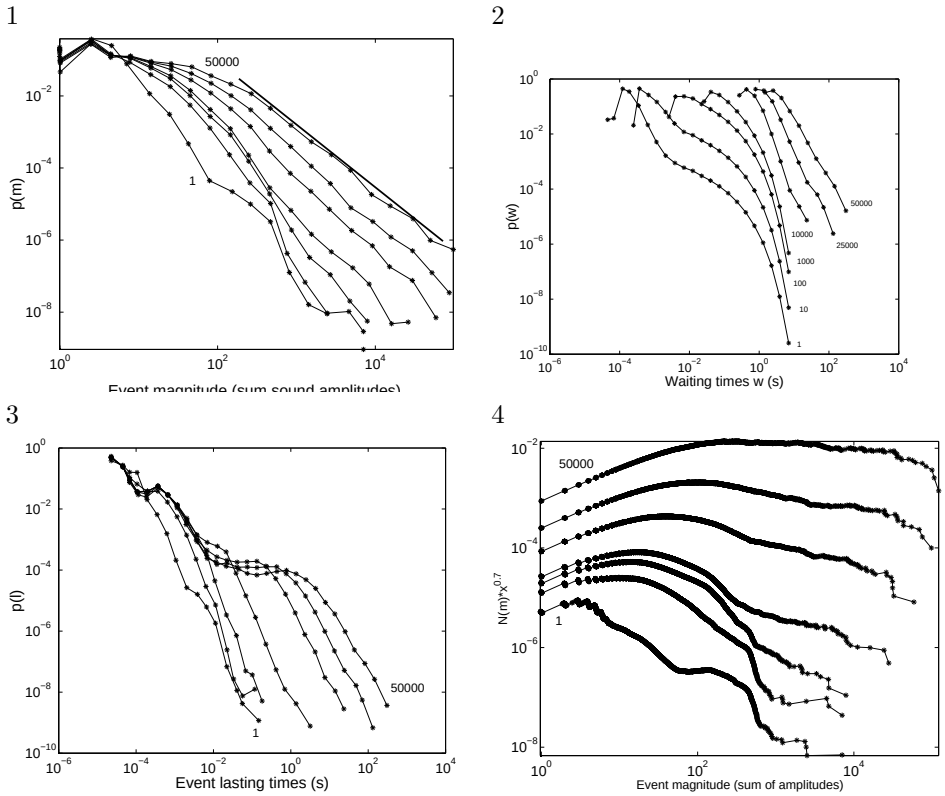

Figure 3.22: Probability density of event magnitudes, waiting times and lasting times are plotted figure 1,2 and 3 respectively. We see that the value of ΔT increases from the bottom curve ($\Delta T = 1$) and to the top curve ($\Delta T = 50000$). In figure 4 the scaled (with $m^0.7$) cumulative distribution of event magnitudes is plotted. For the largest events and the largest value of ΔT the distributions resemble power laws. It is striking that the slope of the power law is close to the values found from the force in time data when ΔT is close to the sampling rate from the strain gauge (1/13 s).

Measuring the dissipation using an infrared camera

In order to measure the temperature of the carpet fibers in real-time we used a semi-transparent slider consisting of a rigid metal grid that is coated with sand grains that have been glued on using an epoxy adhesive. The square holes in the grid are approximately 2.5 mm in diameter, whereas the grid lines are approximately 0.5 mm in thickness. The entire grid is just 5 cm by 5 cm in total size. A frame was constructed from LEGO^{TM} components and was mounted on the metal frame supporting the grid, and this was used to carry a load of 400g. An infrared camera with 300x240 pixel resolution was used to take six images per second as the slider was dragged across the carpet surface. This camera is very expensive and was rented for a week. Normal temperature resolution is $\pm 0.01^0$C. In this way we measured the range in temperatures on the carpet surface in time (Figure 3.24), as well as the mean temperature as in Figure 3.25. This makes it possible to estimate the amount of energy dissipated in the form of heat.

These measurements also enable us to visualize the geometry of the regions of asperities involved in events as in Figures 3.27 and 3.28. These regions are not contiguous and do not seem to propagate, in contrast to previous suggestions [7, 25]. It must be remembered, however, that the motion is not driven slowly enough that we should expect this kind of behavior. In order to determine exactly the geometry of regions involved in stick-creep motion (SCM) and stick-slip motion (SSM) events, a relatively smooth carpet would be needed: that is, fiber and fiber-bundles of the same height, so that it becomes possible for neighboring asperities to attach themselves to the slider. Moreover, a larger grid is needed in order to increase the number of fibers that are gripping at any given time. A camera with greater temporal resolution could then be used to visualize the geometry of slipping regions and the manner in which these regions evolve on short time-scales.

We found a characteristic infrared signature that corresponds to the edge of the grid in each image (Figure 3.29). The camera position was adjusted in just one direction after each event, and therefore it was possible to use the image data to measure the displacement of the grid in time (Figure 3.30). These displacement measurements provide still another way to quantify the magnitude of events and to get a glimpse of the dissipation in the system.

Unfortunately, since the camera we used had a spatial and temporal resolution that was relatively small (6 frames per second, 4 pixels/mm), the displacement that occurs in the vast majority of small events cannot be measured in this way. Using special hardware, it is possible to take pictures as fast as 40 frames per second. When taking pictures so rapidly, one must develop smart methods for triggering the camera to start recording only when an event is under way. This triggering can be accomplished using information from the microphone or the force data.

The infrared camera was also used to capture the regions left behind by the slider after massive stick-slip events. The camera was not moved with respect to the carpet, so that product images could be used to determine which of the

fibers become hot in subsequent events. In this way it was discovered that many of the same fibers are involved in subsequent events, probably owing to their greater height with respect to neighboring fibers (see Figure 3.31).

In the remaining sections of this thesis we refer only to the strain gauge measurements, obtained using the opaque sandpaper slider driven at 10 μm/second.

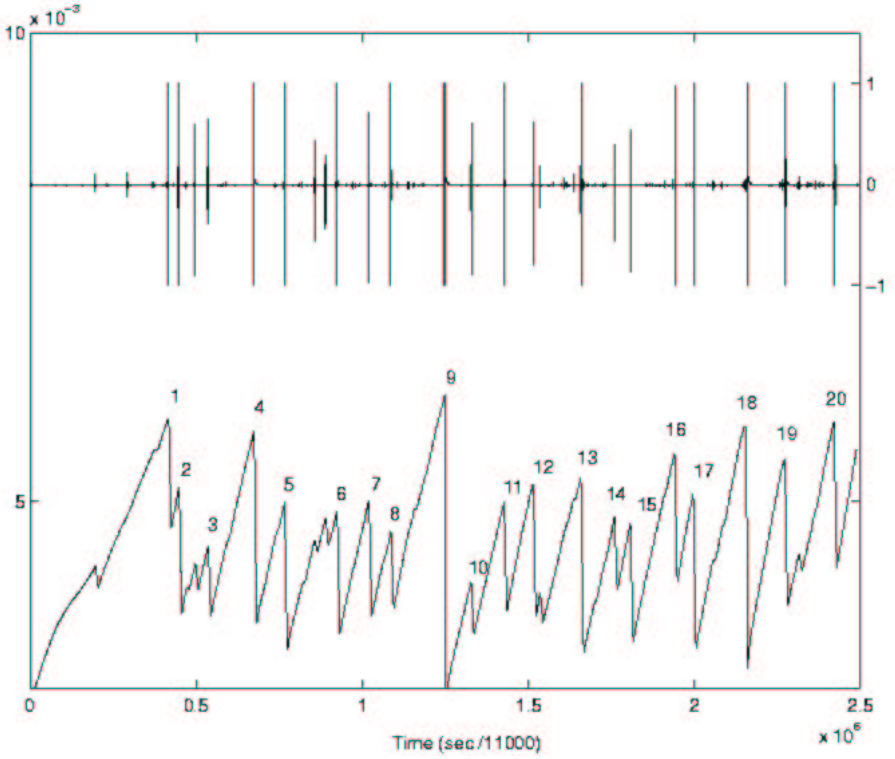

Figure 3.23: Sound (top) and force (voltage measured across a strain-gauge, bottom) recorded while driving the "grid-sandpaper" across 35 cm at 1.6 mm/sec. Twenty prominent events are labeled in this figure. The same events are also labeled in Figures 3.24 and 3.30.

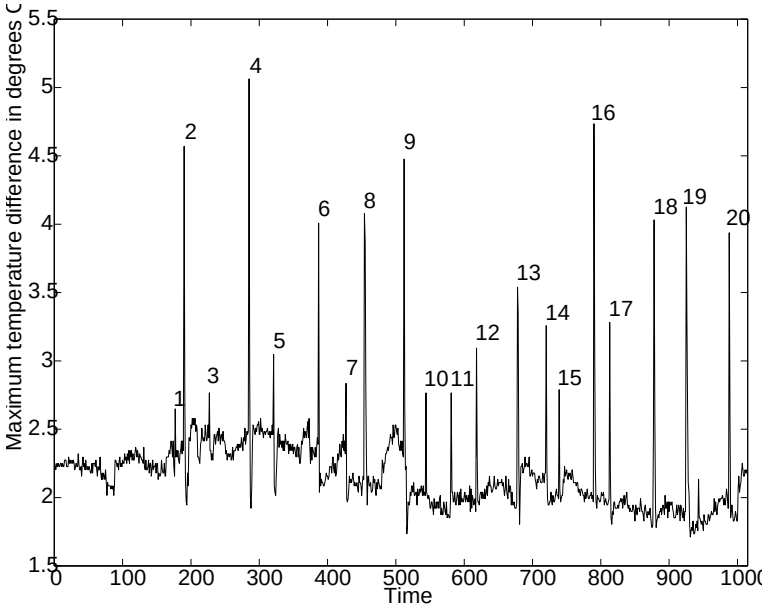

Figure 3.24: Maximum temperature range of each infrared image in a series of 1015 images, acquired at the rate of approximately six per second.

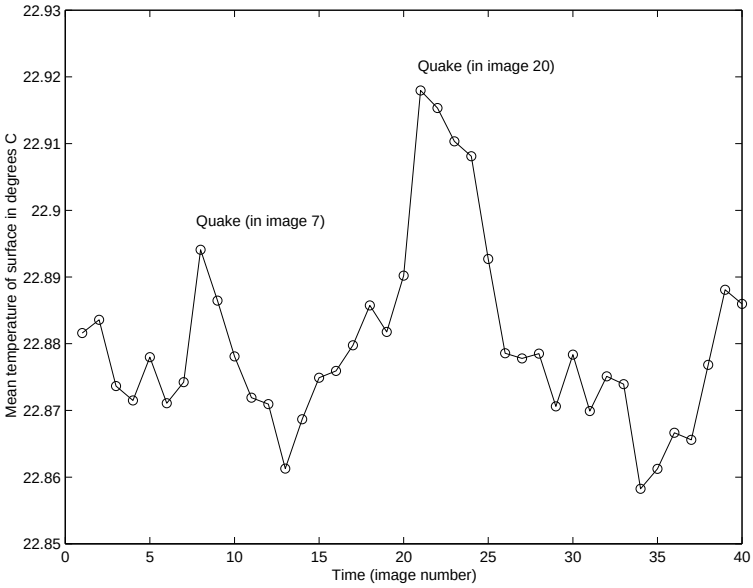

Figure 3.25: Mean temperature in time for the grid region only, in forty images (here numbered 1 through 40) that correspond to images 367 through 407 in the entire set of 1015 images. (N.B. "quake" means the same as "slip" or "event".)

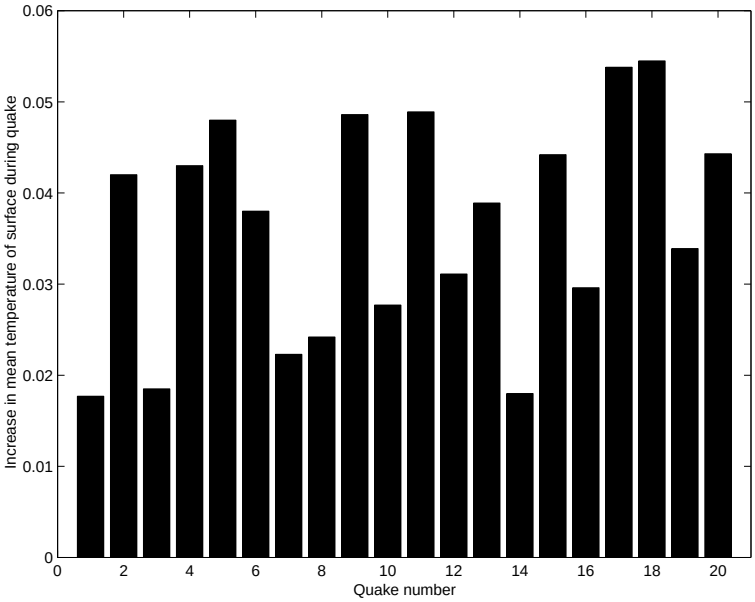

Figure 3.26: Maximum range for the mean temperature of five images centered around each of the twenty labeled events (for the grid region only). (N.B. "quake" means the same as "slip".)

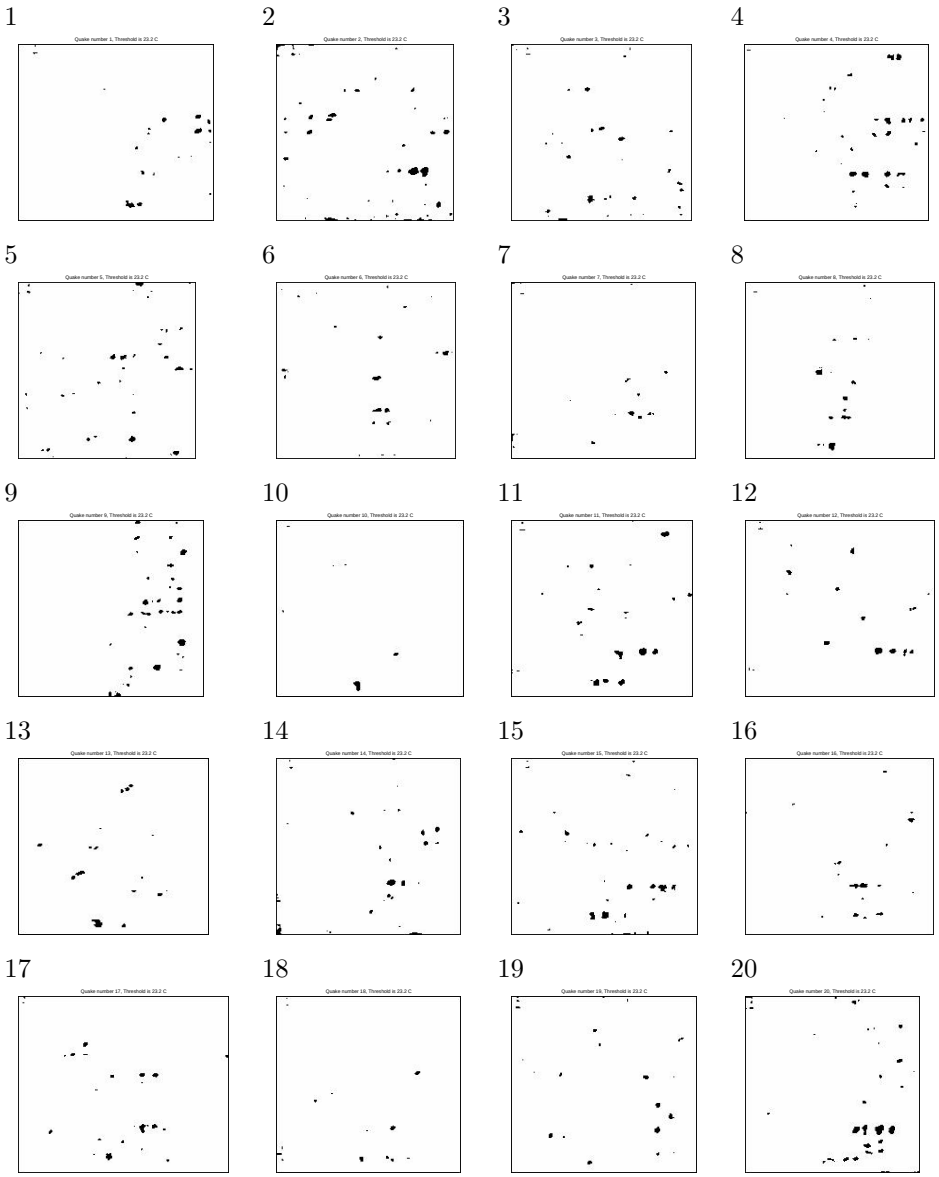

Figure 3.27: Infrared pictures taken after or during each of the twenty numbered events in Figure 3.23, in which all temperatures greater than 23.2 ^{o}C are shown in black.

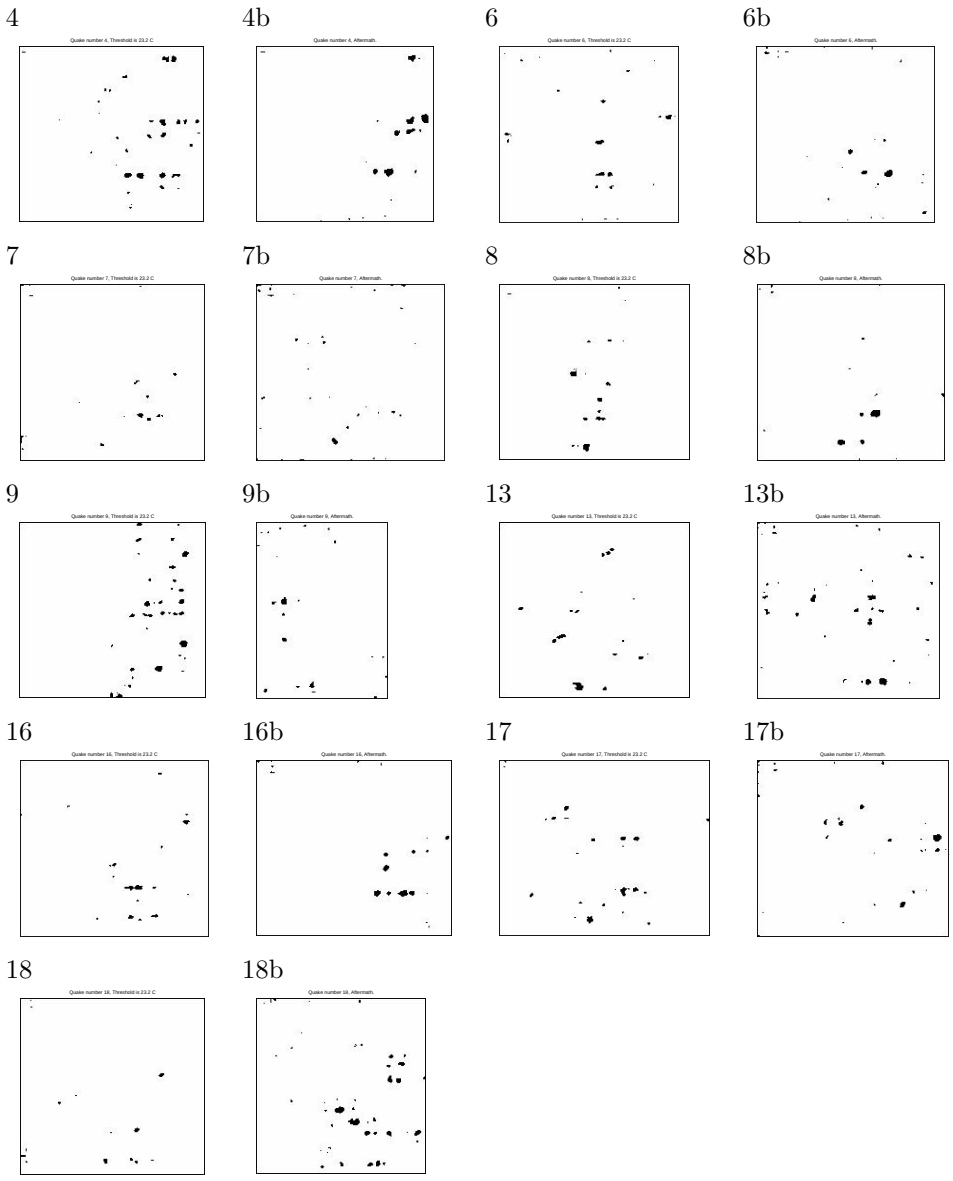

Figure 3.28: Pairs of successive thresholded images of events where the first picture is taken while the frame is in motion, and the second after the motion has stopped. The threshold was chosen large enough so that the grid does not appear in the images (that is, 23.2 ^{o}C).

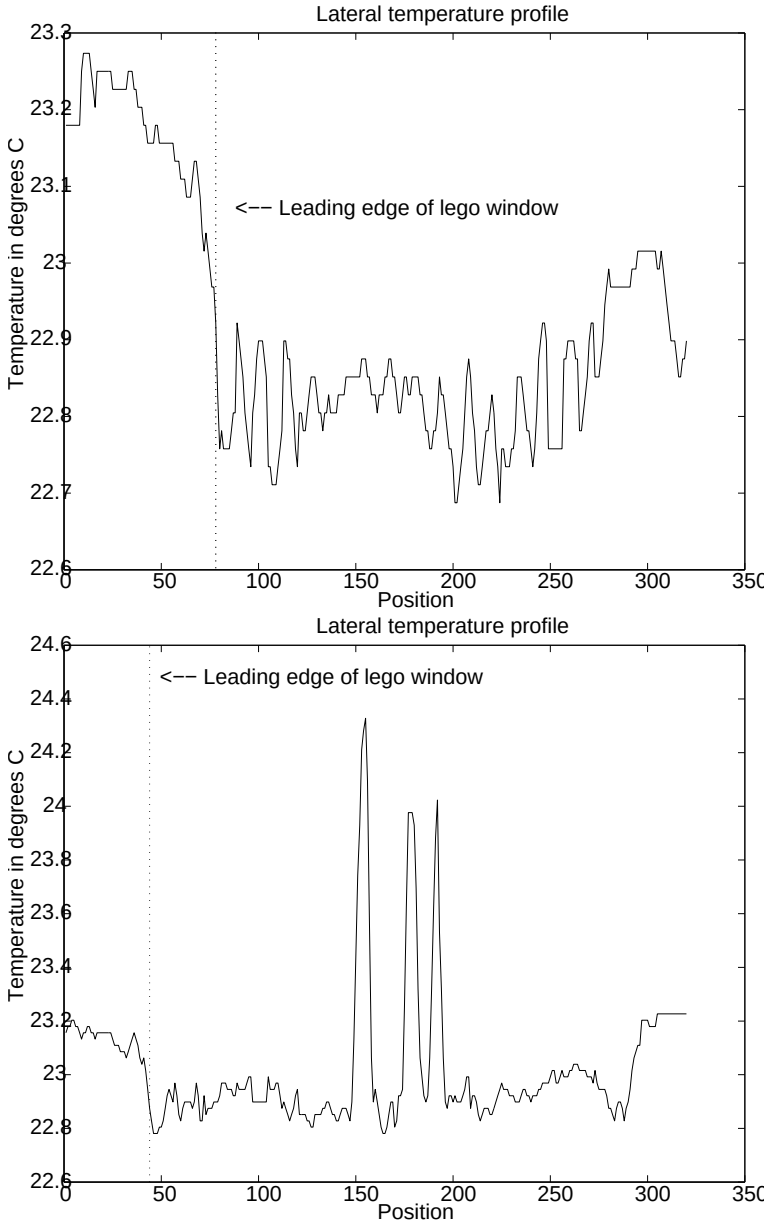

Figure 3.29: Two sample temperature profiles used to find the leading edge of the LEGO frame (called the LEGO "window" in these plots). Note that the profile in the second plot is obtained from an image taken during an event.

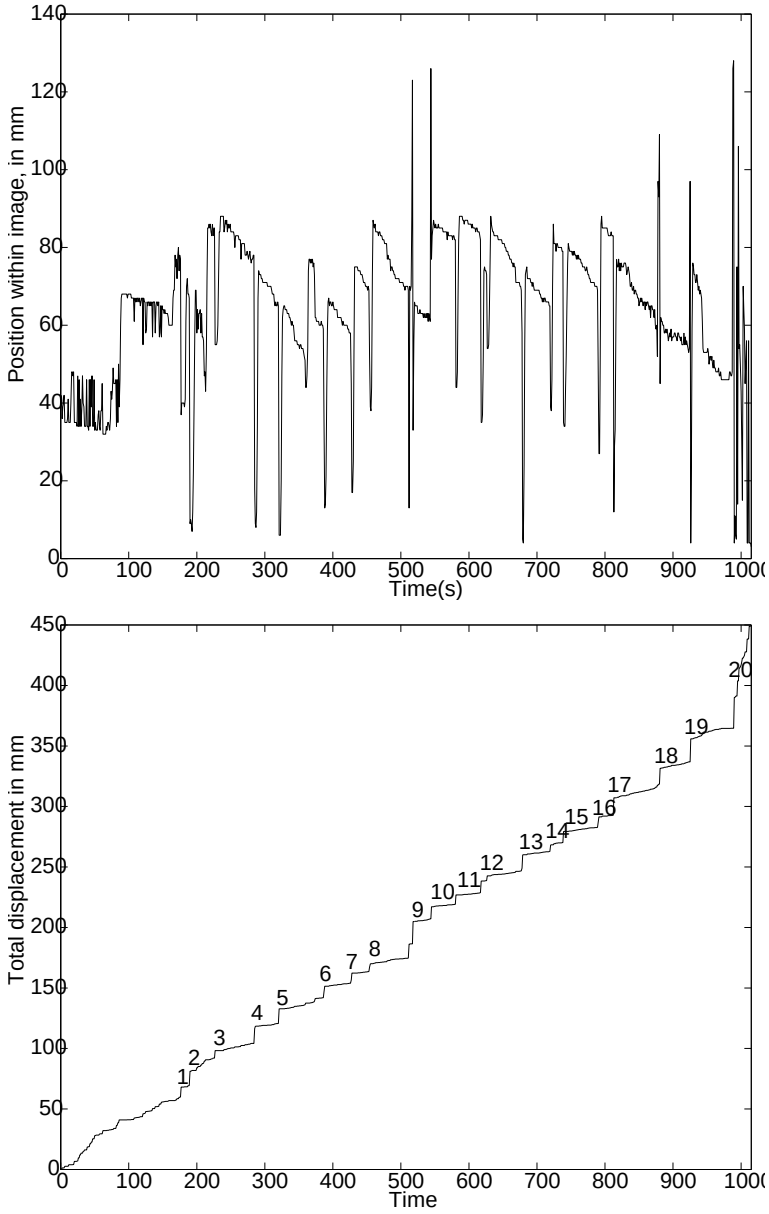

Figure 3.30: The first plot shows the position of the leading edge of the Lego frame, used to support the load in each image, where the time axis is given in terms of image number which is about 6 per second. The second plot shows the total positive displacement of the leading edge in time, also in terms of image number.

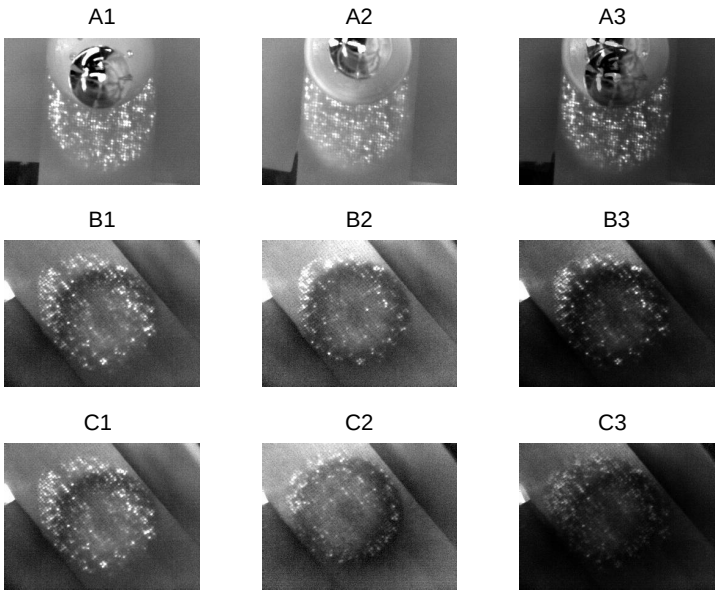

Figure 3.31: Pictures taken immediately after an event. Events are provoked by increasing the force quickly (about 0.25 kg/sec). The slider is removed immediately after the event and a picture is taken with the IR-camera. The first two pictures in each series (A,B,C) show separate events, and are taken in the same position. The rightmost picture in each series shows the product of the two previous images (both are intensity images, where each pixel has a value on a scale from 0 to 1). Using this technique we can find out whether the same fibers make contact each time (for example, overlapping pixels each with large values are reinforced (become brighter), and overlapping pixels each with small values are diminished (become darker)). The A and B series show that some of the asperities are involved each time (light areas in A3 and B3). C1 and C2 are taken at different places on the carpet, to show that the product shows no bright regions (no correlation).

Chapter 4

Analysis of strain gauge measurements

In section 3.1 we described the manner in which event magnitudes are calculated from the strain gauge measurements: if the signal is called $F(t)$, the magnitudes are given by the change in force from any time, t_1, when the force derivative becomes negative ($F'(t_1) < 0$) until some later time, t_2, when this derivative becomes positive again ($F'(t_2) > 0$). The event magnitude, ΔF, is given by $F(t_1) - F(t_2)$. An example of the source code used to calculate these magnitudes is supplied in appendix H (embedded in the source code for a numerical model that describes the triggering and propagation of creep events). In Figure 3.4 an event from the data in Figure 3.3 has been magnified, and an event magnitude and the corresponding event duration time are labeled.

We have also in section 3.2 explained why this method is not totally satisfying, but hard to improve because of large fluctuations in the derivative $F'(t)$. For this reason we have not improved this "naive" method for calculating event magnitudes, accepting that very small magnitude events will not be counted. A more stable motor might in the future allow us to improve the current method. Since excess noise (that is, at the line frequency) will cause the method to count a false event, we have tried to remove this noise.

One way to do this is to use a mean filter on the signal before the events are calculated. The mean filter used was a two point moving average filter.[1] A second way of removing the noise is to assume that the noise will produce the shortest lasting events: that is, those events with a duration time equal or to less than $1/f$, where f is the sampling frequency (about 13 Hz). A third method is to remove all events with magnitude less than the noise level suggested on page 45: that is, those event magnitudes less than $3.5 \times 10^{-7} V$.

Since the main results from the analysis did not depend on the method we

[1] In Matlab this is done by using the convolution command *conv* on the signal S. The filter used was the array A = [1/2 1/2] which is then convoluted with S. The new signal is then Sn = *conv(A,S)*.

used, we have chosen to use the latter method. This is because this method yielded the largest number of events above the noise threshold ($3.5 \times 10^{-7}V$).

In this chapter we will in section 4.1 illustrate with examples from the experiments how we statistically can characterize the data. In section 4.2 we will look further into how the statistics of the system vary with different experiment parameters.

4.1 Statistics of the stick – slip data

We allow time for the system to forget its initial conditions before computing the event magnitudes. That is, we select a time interval in the $F(t)$ signal that corresponds to the period after the slider has been totally displaced from its starting position. By this time the signal has stabilized around some mean value, normally following an initial sharp rise and a correspondingly dramatic drop in strain gauge deflection. Sample data from one of the experiments where the analyzed region is marked with vertical dashed lines, is shown in Figure 3.3. In this section we present data from, in the case of experiment A, 5 consecutive experiments with all parameters kept constant. This has only been done with one configuration, namely the one described on page 33 as experiment A. This corresponds to about 60 000 events that were greater than the noise threshold. When referring to experiment A in other sections, we refer to only one experiment (about 10 000 events) if nothing else is specified.

For each experiment we obtain the probability density function (PDF) $p(x)$, and the cumulative distribution function [2] (CDF) $P(X > x)$ as functions of the event magnitude x.

The PDF is defined in the following way: $p(x)dx$ is the probability that we find the stochastic variable X to have values in the range $[x, x + dx\rangle$

The cumulative distribution bears the following relationship to the PDF:

$$P(X \leq x) = \int_{x_0}^{x} dx' p(x') \ , \tag{4.1}$$

where $p(x)$ is defined for $x' \in [x_0, x]$. For practical reasons we have chosen to define the cumulative distribution as $P(X \geq x)$, that is, the probability for a randomly selected sample, X, to be larger than x. This corresponds to subtracting equation (4.1) from unity, and will not alter the properties of the CDF.

Calculating the cumulative distribution function

The cumulative distribution function (CDF) can be calculated by first sorting all event magnitudes in increasing order, and then for each member x of the

[2]The CDF is actually $P(X < x)$, but the method stems from Pareto [5]. Pareto was interested in the distribution of income. Instead of asking what the r'th largest income is, he asked how many people have an income greater than x. Pareto's law is given in terms of the cumulative distribution function (CDF), i.e. the number of events larger than x is an inverse power of x.

ranked list, counting the number n of event magnitudes that are greater than x. The probability P that a given X is greater than x is $P(X > x) = n/N$, where N is the total number of events in the ordered set.

Calculating the probability density function

There are various ways to estimate the probability density function (PDF) from experimental data. The difference between the methods lies in the manner in which the samples are counted and assigned to the intervals (bins). The method we have chosen to use, is based on logarithmic bin sizes. That is, the ratio of the maximum to the minimum limit of a bin is a constant, a. This will yield a discrete number of bins, n_i. The probability density function can then be calculated like this:

- For all j, the sample x_j belongs to bin n_i, where $i = \text{floor}\left(\frac{log_{10}(x_j)}{log_{10}(a)}\right)$. The Matlab command floor(), rounds down to nearest integer.
- The value of n_i is then equal the number samples that belong to bin i.
- The estimate for the PDF for bin i is $p(x_i) = \frac{n_i}{dxN}$ where N is the total number of samples, and $dx = a^{i+1} - a^i$ is the "width" of the bin.
- The PDF is then given as $(\langle x_i \rangle, p(x_i))$, where $\langle x_i \rangle$ is the average magnitude of the values in bin i.

The error estimate of the value of bin p_i is assumed to be proportional to $\sqrt{n_i}$ where n_i is the number of samples in bin i. In order to justify this assumption we must show that the values in bin i are Poisson distributed. That is, if we divide the data set (experiment) into smaller sets, and then bin the values in each set with logarithmic bins (as described earlier), the distribution of the number of samples in bin i would follow a Poisson distribution. The standard deviation of a Poisson distributed random variable is $\sim \sqrt{\bar{n_i}}$ where $\bar{n_i}$ is the average number of values in bin n_i. We take $\bar{n_i} = n_i$. This justifies our assumption about the uncertainty in $p(x_i)$. However, plotting the standard deviation in bin $p(x_i)$ on a log–log plot is barely visible.

Properties of the event distributions

In Figure 4.1(bottom) we have plotted the probability density of event magnitudes for experiment A in a double logarithmic plot. The figure shows a power law (straight line in a log-log plot) spanning several orders of magnitude in both dimensions.

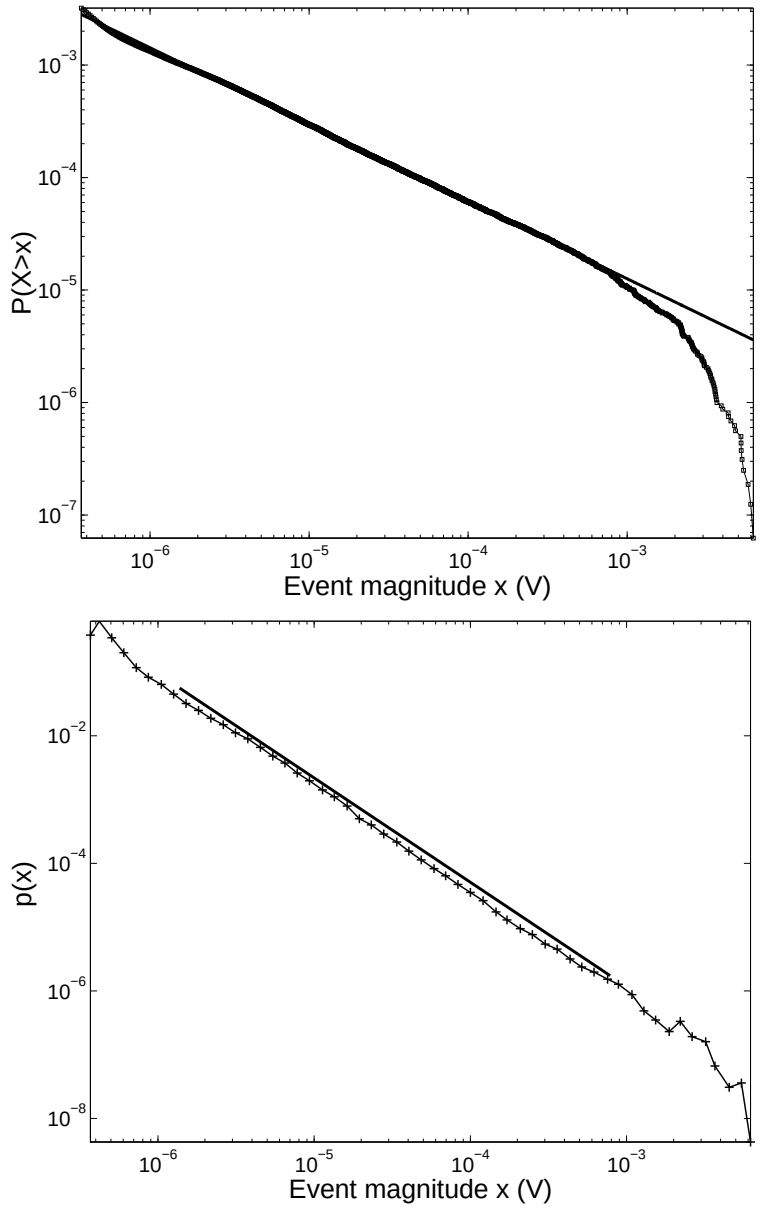

Figure 4.1: (top) The cumulative distribution function (CDF) and (bottom) the probability density function (PDF) are shown for experiment A (stick-creep motion). Each of these exhibits a power law spanning more than 3 orders of magnitude in the x dimension. The exponents have been found by a regression on the interval $[10^{-6}V, 10^{-3}V]$. The exponents found from the regression, $\alpha = 0.68(\pm 0.05)$ (top) and $\beta = 1.66(\pm 0.05)$ (bottom) agree according to the expression $\alpha = \beta - 1$ (equation (4.4)). The PDF is plotted using bin ratio = 1.2 (see page 65). The results in these plots are obtained from 5 identical experiments: that is about 60000 events above the "noise threshold".

That is, we can write the probability $p(x)dx$ that a randomly chosen event magnitude, X, lies in the interval $|x, x + dx\rangle$ according to the law:

$$p(x)dx \sim x^{-\beta}dx. \tag{4.2}$$

The value of β can be found by calculating the slope of the straight line in the double logarithmic plot in Figure 4.1(bottom) ,with the result $1.66(\pm 0.05)$. This is done using a least squares fit procedure in Matlab, over the region $[10^{-6}V, 10^{-3}V]$. The source of uncertainty in the value of β (and other power law exponents) lies mainly in the range that we perform the fit. The exact value of the power law coefficients calculated in this thesis is not of crucial importance, but we estimate the values within an uncertainty of ± 0.05.

Since the cumulative distribution can be obtained by integrating the PDF, as shown by the definition in equation (4.1), the value of β can also be found by inspecting the slope in a plot of the cumulative distribution (Figure 4.1 (top)). If we assume the CDF is also given as a power law, which is natural in the light of equation (4.1), the probability that an event with magnitude X is greater than x is given by

$$P(X > x) \sim x^{-\alpha}. \tag{4.3}$$

We can then write the scaling relation

$$-\alpha = -\beta + 1 \rightarrow \alpha = \beta - 1. \tag{4.4}$$

To illustrate the validity of the power law, we have in Figure 4.2 plotted the scaled $\frac{P(X>x)}{x^{-\alpha}}$ with $\alpha = 0.66$.

The CDF and PDF for an experiment with a different kind of carpet (experiment B), are shown in Figure 4.3. These power laws exhibit exponents that are different from what is found in the case of experiment A, and illustrate that we can obtain power laws with other exponents by changing the type carpet. For experiment A we find $\alpha \sim 0.68 \pm 0.05$ and $\beta \sim 1.66 \pm 0.05$, and for experiment B we find $\alpha \sim 0.45 \pm 0.05$ and $\beta \sim 1.48 \pm 0.05$

As we shall see later, the difference can be ascribed to the fundamentally different kinds of motion that occur in each case. In particular, experiment A was conducted on a surface (Figure 3.8 (a)) which exhibits only stick-creep motion (SCM) in which motion occurs only by means of stretching fibers that are attached to the slider. Experiment B was conducted on a surface (Figure 3.8 (b)) in which a combination of SCM and a second kind of motion occurs, stick-slip motion (SSM). In our definition of stick-slip motion, events are triggered when all fibers lose their grip on the slider, and the slider then slides across the surface until it becomes stuck again.

Finite-size effects and scaling

When properties of a system can be described by a power law [28] (as in equation (4.2)), we expect this power law to be valid only within a limited range of event magnitudes. For critical systems [31], the limits of the valid range are the

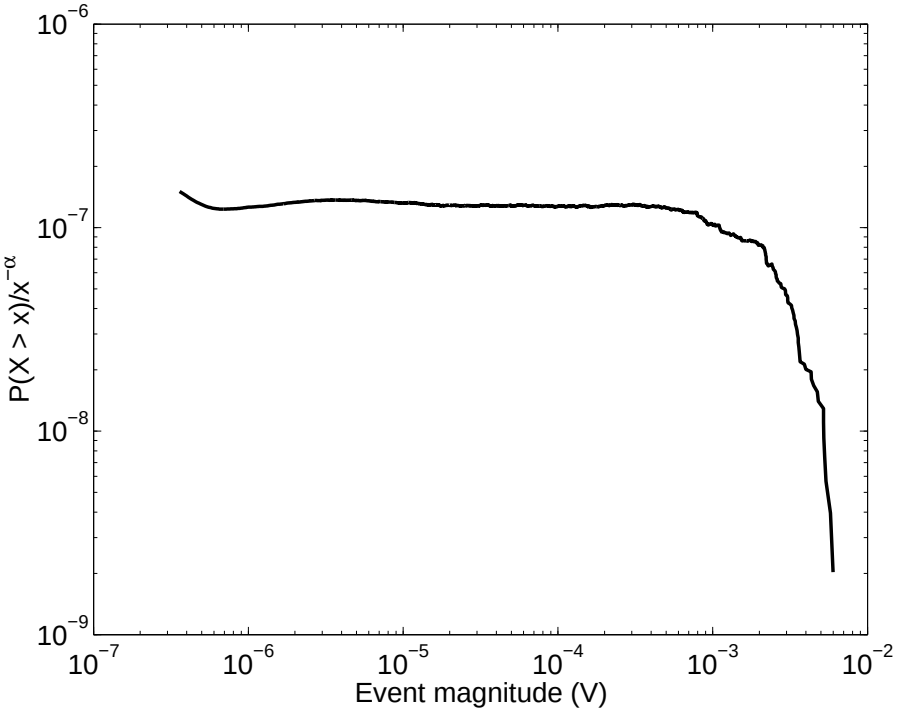

Figure 4.2: A scaled version of the CDF, $\frac{P(X>x)}{x^{-\alpha}}$ with $\alpha = 0.66$, is plotted in order to illustrate the power law.

only scales, and they are set by physical extents of the system. In the carpet-sandpaper system, the low magnitude range is limited by the scale of minimum event that we can measure.[3] The maximum event magnitude is described by a characteristic scale (event magnitude), x^*. Close to this scale the power law should, according to the theory of critical systems and SOC, make a sharp, exponential-like cutoff. The power law shape of the distribution of events (and duration times) defined in equation 4.2, could therefore have the form:

$$p(x) \sim x^{-\beta} e^{-(x/x^*)^a}, \tag{4.5}$$

where a is exponent that describes the "sharpness" of the cutoff. The value of x^* will in our system therefore be expressed through a characteristic event magnitude, or event duration time for which a sharp decay from a power law will take place. That is, if we make a Taylor expansion of equation (4.5) we see

[3]We can not measure events less than 10^{-8}V in magnitude. Due to problems of separating the noise from "real" events, we have chosen to use only those events larger than 3.5×10^{-7}V.

that if

$$x \ll x^* \quad \rightarrow \quad p(x) \sim x^{-\beta} \left(1 - (\frac{x}{x^*})^a + \ldots\right) \tag{4.6}$$

$$x \gg x^* \quad \rightarrow \quad p(x) \sim e^{-(x/x^*)^a}. \tag{4.7}$$

A possible cutoff effect, and cutoff scale can be seen in the Figures 4.1 and 4.3 (bottom) where the power law probability density function makes a sharp bend downwards for the largest event-bin.

The theory of critical systems (and the hypothesis of self-organized critical systems) assumes that all perturbations to the system will be transformed into a change in the length (or time) -scale x^*. For values of x much less than x^* the system will not know the existence of this characteristic scale and behave as if was infinite. On the other hand, close to x^* the system "feel" its prescence and no longer be scale invariant.

We have performed several experiments where we have perturbed the system by changing parameters such as the normal force, the grain size on the sandpaper, and the elastic constants in the pulling string (only one parameter is changed at a time). The effects of these parameter variations should, according to the theory, alter the value of x^* in a systematic way. The probability density of event magnitudes is then a function of two parameters: the event magnitude, x, and the varied parameter L, and it can be represented graphically $p(x)$ as a function of x for a sequence of different values of L. The scaling hypothesis (for critical systems) [31] predicts that all the curves of this family can be collapsed onto a single curve, provided one plots a scaled $p(x)$ ($p(x)$ divided by L to some power) as a function of a scaled x (x divided by L to some different power). In critical systems that are found to obey such a scaling law [38, 7, 22, 28, 25], it is the physical extent of the system (the value of L) that decides the value of x^*. In such systems, where the events, or avalanches, are based on a local propagation of events, such as in spring-block models [7, 25] and in sandpiles models [39, 28], the biggest events will propagate until they reach the perimeter of the system. When these events reach the physical extent of the system, they will terminate. Thus, it is the physical extent of the system that determines the magnitude of the biggest events, and therefore the magnitudes of these events will be underestimated (compared to a bigger system where they would have propagated further). This will lead to an exponential-like (sharp) cutoff, as seen in equation (4.5), for the events that will feel the size of the system.

In the carpet-sandpaper system, we have had problems with observing finite-size effects on the form of equation (4.5).[4] We believe reasons for this could be that the events ("avalanches" of breaking fibers) do not seem to propagate through a local distribution of force or energy, but rather through a global distribution of the force (see chapter 5). If this assumption, of a global distribution of forces in the sandpaper-carpet system is correct, it is not directly

[4]Note that the exponential-like cutoff seen in the cumulative distribution (Figure 4.1), is in the nature of the CDF. This is discussed further in appendix B

the physical extent of the system that determines the magnitude of the biggest event magnitudes, but rather the number of fibers that are gripping. The ability for the system re-grip fibers during the events also limits the maximum event magnitudes. This means that it is a possibility that the biggest events in our experiments are not "falsely" terminated by the physical extent of the system, and that the power law distribution of events can have an abrupt ending, without a crossover to a sharp cutoff. It is likely that if we had a much larger system, the system would start to "feel" the system size and that the local interactions between fibers would start to matter.

Although varying parameters such as the normal force, the sandpaper rating or the surface type might alter the maximum event magnitude (see section 4.2), this does not necessarily lead to a scaling law on the form described in equation (4.5). Instead of the exponential decay of the power law as in equation (4.5), the power law will decay as a step function. The earlier described data collapse of the scaled probability density function, will in cases like this be based on the maximum measured event. Compared to the method of scaling the probabilities using the cutoff effect, this latter method of scaling the distributions is more subjected errors due to statistical effects. In section 4.2 where we report from experiments where we have varied different parameters, we discuss some techniques for reducing this error.

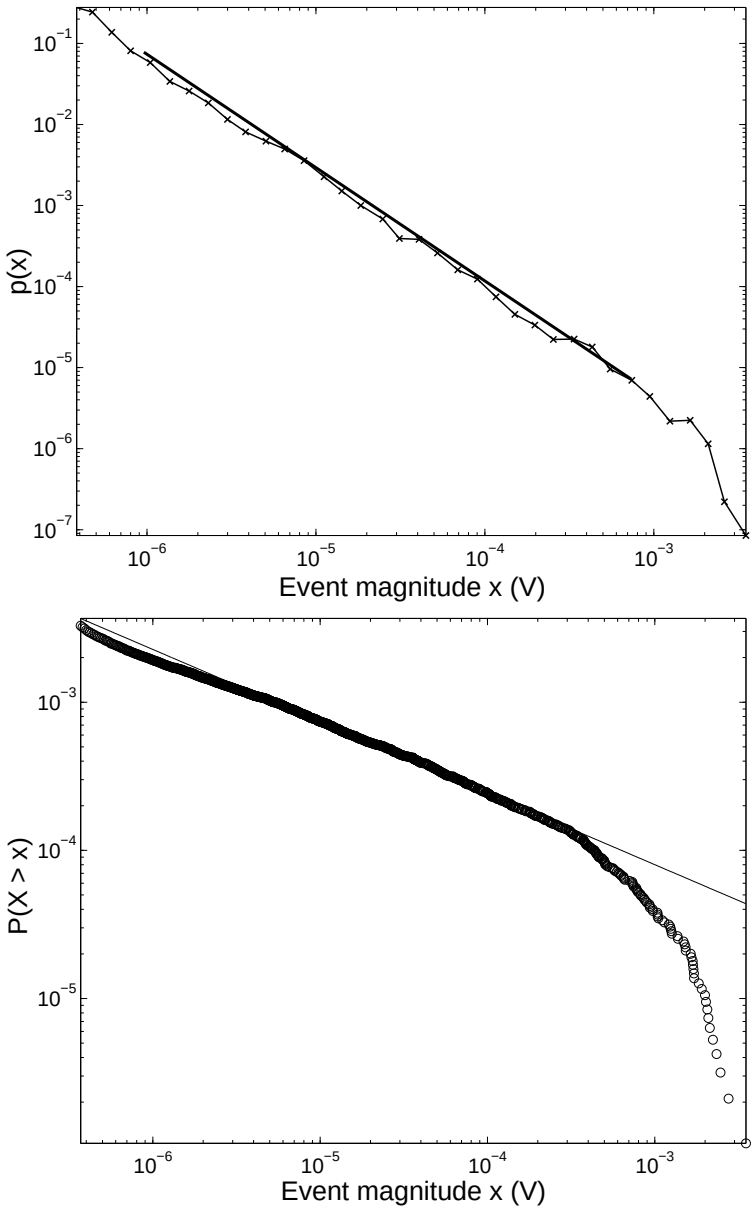

Figure 4.3: (top)The probability density function (PDF) and (bottom) the cumulative distribution function (CDF) of event magnitudes are plotted for experiment B. Each exhibits a power law spanning more than 3 orders of magnitude. The exponents $\alpha = -0.45(\pm 0.05)$ (from the top plot)) and $\beta = 1.48(\pm 0.05)$ (from bottom plot)) are obtained from a linear regression on the interval [1e-6, 1e-3]. The data for these plots are obtained from only one experiment, that is, about 5000 events. Note the difference in β between this experiment and experiment A in Figure 4.1, that is, $\alpha = -0.45$ instead of -0.68 as in experiment A.

CDF versus PDF

Now let us consider the properties of the cumulative distribution (CDF) and probability density function (PDF) and evaluate the relative importance or reliability of each method. The CDF seems at first to have important advantages. By comparison, this function does not fluctuate wildly, which is what happens if we choose bins that are too small for the PDF, and there are no problems regarding how best to choose the limits of the bins. On the other hand, the PDF is more sensitive to finite-size effects. In particular, in the high-magnitude regime the PDF exhibits a downward trend only in the case where a finite-size effect (FSE) is noticed: that is, a transition from power law behavior to exponential decay at the "crossover scale" (see page 69). On the other hand, the CDF departs from power law behavior for three reasons, two of which are non-physical. In addition to a possible finite-size effect, the magnitude at which the CDF departs from power law behavior depends upon the sample size (the number of event magnitudes) as discussed in section B. Moreover, a downward trend in the high-magnitude regime is an expected analytical result, obtained from integrating a PDF that is defined on a finite domain.[5] To see this trend, let us assume we can write the PDF as a power law, as in equation (4.2). Then, the probability that a randomly chosen magnitude X is greater than the magnitude x, is given by the cumulative distribution function (CDF) $P(X > x)$:[6]

$$P(X > x) = \int_x^c p(x')dx' = \frac{1}{c^{-\alpha}}(c^{-\alpha} - x^{-\alpha}), \tag{4.8}$$

where we have selected $x \in [10^{-8}, 10^{-2}]$ as the domain of $p(x)$. From Figure 4.4, we can see that fitting a line on this domain close to the cutoff c will give an inaccurate measurement of the exponent for α. For this reason, a straight line fit to the CDF is less apt to give accurate results for the exponent α as long as the high-magnitude regime is included.

[5] In our experiments this domain is bounded by the magnitude of noise, with mean value of about 3.5×10^{-7} V in the low end, and the maximum event size ($\sim 10^{-2}$V) for the upper bound.

[6] Note that the traditional definition of the cumulative distribution is $P(X < x)$.

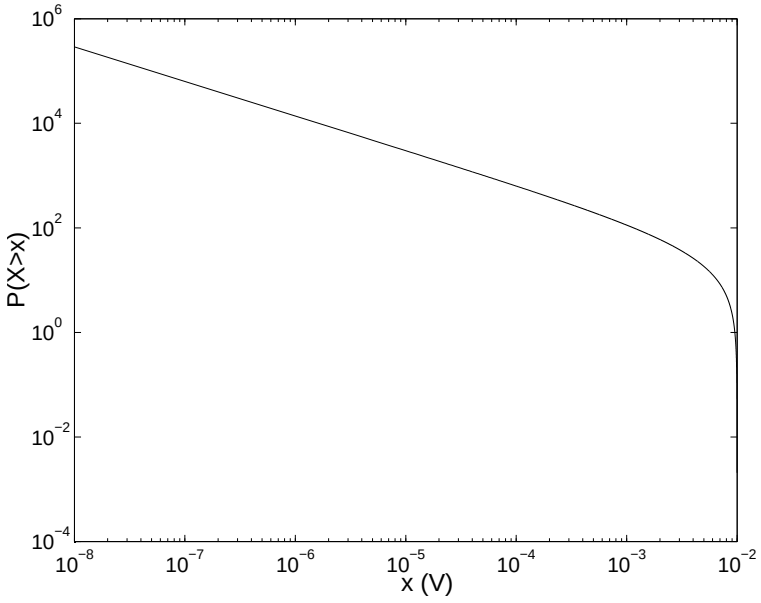

Figure 4.4: A plot of the cumulative distribution function (equation 4.8). Notice how the cumulative probability for high magnitudes goes to 0. The value of α is set to 0.66, which is commonly observed in experiments.

The distribution of event duration times

We have also studied the distribution of event duration times: that is, the time it takes for $F'(t)$ to go from negative to positive again. In Figure 3.4 this corresponds to $t_2 - t_1$. In Figure 4.5 the PDF and the CDF of event duration times for experiment A have been plotted. The plots resemble power laws just like the distribution of the event magnitudes, but now with the new exponent τ (for PDF). This means that we can roughly write the probability of an event lasting time t as follows (see Figure 4.5 top):

$$p(t) \sim t^{-\tau}. \tag{4.9}$$

The cumulative distribution of event duration times, that is, the probability of measuring an event with duration time T greater than t, is given as (see Figure 4.5 bottom)

$$p(T > t) \sim t^{1-\tau}. \tag{4.10}$$

The exponent τ takes a value near to 2 ($\tau = 1.95(\pm 0.05)$) and ($1 - \tau = 0.97(\pm 0.05)$). It should be noted that a power law in the duration time plot only occurs for experiments where the events are relatively long-lasting, often longer than 100 seconds, as happens only in stick-creep motion (that is, experiment

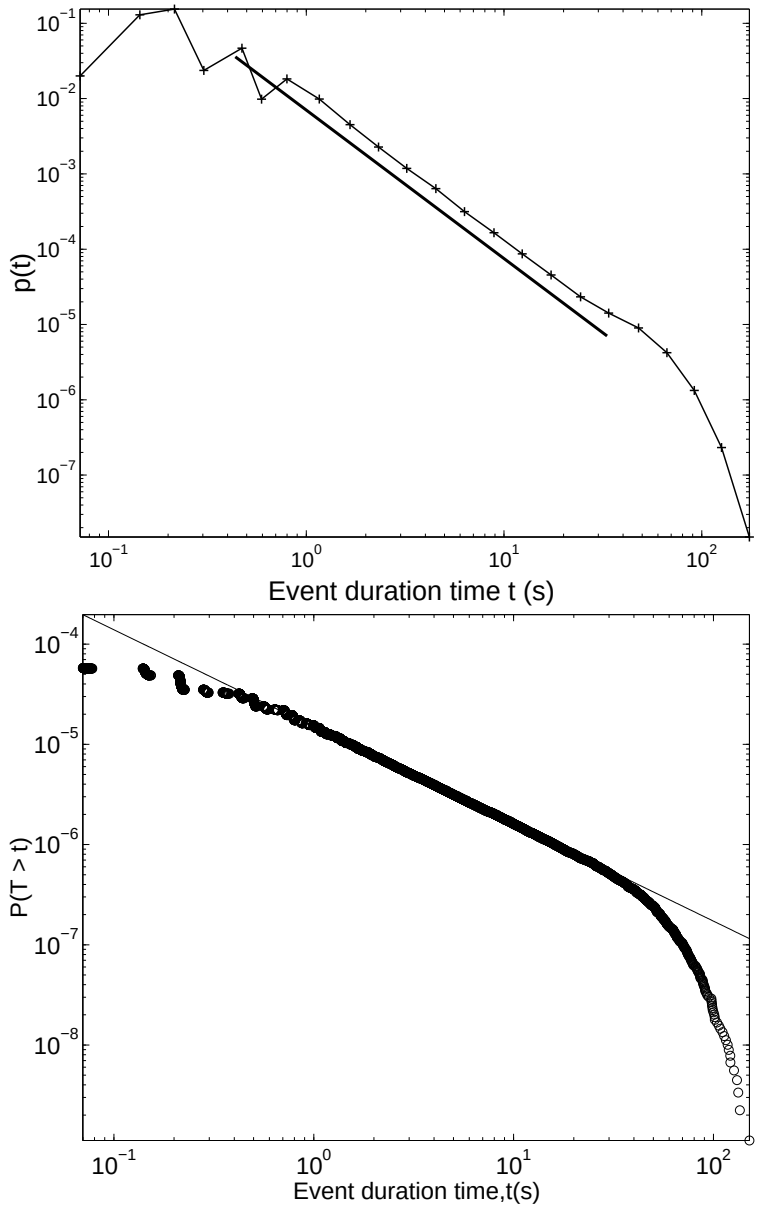

Figure 4.5: The probability density function (top) and cumulative distribution function (bottom) for event duration times in experiment A. The value of $\tau = 1.95(\pm 0.05)$ in equation 4.9, is found from a linear fit (–) in the interval $t \in [5 \times 10^{-1}s, 5 \times 10^{1}s]$. The value of $1 - \tau = 0.97(\pm 0.05)$ (equation (4.10)) in the same interval.

A). In Figure 4.6 we have plotted the event duration time CDF for experiment B, and we see that the shape of the curve is not a well defined power law distribution. Experiment A is the only surface for which we have found a well

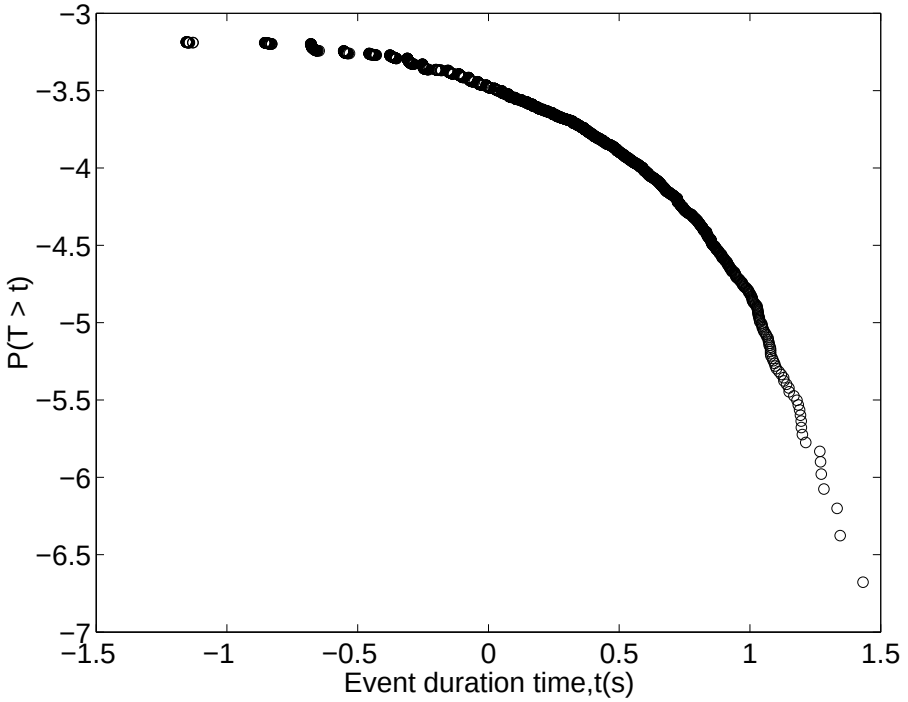

Figure 4.6: The CDF for event duration times for experiment B (more SSM behavior) plotted on logarithmic axes. The round shape of the distribution does not very well correspond to a power law.

defined power law distribution of event duration times. However, we cannot exclude that there is a power law for event duration in stick-slip motion – we may just be unable to resolve the scaling behavior.

The event duration time as a function of event magnitude

Beside from calculating the distributions (4.2) and (4.9), it is instructive to define the joint distribution $p(x,t)$ such that,

$$P(a \leq x \leq b, c \leq t \leq d) = \int_a^b \int_c^d p(x,t)dxdt, \tag{4.11}$$

which in practice means finding a joint histogram in the event duration time (t), and event magnitude (x) space. In Figure 4.7 the event duration times versus the event magnitudes are plotted for experiment A.

The events are first sorted in increasing order, then 20 consecutive events are averaged in both time and event magnitude. The average time, and the average event magnitude for the 20 events is then plotted. From the figure, one may gain insight into the joint probability, as it is proportional to the number of points per unit area in the plane marked with '–'.

One can see from Figure 4.7 that for small event magnitudes ($x < 10^{-6}$V) the corresponding pairs of quantities are not related to each other through a trivial expression. On the other hand, one can see from the figure that each pair of event duration times and magnitudes greater than $\sim 10^{-6}V$ displays a significant linear correlation in the log–log plot. From this fact can we assume validity in the following expression :

$$t \sim x^{\kappa}, \tag{4.12}$$

where κ takes the value of the slope calculated in Figure 4.7. For experiment A the value of κ is close to 0.70. For events in experiment B, the duration times are shorter (more SSM) than in experiment A, and as we saw in Figure 4.6 the distribution of duration times did not follow a power law.

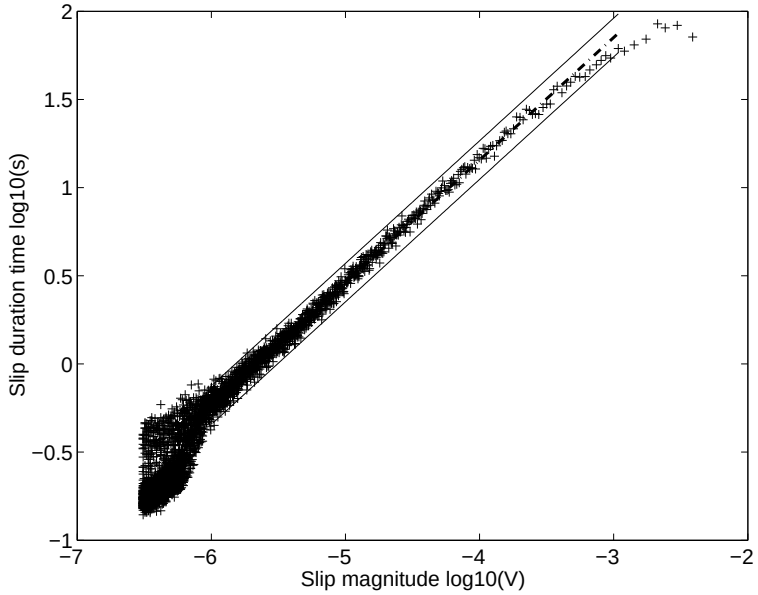

Figure 4.7: The duration time of events as a function of the event magnitudes for experiment A. The event magnitudes are first sorted, then series of 20 consecutive events (sorted) are selected and the mean event magnitude and duration time is plotted. A linear regression to the interval $m \in [10^{-6}V, 10^{-3}V]$ (-.) yields a slope of about 0.70, that is, $\kappa \sim 0.70 \pm 0.05$. The error bounds (corresponding to 99 % confidence) for the first order polynomial is plotted as (–) .

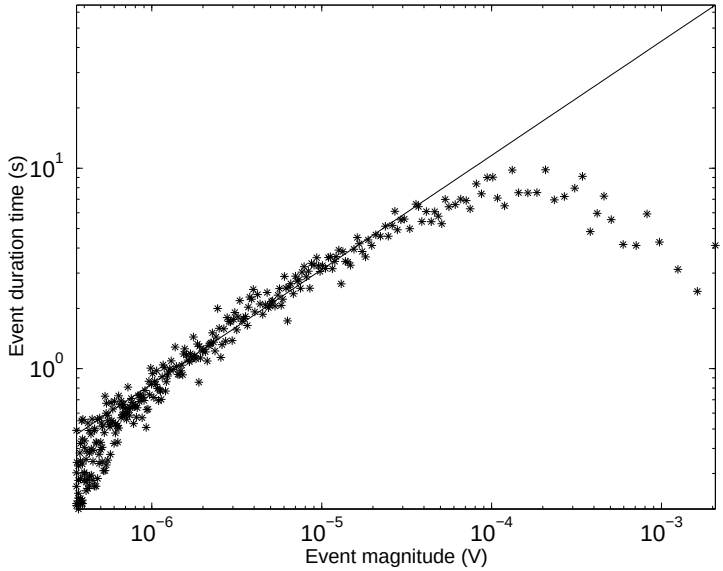

Figure 4.8: The duration time of an event as a function of the event magnitude for experiment B. We observe that for small event magnitudes the shape of the points can resemble a power law (the fit has a slope = 0.55). For larger events, we see that the events tend to decrease in duration time and deviate strongly from the power law. About 3000 data points are used in the plot, and 10 data points are averaged for each point plotted.

Linear correlation coefficient

To test whether the assumption in equation (4.12) is valid, we can check the corresponding linearity in the log-log plot in Figure 4.7. This is done by finding the linear correlation coefficient ν [44]. This method, which can be used on variables that are ordinal, that is, on a discrete but ordered set, goes as follows:[7]

$$\nu = \frac{\sum_i (x_i - \overline{x})(t_i - \overline{t})}{\sqrt{\sum_i (x_i - \overline{x_i})^2}\sqrt{\sum_i (t_i - \overline{t_i})^2}} \,, \tag{4.13}$$

where $\overline{x}$ and $\overline{t}$ are the mean of the event magnitudes x_i and event duration times t_i. The value of ν lies between -1 and 1, where 1 means that there is is "complete positive correlation", and the points $\{x_i, t_i\}$ should lie on a perfect straight line. If ν is equal to -1 the points will lie on a straight line with negative derivative; this is called "complete negative correlation". A value of ν close to

[7] also called the product-moment correlation coefficient, or Pearson's ν. See chapter 14.5 in [44].

0 indicates that the variables (here t and x) are uncorrelated.

The value of ν is found in experiment A found to be ~ 0.8 which strongly supports a linear correlation between t and x in equation (4.12).

The relation between τ, β and κ

We now have the three power law exponents α, β and κ that each can be estimated by experiments, and we want to establish the relationship between them. We assume that the probability of an event with duration in the interval $[t, t+dt]$ is given as $p(t)dt$, and the probability of an event with magnitude in $[x, x+dx]$ is given as $p(x)dx$. The probability of an event in the range $[t, t+dt]$ and $[x, x+dx]$ is given by the joint probability (equation 4.12) $p(x,t)dxdt$. Using equation (4.2) and (4.3) we have:

$$p(t) \simeq t^{-\tau}\,, \tag{4.14}$$

$$p(x) \simeq x^{-\beta}. \tag{4.15}$$

From the power law shape of these equations, we assume validity of the following scaling ansatz for the joint distribution (equation 4.11):

$$p(x,t)dxdt = \lambda^{-\delta} p(\frac{x}{\lambda}, \frac{t}{\lambda^{\kappa}}) d(\frac{x}{\lambda}) d(\frac{t}{\lambda^{\kappa}})\,, \tag{4.16}$$

where δ is a new scaling exponent. We then integrate equation (4.16) with respect to t:

$$\begin{aligned} p(x)dx &= \lambda^{-\delta} d(\frac{x}{\lambda}) \int_0^{\infty} d(\frac{t}{\lambda^{\kappa}}) p(\frac{x}{\lambda}, \frac{t}{\lambda^{\kappa}}) \\ &\underset{\lambda=x}{=} x^{-(\delta+1)} dx \int_0^{\infty} du\; p(1,u)\,, \quad \text{where } u = \frac{t}{\lambda^{\kappa}} \\ &\sim x^{-(\delta+1)} \sim x^{-\beta}\,, \end{aligned} \tag{4.17}$$

where we have used equation (4.15) in (4.17). It then follows that

$$\delta + 1 = \beta. \tag{4.18}$$

Next we integrate equation (4.16) with respect to x:

$$\begin{aligned} p(t)dt &= \lambda^{-\delta} d(\frac{t}{\lambda^{\kappa}}) \int_0^{\infty} d(\frac{x}{\lambda}) p(\frac{x}{\lambda}, \frac{t}{\lambda^{\kappa}}) \\ &\underset{\lambda=t^{1/\kappa}}{=} t^{-\frac{\delta+\kappa}{\kappa}} dt \int_0^{\infty} du\; p(u,1)\,, \quad \text{where } u = \frac{x}{\lambda} \\ &\sim t^{-\frac{\delta+\kappa}{\kappa}} \sim t^{-\tau}\,, \end{aligned} \tag{4.19}$$

where we have used equation (4.14) in (4.19). We can then write $\tau = (\kappa+\delta)/\kappa$. This means we have the following expression for the exponents

$$\tau = \frac{\beta + \kappa - 1}{\kappa}. \tag{4.20}$$

Until now we have assumed that κ is just a scaling parameter for the joint distribution (equation 4.16) and we argue that κ is the exponent we extracted from Figure 4.7, the plot of the event duration as a function of event magnitude (equation (4.12)). In the $p(x,t)$-space, the maximum (largest) probabilities will trace out a sharp "ridge", where the $t(x)$-curve (equation 4.12) will consist of the points on this edge. Consider the plot "designed" in Figure 4.9: the solid line in the figure represents the solid line fitted in Figure 4.7, while the points (marked with '*') represent the scattered points obtained from experiments. We locate a local maximum at $p(x_0, t_0)$ (inside the triangle somewhere). According

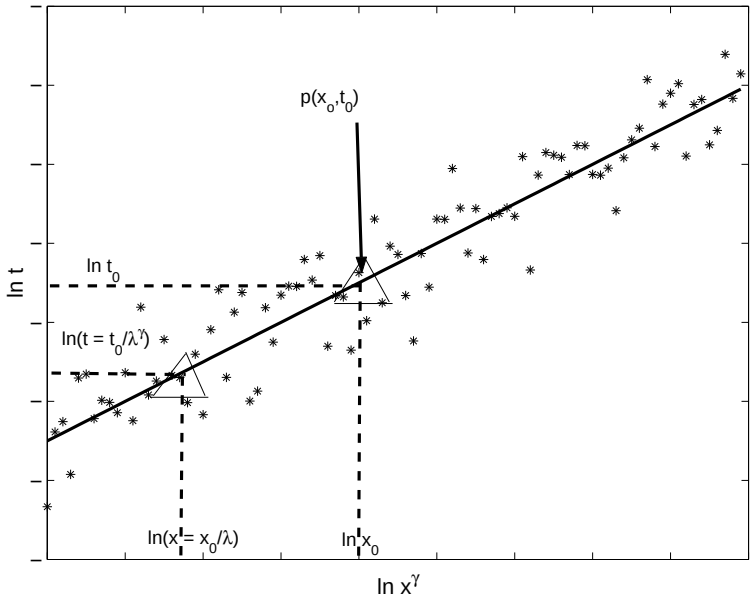

Figure 4.9: A "designed" plot in order to illustrate the interpretation of the exponent κ.

to equation (4.16) we have :

$$\lambda^{\delta+1+\kappa} p(x_0, t_0) = p(\frac{x_0}{\lambda}, \frac{t_o}{\lambda^\kappa}). \tag{4.21}$$

If we let $x_0 \to \frac{x_0}{\lambda}$ and $t_0 \to \frac{t_0}{\lambda^\kappa}$, we move to the other maximum probability in Figure 4.9. That is, we let $x = \frac{x_0}{\lambda} \to \lambda = \frac{x_0}{x}$, which means that we let $t = \frac{t_0}{\lambda^\kappa} = t_0(\frac{x}{x_0})^\kappa$, which again is the relation we suggested in equation 4.12. Thus, the κ we use in as scaling parameter in equation (4.16) is equal to the κ we measure in Figure 4.7.

In order to test whether equation (4.20) is satisfied in the experiments, we fill in the approximate obtained values for $\beta \sim 1.7$, $\kappa \sim 0.7$ and $\tau \sim 2$ for

experiment A. From equation 4.20, $\tau = \frac{\beta+\kappa-1}{\kappa} = (1.7+0.7-1)/0.7 = 2$, which is approximately the value we have measured for τ in Figure 4.7.

Time between events

Are the events statistically independent? We assume that the probability of measuring an event magnitude in the range $[M, M+\Delta M]$ is given as $P_M = p(M)\Delta M$, where $p(M)$ is the event probability density. It is then possible to calculate the average time (or number of events) between two events in this range. In order to simplify the problem, we regard the events in time as a stochastic process where we have a well defined average time between events, $\dot{n}$.[8] Given that an event in this range has just occurred, we may ask: how many events will occur before we measure another event with a similar magnitude (that is, in the range $[M, M+\Delta M]$)? The average time between events, $\dot{n}\langle T(M)\rangle$, can then be found by calculating the following sum :

$$\langle \dot{n} T(M)\rangle = \dot{n} \sum_{n=1}^{\infty} n P_n \ , \tag{4.22}$$

where P_n is the probability that the next event in the range $[M, M+\Delta M]$, occurs after n events. For example, in order to calculate $P_{n=3}$, we must have 2 events that are not in the range, followed by 1 event that is within the range. If the events are statistically independent, we can write this probability as $P_3 = (1-P_M)^2 P_M$. We therefore write the sum in equation (4.22) as follows :

$$\begin{aligned} \langle T(M)\rangle &= P_M + 2P_M(1-P_M) + 3P_M(1-P_M)^2 \ldots \\ &= P_M \sum_{n=0}^{\infty} (n+1)(1-P_M)^n \ . \end{aligned} \tag{4.23}$$

For convenience we write $x = 1 - P_M$, and continue equation (4.23):

$$\begin{aligned} \langle T(M)\rangle &= (1-x)\left[\sum_{n=0}^{\infty} n x^n + \sum_{n=0}^{\infty} x^n\right] \\ &= (1-x)\left[x\frac{\partial}{\partial x}\frac{1}{1-x} + \frac{1}{1-x}\right] \\ &= \frac{x}{1-x} + 1 = \frac{1}{1-x} = \frac{1}{P_M} \ , \end{aligned} \tag{4.24}$$

where we have used that the geometric sum

$$\sum_{n=0}^{\infty} x^n = \frac{1}{1-x} \ . \tag{4.25}$$

[8] The number of seconds per event (that are above the noise threshold) was fairly constant, and close to 6 seconds for experiment A.

By estimating $\Delta M \sim M$, and $p(M) \sim M^{-\beta}$ (from equation (4.2)) we find that:

$$\langle T(M) \rangle = \frac{1}{P_M} = \frac{1}{p(M)\Delta M} \sim M^{\beta-1}. \tag{4.26}$$

In Figure 4.10 we have plotted the average time between events as a function of event magnitude, M, for experiment A. The magnitude range, ΔM, is chosen so that $M_{\max}/M_{\min} = 1.2$ (that is, $\Delta M \sim M$) within each bin. With a linear regression to the linear trend in the plot, we obtain a slope of 0.66 ± 0.05 which is what we should expect when we combine the results obtained for β in Figure 4.1 and equation (4.26). That is, according to equation (4.26), $\beta - 1 \sim 1.66 - 1 = 0.66$, which is what we find in Figure 4.10. We conclude that the time between

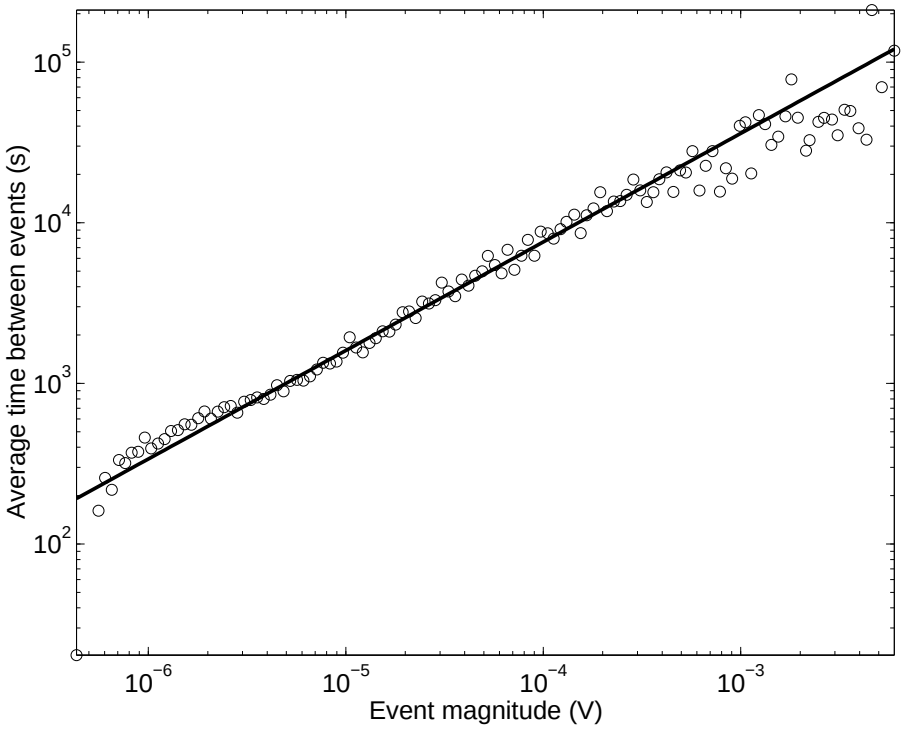

Figure 4.10: The mean time between events $\langle \dot{n} T(M) \rangle$ within a given event magnitude interval (o). The magnitude intervals are calculated by choosing $M_{\max}/M_{\min} = 1.2$ for each bin. A linear regression to the plot yields an exponent of 0.66 ± 0.05 which is as expected according to equation (4.26) and the value for β in Figure 4.1

events is consistent with the events being statistically independent.

Overview of power law exponents

A short overview of the different exponents, where they are available, for experiment A and B is presented in table 4.1. The value of κ for Experiment B is a based on a very "short" power law (Figure 4.8), and its validity might be questioned. The values of κ are checked with the basis of the relation in equation (4.20).

Table 4.1: Values and description of the various exponents for experiment A and experiment B (the difference of the two is explained on page 33). Uncertainties in the exponents are estimated to ± 0.05. The exponents in the column label "Rain" are obtained from [45], where event magnitudes correspond to mm of rain, and the duration time is the lasting (in minutes) of the rain event. The rain data is collected, through 6 months, on the Baltic coast in Zingst (Germany) using a Micro Rain Radar. The value of κ is calculated from (equation (4.20)) $\kappa = \frac{\beta-1}{\tau-1}$, and confirmed through re-plotting of the data used in [45]. The values κ in the other columns are also confirmed through this relation.

Exponent	Exp. A	Exp. B	Rain	Explanation	Equation
β	1.66	1.48	1.4	PDF for magnitudes	4.2
α	0.68	0.45		CDF of magnitudes	4.3
τ	1.95	1.9 (?)	1.6	PDF for duration times	4.9
κ	0.7	0.55 (?)	1.2	joint probability	4.12

4.2 Other experimental results

With the statistical tools described in the last section, we have obtained and analyzed event magnitudes data from over 100 experiments. We have varied parameters such as normal force, sandpaper coarseness, string thickness, type of surface (carpet), and driving speed. We will in this section summarize some of the observational trends from these experiments, and along the way propose what are the future prospects of other experiments of this type.

Two types of motion at low sliding velocities

As mentioned before, the motion of the slider on different surfaces (carpets) can be classified using two categories. One of these is stick-slip motion (SSM), in which occasionally all attached fibers are released and the slider is allowed to glide rapidly over the surface until a critical number of fibers has gripped again or else microscopic friction halts the motion. The second kind of motion is called stick-creep (SCM), which occurs whenever a single fiber lets go while the others remain attached. In this case the slider moves slowly by increasing the strain on fibers that remain attached. Most carpet surfaces exhibit a combination of SCM

and SSM, as in experiment B, whereas some exhibit only SCM, as in experiment A (compare Figure 4.1 and 4.3).

Carpets that are dominated by a combination of stick-slip and stick-creep motion exhibit a value of α (equation 4.3) in the range from -0.5 to -0.35, whereas carpets in which only stick-creep occurs normally produce values of α from -0.6 to -0.75. In some cases it may happen that a surface is worn so thoroughly that stick- slip motion emerges where previously there was only stick-creep motion. An example of this can be seen in figure 4.11 where the distribution exponent of events goes from being SCM to SSM. The longest lasting event for the unworn carpet is about 80 seconds, while the longest event for the worn is about 20 seconds. The value of α is higly reproducible for one type of carpet, but the

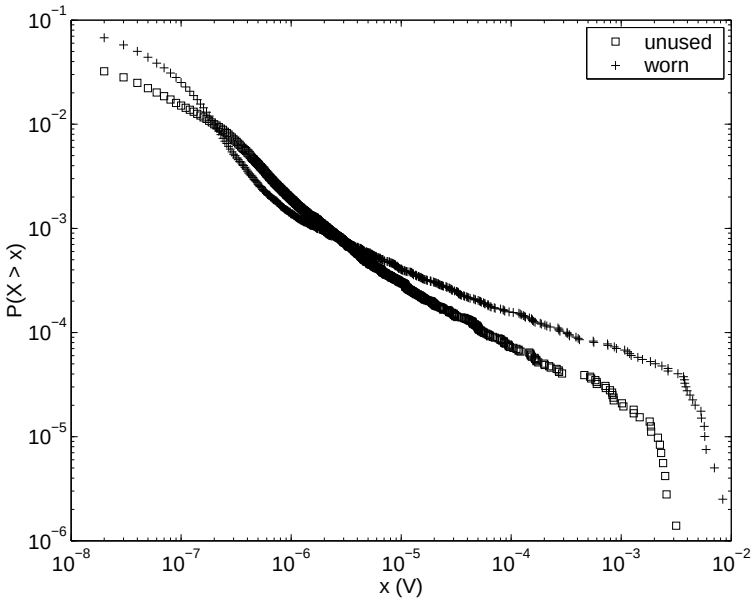

Figure 4.11: Cumulative distributions of event magnitudes for two experiments where the same carpet has been used twice. The distribution of the unused carpet is marked with squares and the used carpet is marked with '+'. A quantitative difference in the distribution can be seen as a result of wear. If we assume the distributions are given as a power law in the high magnitude regime, they have exponents $\alpha \sim 0.4$ for the worn (+), and $\alpha \sim 0.6$ for the unworn carpet (squares).

carpet must not be worn in order to achieve this.

Inhomogeneities in the stick-slip data

If we plot the event magnitudes versus the event number (see figure 4.12(top)) we see that there are periods in the experiment where the density of events are much lower than other places. Take for example the dense region in the top plot, form event number 0 to about 2000. This corresponds, in the bottom plot, to the region $1 - 1.3 \times 10^5$s. That is, the number of events per second in the first cluster (0-2000 events) is about 3 times as low as in the rest of the experiment. The clustering observed in Figure 4.12(top) is often observed in our experiments, and does not always occur at the beginning: at times the clusters appear at the midpoint or near the end of the experiment. However, whether these clusters of lower density of small events are present or not, does not affect the overall properties of the distributions.

We have undertaken several adjustments to the experiments to find out the reasons for this clustering. We have tried to fasten the carpet to the board using double sided tape (this became the standard way), putting pipettes between the solid board and the moving board (now also the standard) and assuring there are no disturbances such as temperature differences, air current or other such factors. We have diminished somewhat the clustering effect, but not fully. We believe the difference in large-magnitude event density (number of big events / number of small events) is guessed to be caused by either:

- changing gripping conditions in different regions of the carpet surface: for example, the number of asperities that can become attached to the slider in a given region (this depends on the local topography of fibers). We have tried to ensure that conditions are homogeneous and constant throughout the experiment, and for this reason we believe that the clustering may arise because of local inhomogeneities in the carpet itself.

- the actual noise, either from the motor, electronic sources or other mechanical/thermodynamic sources is not constant throughout the experiment.

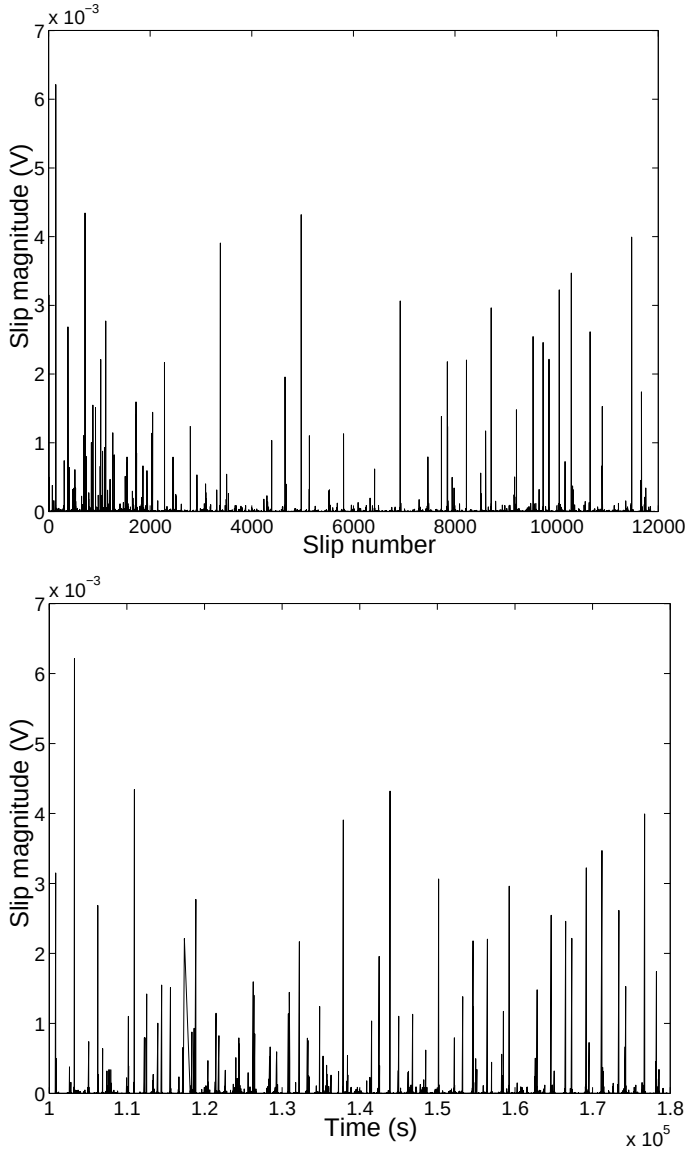

Figure 4.12: (top) Plot of event magnitude versus event number. This plot shows clustering of events at the beginning of this experiment, a feature that is not visible in (bottom), a plot of event magnitudes in time. In the clustered regions there are relatively few small events between larger events. After about 2000 events (top) we see that the number of small events increases and that big events therefore are farther apart. In the bottom plot this corresponds to the region $1 - 1.3 \times 10^5$s. The number of events per second is 0.3 in the first region (lasting 0-2000 seconds), and 0.8 events per second afterwards.

The effect of varying the normal force

From the classical friction laws one expect that the friction force should increase with the normal force, but it is not clear how this will affect the distribution of event magnitudes. We have carried out several experiments where the only parameter varied has been the normal force.

For both experiment A (Figure 4.14) and of experiment B (Figure 4.13), the exponent of the power law distribution of event magnitudes seems to be fairly unaffected by a change in the normal force, although the mean force required to pull the slider increases with the normal force. The number of small magnitude events also increases with the normal force. This can be observed in Figure 4.14 where a "hump" in the low magnitude regime becomes more prominent for higher normal forces. From the discussion regarding finite-size effects on page

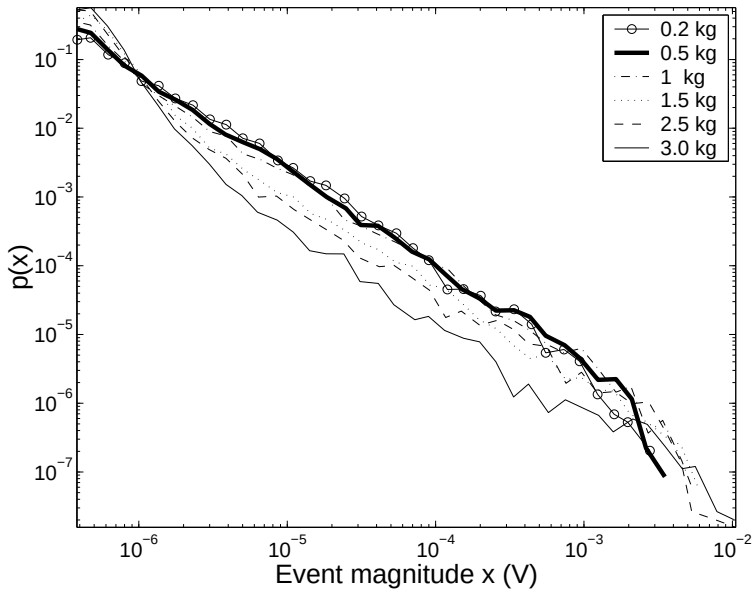

Figure 4.13: Probability densities of event magnitudes (x) for different normal forces. These results were obtained from experiment B. The value of β lies between 1.33 and 1.40, and there does not seem to be a systematic trend in these values. The maximum event magnitude seems to increases with the normal force. See plot 4.15 for more details about this trend.

68, we learned that all perturbations of the system (such as a variation of the normal force) should result in a change of a characteristic event scale, a^*. It is therefore interesting to learn how and if this scale is altered when the normal force is changed in our experiments. Thus, the event scale, a^*, can be "mapped" to a characteristic length scale, L, of the system. For systems of finite size, the shape (or dynamical range) of the event distribution will depend on L, as well

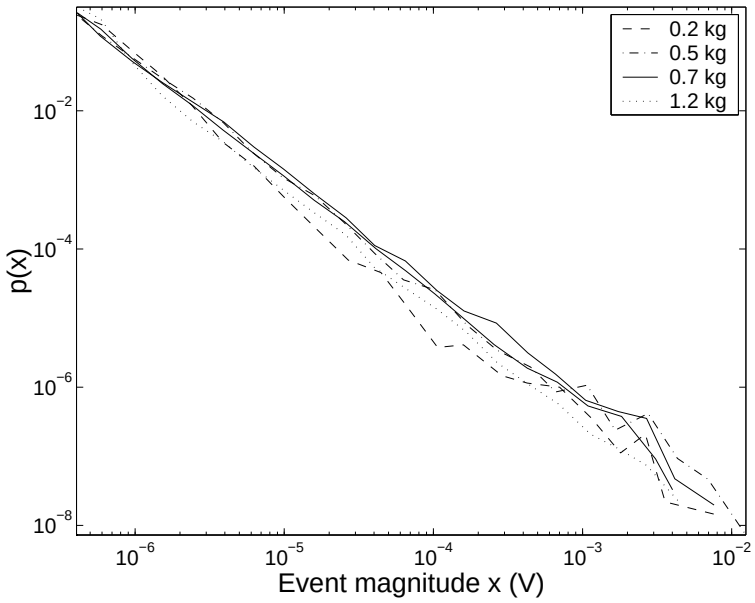

Figure 4.14: Probability densities of event magnitudes (x) for different normal forces for experiment A (only stick-creep motion). The values of β lie between 1.60 and 1.70, and there does not seem to be a clear trend in these values. There does not seem to be a correlation between the maximum event magnitude and the normal force, but from Figure 4.16 we see that the maximum event magnitude decreases with the normal force.

as the event magnitude x. The scaling hypothesis states that, if the probability density of events is a power law, it can be written as: [9]

$$p(x, L) \sim L^{-\phi} G(\frac{x}{L^{\zeta}}) \ , \tag{4.27}$$

where G is a suitable scaling function, and ϕ and ζ are critical exponents describing the scaling of the distribution function. There could as well be other length scales than L, but it is believed that the effects of these will be averaged out by the system [47].

A variation in, for example the normal force should "transform" into a change in L. According to this scaling assumption, the probability density of event magnitudes for different values of L can be expressed in terms of the scaling form in equation (4.27). If this equation provides a valid description of the geometric scaling properties, then plots of $L^{\phi} p(x, L)$ against x/L^{ζ} for different values of normal forces will fall on a common curve (data collapse), $G(y)$. However, in order to be able to do this data collapse and find the value of ϕ and ζ, we believe

[9] we're assuming that $p(x, L)$ then is a homogeneous function [46]

we need far more data points to obtain a well defined crossover at the cutoff scale in the probability density function. It might also be that the system is too small for any length scale to be prominent. In Figure 4.1 (bottom), where we have used 5 times more data points than in any other event magnitude probability density plot, the crossover scale is still not well defined. On page 69 we discussed the possibility that the finite-size (or finite number of contacts) effects are not visible as a crossover to an exponential decay in the power law. Instead we proposed that the scaling of the system could be found by inspecting the maximum event magnitudes of the experiments. We have therefore looked at the maximum event magnitude as a function of the normal force. Because the dynamical range of the varied normal force is only one order of magnitude, we have not tried to get an estimate for ϕ and ζ, but we have rather got a "glimpse" of how and whether there is characteristic scale in the system and if this is affected by this perturbation.

In Figure 4.13 we see that the maximum event size for experiment B increases with the normal force, while for experiment A (see Figure 4.14) there is no obvious trend (however, in Figure 4.16 there is a trend). In Figure 4.15 we have plotted the maximum event size as a function of normal force for experiment B. We see that the maximum event size increases with the normal force. When the same plot is performed for experiment A (see Figure 4.16), we observe that the maximum event magnitude decreases with increasing normal force. That

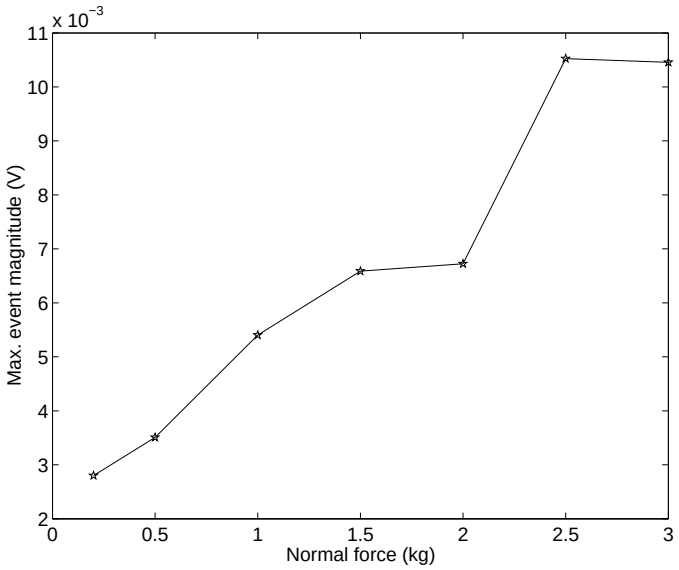

Figure 4.15: The maximum event magnitude as a function of the normal force for experiment B. We see that the maximum event magnitude increases with the normal force (with a few exceptions).

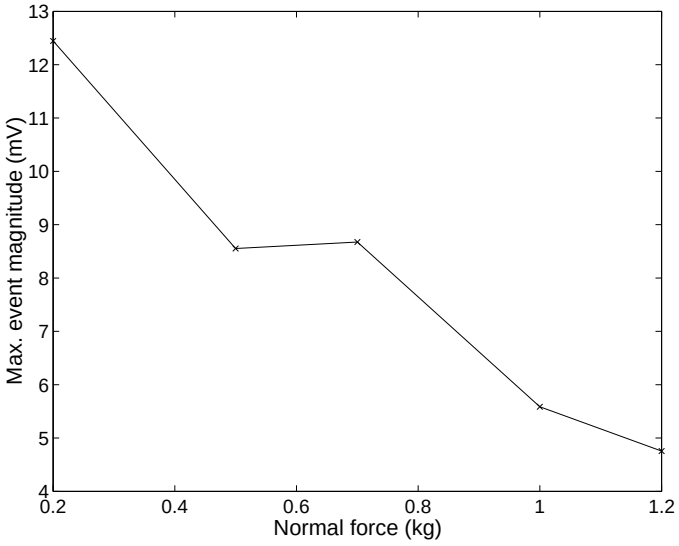

Figure 4.16: The maximum event magnitude as a function of the normal force for experiment A. We see that the maximum event magnitude decreases with the normal force.

is, changing the normal has the opposite effect in experiment A and B. This interesting result may originate from the fact that experiment A is pure stick-creep motion (that is, events with long duration times), while experiment B is basically stick-slip motion (that is, short event duration times). Once a creep event is initiated (experiment A), the probability for fibers to re-grip, or for new fibers to make contact (causing the slider to halt) may increase with the normal force. For slip events (experiment B), the low density of gripping fibers may cause the varying normal force to have a less dominant halting effect. Increasing the normal force should rather result in that a greater number of fibers actually hook on to the slider before the events and therefore causing greater event magnitudes. This is not an explanation of the observed effect, but mere a suggested factor that can cause this effect, namely the type of surface that is used. It would therefore be interesting to perform the same experiments with other types of surfaces (such as paper, silicon, metals etc.) to test whether the different observed trends in Figures 4.15 and 4.16 are not just special for "friction" in the carpet experiment.

In Figure 4.15 and 4.16 we selected the largest event magnitude from each experiment. To test whether the observed trend in these figures is just a co-incidence, or just an effect of how many event there were in the experiment, we divided each experiment into shorter segments and then found the average maximum event magnitude in these segments. In Figure 4.17 we have plotted the average maximum event magnitude in segments of duration 0.5 hours (left)

and 8 hours (right), as a function of normal force. From these figures we see that the trend observed in Figure 4.15 is preserved irrespective of the length of the segment, and that the average maximum event magnitude increases with the length of the segment. In Figure 4.18 we have plotted the average maximum

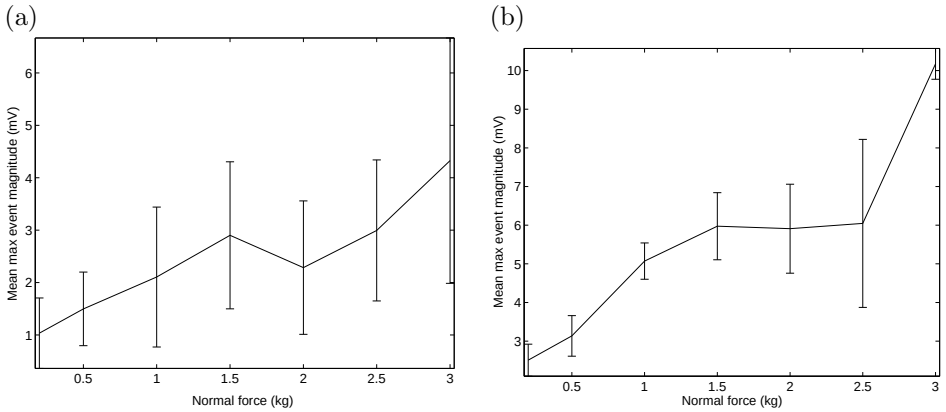

Figure 4.17: The mean maximum event magnitude within segments of duration 0.5 hours (a) and 8 hours (b), as a function of the normal force (for experiment B). We see that the trend seen in Figure 4.15 is preserved for both lengths of the segments. The vertical bars represents the standard deviation of the maximum event magnitudes.

event magnitude as a function of the length of the segment, for three different normal forces. We see that for segment longer than about 4 hours, the average maximum event magnitude levels of. It is possible that we could fit a $\tanh t/t^*$ function to the data, and from that estimate a characteristic time, t^*, of the system. However, this has not been explored.

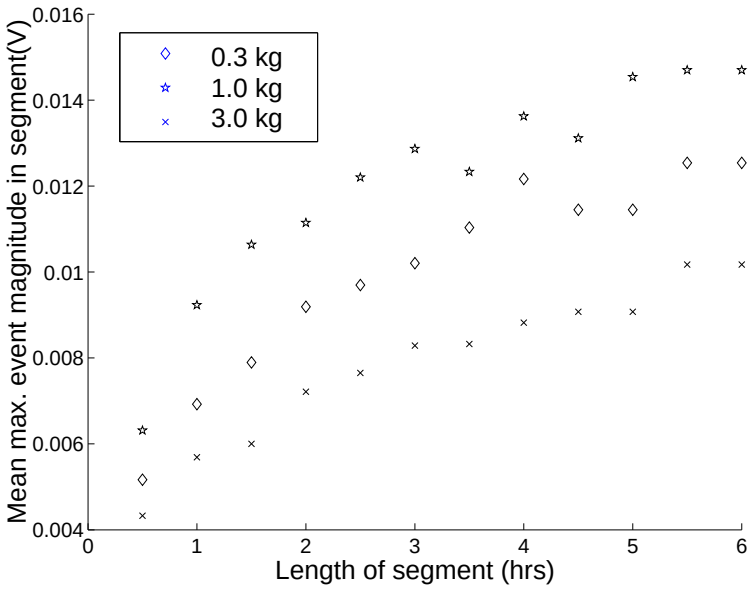

Figure 4.18: The mean maximum event magnitude as a function of segment length plotted for three different normal forces. We see that for segment longer than about 4 hours, the average maximum event magnitude levels of. Note, that the data sets have been scaled in order to fit into the same plot: the 0.3kg set has been multiplied by 5, and the 1.0 kg data set has been multiplied by 3.

The effect of varying the sandpaper grain size

One would guess that by increasing the sandpaper grain size, the slider would get a "better" grip to the carpet, but how will this alter the event magnitudes? We have performed several experiments where the sandpaper rating (average grain size) is the only parameter that has been varied. Sandpaper coarseness is rated according to an industry convention defined by FEPA (Federation of European Producers of Abrasives).[10] The mean size of the grains on the sandpaper decreases with the characteristic number. That is, for sandpaper 180, the mean grain size is 82 μm, while for sandpaper 60, the mean grain size is 269μm. The four coarseness ratings used in the experiments are 60, 80, 120, 180.

In Figure 4.19 we have plotted the probability densities of the event magnitudes for different sandpaper ratings for experiment A. From the figure it looks as if the slope of the power law ($\beta \sim 1.65 \pm 0.05$) is unaffected by the sandpaper coarseness. In Figure 4.20 we have plotted the maximum event magnitudes

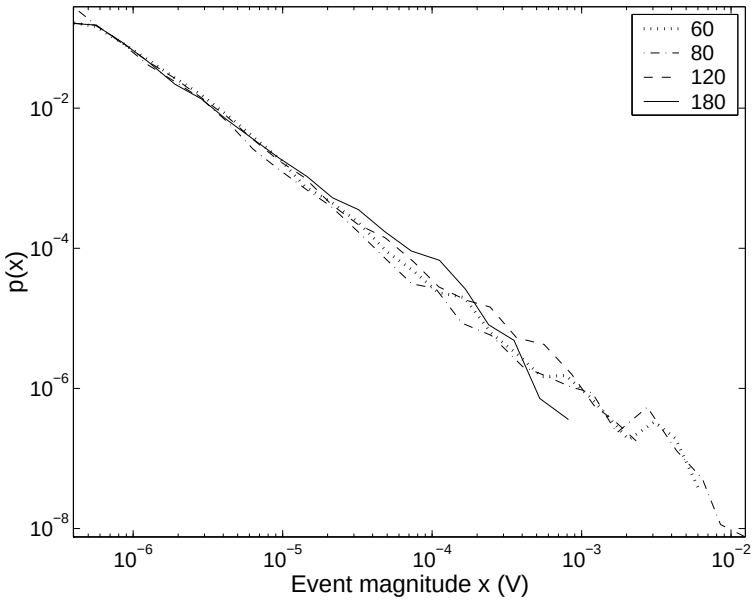

Figure 4.19: The probability densities of event magnitudes for experiment A, where the only parameter varied is the sandpaper coarseness. The sandpaper ratings are listed in the legend, and these values are proportional to the average grain size. Varying the sandpaper coarseness does not seem to have any effect on the exponent β. The value of β is 0.65 ± 0.05 as in the earlier reported values of β for experiment A. Except from the experiment with sandpaper 60, the maximum event magnitude increase with the sandpaper grain size, that is, decreasing sandpaper rating (see Figure 4.20 for more details).

[10] For details see http://www.fepa-abrasives.org/fepap-e.htm

for different sandpaper ratings, and we see that the maximum event magnitude increases roughly with decreasing sandpaper rating. In principle, increasing the

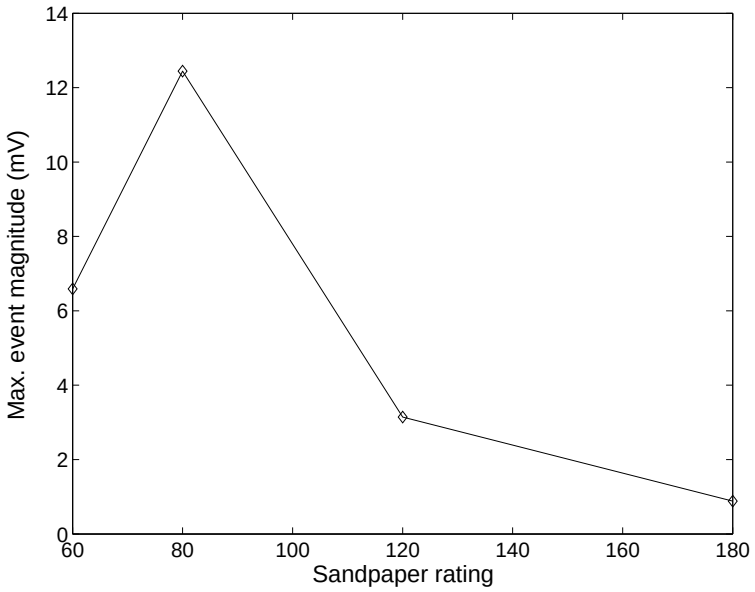

Figure 4.20: The maximum event magnitude is plotted for different sandpaper ratings. We see that the maximum event magnitude decreases when the sandpaper rating increases. However, this is not true for rating 60, where the maximum event magnitude is seen to be lower than rating 80. We have no reasonable explanation for this effect.

coarseness increases the number of asperities, and the quality of their "grip" on the opposing surface – that is, the threshold of total strain that is tolerated before a release happens. On the other hand, a smaller average grain size would grip less effectively onto the "fiber bundles" that make up the surface in experiment A. In Figure 4.20 we see that the maximum event magnitudes, for experiments with sandpaper rating 60, are less than in the data set from sandpaper rating 80. This deviation from the trend is not a statistical coincidence: when performing the same plot, but averaging over different length of the segments, we obtain the same deviation independently of the length of the segment. An explanation for this effect is not clear. We have not performed a variation of the sandpaper rating for other surfaces than in experiment A. It would also be interesting to see how the maximum event magnitude depends on the roughness of other surfaces, such as paper, silicon, rock and metals. These questions remain to be answered in future projects.

The effects of varying the elastic properties of the pulling string

We have also studied the effect of varying the elastic properties of the nylon string (fishing line) used to pull the slider. Stick-slip motion is normally damped by using a "stiffer", or less elastic loading apparatus. This effect is illustrated in figure 4.21, where the stick-slip motion resulting from a paper-on-paper system is plotted for different values of the stiffness of the system (labeled K in the figure). The spring elongation, which is proportional to the pulling force, is labeled Δx in the figure. One can see from the figure that the amplitude of

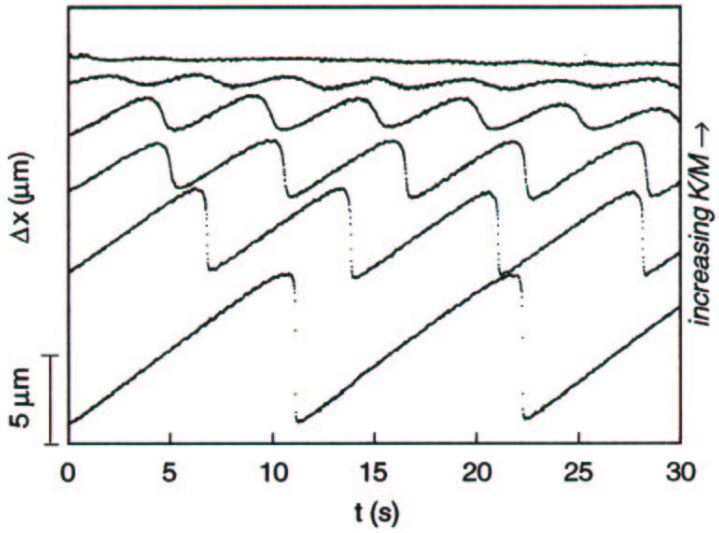

Figure 4.21: The force, which is proportional to the spring elongation Δx, required to pull a paper on paper is plotted for different pulling spring stiffness K (slider mass (M) and velocity are kept constant). The event magnitudes decrease with K, while a rounding of the signal increases with K. That is, the duration time of the event magnitudes increases with K. The figure is taken from [14].

the stick-slip motion decreases by increasing the force constant K (M is kept constant). This happens because Hooke's law states that the friction force (F_c) to be reached before triggering of an event, is $F_c = K\Delta x$, and therefore

$$\Delta x = \frac{F_c}{K}. \tag{4.28}$$

Assuming that F_c is constant and independent of K we can rationalize the decreasing stick-slip amplitude as seen in Figure 4.21. There is a problem with the last assumption: for constant driving velocity, the time of static contact (stick) between two surfaces decreases with K. This will cause F_c to decrease

with increasing K since the static friction is often observed to be dependent on the time of contact (see equation (2.6)). However, in our experiments the mean value of the pulling force before events are triggered does not depend on K' and is fairly constant, and therefore the static aging of the contact is guessed to play a minor role.

In Figure 4.22 we have plotted the event magnitude PDF's for different lengths of the pulling string (see the legend in the plot). Note that the basic configuration is experiment A, but that the string thickness is 0.9mm instead of 0.6mm as described on page 33. This change in the diameter of the string did not affect the validity of the power law nor the value of the coefficient β (for the longest string), but the maximum event magnitude was reduced compared to the experiments with a more elastic string (see for example Figure 4.16 (0.5kg) where a 0.6mm in diameter string is used). For shorter string lengths we see that there is a "rounding" of the power law and that the maximum event magnitude decreases with decreasing string length.

In Figure 4.23 we have plotted the maximum event magnitudes as a function of the force constant of the pulling string. We assume that the inverse of the length of the string is the effective spring constant, K', of the pulling string. We see from the figure that the maximum event magnitude decrease approximately as 1/K, as described in equation (4.28).

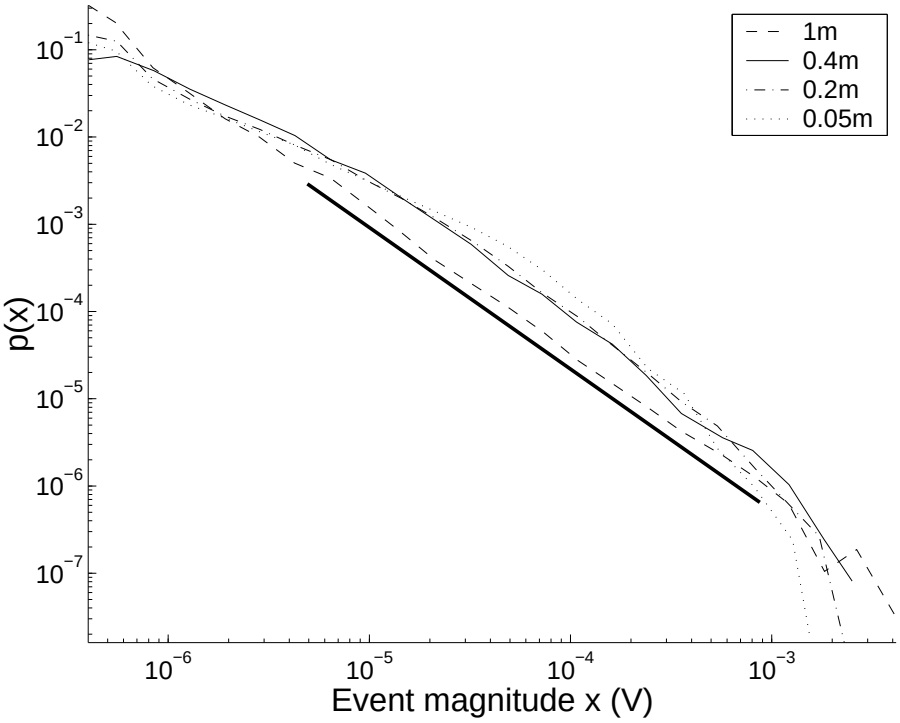

Figure 4.22: The event magnitude (x) probability density, $p(x)$, is plotted for different values pulling string length (experiment A). The elastic string used in these experiments has a diameter of 0.90 mm (0.60 mm is the standard in experiment A), and a varying length from 1m to 5cm (see legend). For the experiment with the string of length 1m, $p(x)$ is a well defined power law with $\beta \sim 1.65 \pm 0.05$ (the slope of the thick solid line). For shorter strings, we observe that there is a "rounding" of the distribution and that $p(x)$ no longer is a well defined power law.

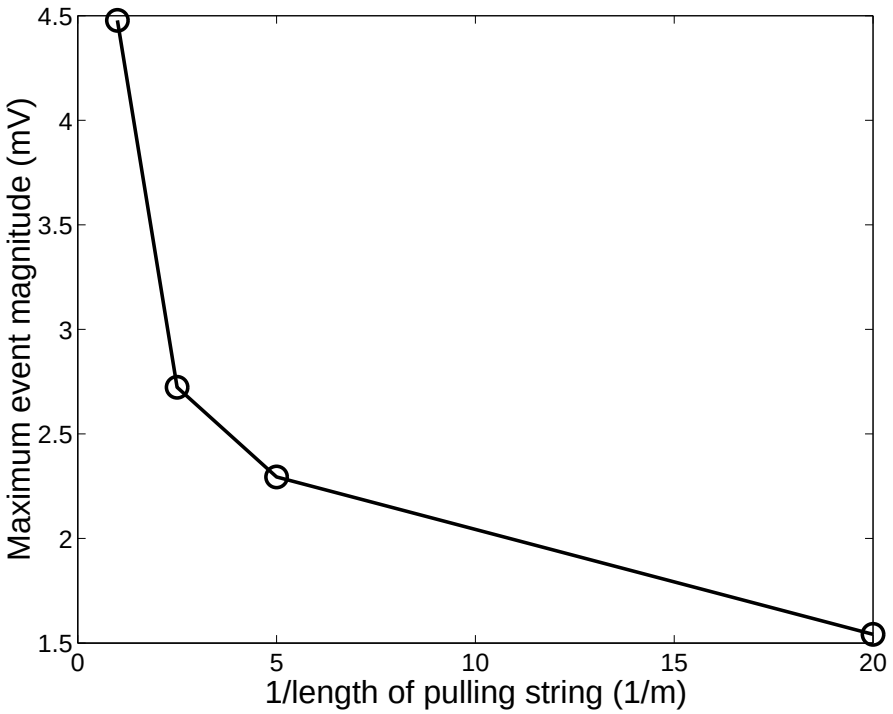

Figure 4.23: The maximum event magnitude as a function of the inverse of the length of the pulling string (assumed to be the effective spring constant of the pulling spring).

Chapter 5

A numerical model of event triggering and propagation.

In this chapter we describe a simple model for the stick-creep motion (SCM) that we observe in the carpet experiment. Previous studies have described the carpet as a quasi-elastic medium [7], so that avalanches of slipping asperities are propagated mainly through a process of local force redistribution. Our own experiments using the Feder-Feder (the carpet experiment) apparatus indicate that avalanches in this sense probably do not occur. Instead, we suggest that the medium is effectively rigid, and that all of the important consequences of a local slip are communicated by the rigid slider in a global perturbation. For a narrow range of realistic parameters, our own "hooked-spring rigid-medium" model produces a power law distribution for event sizes that spans several orders of magnitude, and which has an exponent $\alpha \sim 0.66$ that corresponds to what is measured for surfaces in which only SCM is observed (see Figure 4.1). An analytical solution to a similar model has been proposed in [48], where they calculate a value for $\alpha = 1/2$.

Computational models have been proposed for friction phenomena in a variety of experimental contexts [17, 49, 20, 7, 12, 50, 25]. It has been shown that the elastic properties of the interacting materials will often play a hugely important role in the dynamics of sliding friction [4, 10]. It is nevertheless possible to find materials for which the elasticity of the medium between the asperities is unimportant. In particular, there are materials for which the individual asperities are far more elastic than the supporting medium. In such cases, if the opposite sliding surface is sufficiently rigid, then its motion will communicate globally and almost instantly the important effects of a single slipping asperity. We suggest that the carpet surfaces used in the carpet experiment belong to this category.

This category of systems can be described as a limiting version of a spring-block model, shown in Figure 5.1 [25], where $k_c >> k_l$. This limiting case can

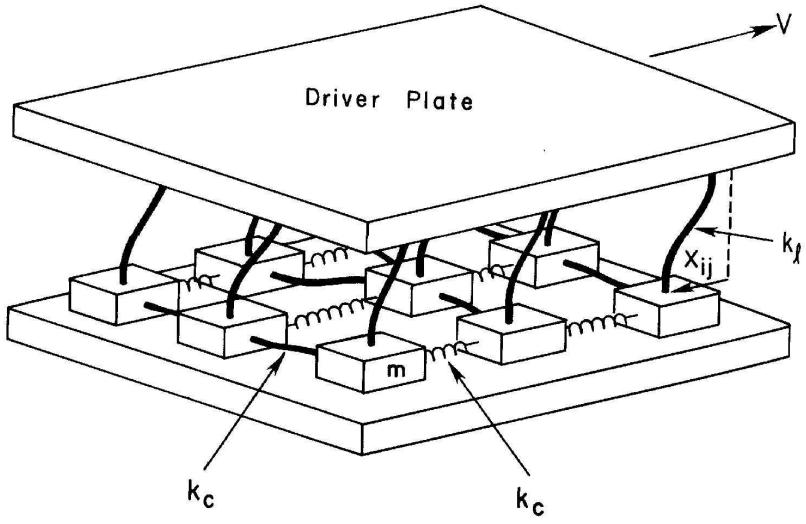

Figure 5.1: A schematic view of a spring block model, from [25].

also be viewed as a fiber-bundle model, with equal load sharing rules [51, 52] [1]. Both spring-block [25] and fiber-bundle models [52] are known to exhibit clear signs of belonging to the class of SOC-systems.

5.1 The SCM model

In this section we describe a model in which the elastic properties of the supporting medium (mat) of the carpets are ignored. We have called into question the assumed quasi-elasticity of the carpet mat for several reasons. First, we have observed that even carpets with a very rigid mat, such as the surface used in experiment A, can exhibit power law behavior for slip magnitudes (Figure 4.1 and 4.3), a behavior that was thought possible only for relatively elastic mats [7, 10].

In the experiments we observe a very clear difference in the exponent of the power law for different carpets, however, this difference can be ascribed to many properties aside from just the elasticity of the mat: for example, these include the elastic properties of the fiber-loops, the arrangement and orientation of these loops, and roughness in the elevation of loops, etc. Moreover, some carpets exhibit only stick-creep motion (SCM), in which the slider moves only by stretching the fibers that are momentarily attached, at times stopping totally, and others exhibit a combination of SCM and stick-slip motion, SSM, during which all fibers become detached and the slider glides across the surface. These

[1] see Figure 5.2 for schematic view of SCM model.

two kinds of surfaces, used respectively in experiment A and B, have been shown to exhibit different exponents (compare Figures 4.1 and 4.3).

The model that we propose in this section is meant to describe SCM in carpets for which only this kind of behavior occurs, however, it has implications for the understanding of SSM also. That is, the model can be used to understand the mechanism that triggers SSM events, because, as mentioned, that kind of motion occurs whenever all asperities have slipped (see Figure 5.5). (N.B. in the following discussion, the word "slip" will often refer to the "release" of individual asperities, which is of course a basic mechanism in both stick-slip (SSM) and stick-creep motion (SCM).)

As mentioned, if all of the attached asperities have slipped, the slider then glides across the surface until it is halted. The mechanism for halting SSM events is discussed in the next section 6. In SCM, it never happens that all asperities have slipped, and events develop and terminate without causing any rapid motion of the slider.

The FF [7] and OFC [25] models describe a friction interaction in quasi-elastic media, and therefore posit a primarily local redistribution of force whenever a single asperity has slipped. These models therefore predict an avalanche-like propagation of slips. These avalanches form contiguous "domains" that connect the asperities involved in SSM and SCM events. Our experimental observations suggest that slipping events probably do not occur in this way. In SCM, we observe that the sound of consecutive slipping events for individual asperities can originate from all portions of the region that is beneath the slider. Moreover, an infrared camera was used to identify the [slightly hotter] asperities involved in large SSM events on carpets for which this kind of motion dominates. It was found that regions involved in SSM events are not contiguous at all. Instead, the slipping asperities are normally isolated, and they are distributed throughout the region that was in contact with the slider (Figures 3.27 and 3.31). It should be acknowledged, however, that these images were not obtained in an experiment for which the slider velocity was slow enough to produce a power law distribution of event magnitudes. Also, it must be acknowledged that some surfaces are far more rough than others, so that neighboring fibers are not necessarily gripping on the slider. Thus, for many surfaces we cannot expect contiguous domains to appear in the infrared images because the gripping asperities are not themselves connected. The idea of using a grid as a contacting surface (as in Figure 3.27) is does not necessarily give the right dynamics of the sliding.

5.2 A detailed description of the model

The hooked-spring rigid-medium model that we propose for SCM in the carpet experiment is illustrated in Figure 5.2. The fiber-loop asperities are represented as hooked springs that are fastened at the base to a rigid plane. The slider is represented by a rigid plane that is dotted with inelastic attachment sites (analogous to the sand grains on the sandpaper). In the calculation, N springs are represented by elements in a list, having a strain ϵ, and a strain-threshold

ϵ_{th}. In the first time step, some elements are assigned a small initial strain ϵ_i, as well as a strain-threshold $\epsilon_{i_{th}}$ that represents the robustness of their grip on an attachment site in the opposite surface. Both quantities are chosen according to a uniform distribution. If a spring is not gripping, then its strain is 0.

In each *macro*-step, the strain on all of the gripping springs (N_g in total) is increased by a constant amount of strain ν divided evenly between gripping springs:

$$\epsilon_i \rightarrow \epsilon_i + \nu/N_g, \ \forall \epsilon_i > 0. \tag{5.1}$$

If an individual spring ϵ_j exceeds the strain threshold that was assigned to its current grip (we assume that ν is so small, and ϵ_{th} so large that only one spring exceeds its threshold at each macro-step), then its strain is set to zero (not gripping):

$$\epsilon_j \rightarrow 0, \ \forall \epsilon_j \geq \epsilon_{j_{th}}, \tag{5.2}$$

and some fraction υ of this strain is redistributed evenly to all gripping springs simultaneously:

$$\epsilon_i \rightarrow \epsilon_i + \frac{\upsilon \epsilon_j}{N_g - 1}, \ \forall \epsilon_i > 0. \tag{5.3}$$

This process is repeated within a so-called *micro*-step until the consequences of all slips have been calculated, and the slipping has stopped (this represents the end of a single SCM or "creep" event). Also, in each micro-timestep, each non-gripping spring is given a chance to grip again, based upon some constant and uniform probability. The total force needed to pull the slider (top layer in Figure

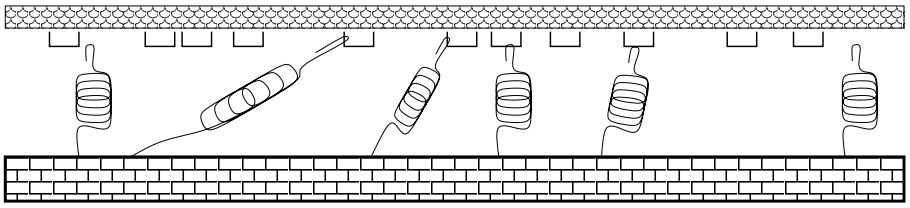

Figure 5.2: Schematic of a one-dimensional cross-section of the hooked-spring rigid-medium model. The slider (top) is here shown moving to the right.

5.2) is then proportional to the sum of the strains of all the gripping fibers. The event magnitudes are then calculated according to the scheme described on page 28.

5.3 Simulation results

The model exhibits several behaviors that are consistent with what is observed for surfaces exhibiting only SCM in the carpet experiment. For a narrow range of realistic parameter values, we obtain power law behavior in the cumulative probability distribution and the density function for event magnitudes (Figure

5.3). The model produces exponents between -0.75 and -0.65 for the longest power laws that so far have been obtained, spanning about three orders of magnitude in event size and probability. The exponents obtained in our experiments for SCM-dominated carpets are within this range (compare Figures 5.3 and 4.1). Plots of creep event magnitude versus creep event number as well as total-strain-in-time are qualitatively similar to what is observed for experimental data (where instead the applied force is measured).

In experiments we sometimes observe an unusually steep rise in tension after massive events, and this is observed in the model also. It is incorrect, however, to make a direct comparison between these observations. In the model, this feature can be ascribed to the effect of many asperities re-gripping suddenly. That is, the effective spring-constant of the total carpet surface is changed suddenly, and the overall strain and resisting force rises sharply (see Figure 5.4). The events that exhibit this feature in the experiments are probably not SCM events at all. Normally this feature is observed at the end of SSM events, and this probably represents the stretching of asperities that have halted the slider motion, and which have a larger effective spring constant than the nylon string (and hence cause a steeper rise in the strain gauge measurements). Once these fibers have stretched to nearly their limit of strain, the usual slope resumes, which reflects the stretching of the nylon string.

The model predicts that for even large numbers of springs (for example, 100), it can happen that all of the springs let go in the course of a single event. This represents the onset of stick-slip motion – the "triggering" of a stick-slip event. When all the springs have lost their grip, the slider is free to move and is halted by a separate mechanism that is described in the next section. Figure 5.5 shows a calculation in which all of 100 springs lose their grip within a single macro time-step.

Finally, the spatial distribution of asperities involved in major SSM and SCM events is consistent with the infrared observations shown in Figure 3.27. That is, these asperities do not form contiguous domains, and they are instead isolated from one another.

The shape of the slip distribution is apparently not sensitive to the initial conditions or to the probability that individual springs will grip again. The distribution of slips is very sensitive to the fraction υ of force that is redistributed to other gripping springs after a single spring has slipped. It is difficult to guess exactly what this quantity should be. Since we posit that the effects of each slip are communicated almost instantly to all gripping springs by the slider, we expect υ to be not far from 1, the conservative case. The model in [7] is based on nearest-neighbor interactions, but it also takes into account that when a loop in the carpet loses its grip not all the force is transferred to the neighboring loops. Force is not conserved. Our model, with $\upsilon \sim 1$ represents therefore the extreme non-conservative case for a rigid mat in the Feder-Feder [7] model.

In figure 5.7 (top) we show how the distribution changes for values of υ in a range from 0.85 to 1.0. That is, the distribution changes from a rounded shape to a power law, and then to a "bent" distribution. All three shapes are observed in our experiments, for different configurations (Figure 5.7 (bottom)).

It is unclear how exactly the model parameters should vary with normal load. The number of asperities or effective contact area should increase with increasing load, however, the effect upon v is not known. Changing the number of asperities alone does not indicate the trend observed in our experiments. That is, in our experiments there is almost no change with decreasing load, until some critical load is reached, after which there is shallowing and rounding of the distribution; the high-magnitude cut-off also decreases with decreasing load (see Figures 4.14 and 4.13).

5.4 Conclusions from the model

In summary, the hooked-spring rigid-medium model is a promising description of the stick-creep motion (SCM) that we observe for some carpets in the carpet experiment, as well as the triggering of stick-slip motion (SSM) events (when all springs are released). We have plans to extend this model to incorporate stick-slip motion, which occurs whenever all asperities are released in a single event (see next section). The model could be extended to incorporate the effects of the slider moving into regions with different numbers of asperities. We hope that this will help us to account for features in the experimental results that are not yet explained. These include, for example, the "clustering" phenomenon observed in plots of creep magnitude versus creep number (Figure 4.12 (a)).

Finally, the model and the experiment illustrate that power law behavior can be observed in non-equilibrium systems for which system-wide communications occur automatically, by means of a global perturbation, and not as the consequence of a self-organizing process.

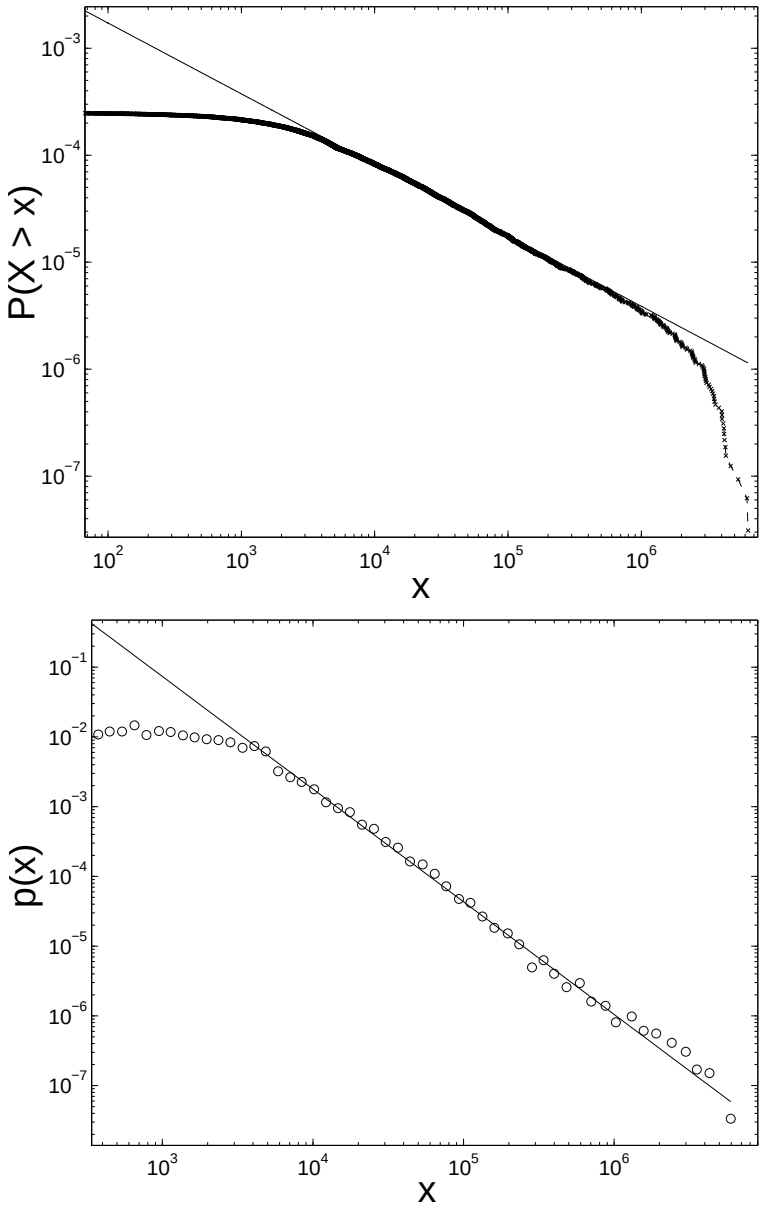

Figure 5.3: Results from the hooked-spring rigid-medium model. Probability density (bottom) function $p(x)$ for the magnitude of events in an interval $x+dx$, with exponent $\beta = 1.62(\pm 0.03)$. The cumulative distribution (top) for event magnitude $X > x$ (the exponent is $\alpha = 0.66 \pm 0.03$). The exact parameter values used for this calculation are supplied on page 163, after the source code for the model in appendix H.

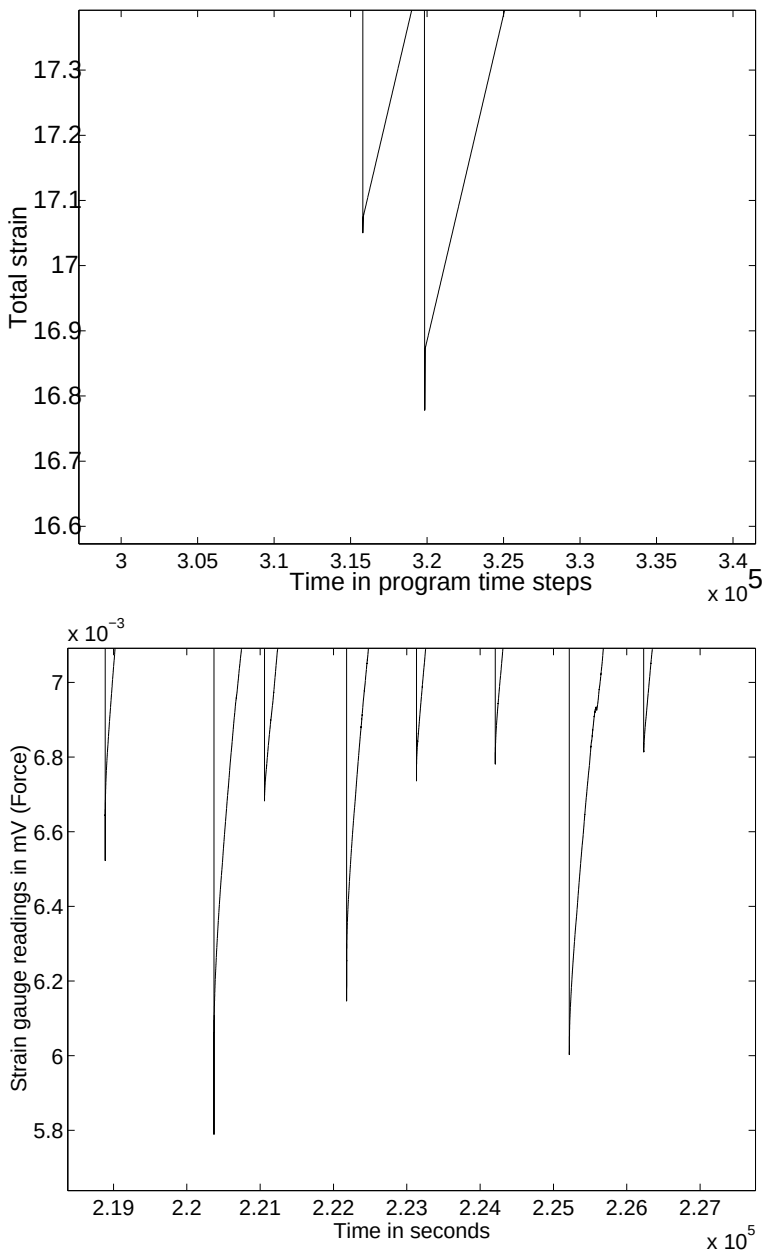

Figure 5.4: Vertical jumps that represent the re-gripping of asperities after massive events, seen here in the total strain versus time for the model calculation (top) and the total applied force versus time for the experiment (bottom). In the case of the experiment, however, this feature is probably the consequence of the asperities stretching after halting the motion of a stick-slip event. (see text)

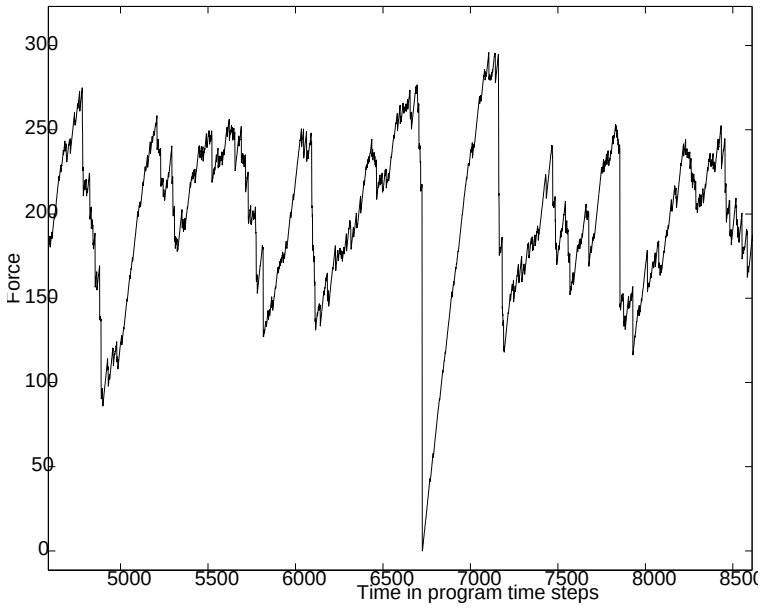

Figure 5.5: This plot shows a triggering of a stick-slip event in a simulation, in which the total strain on all asperities drops to zero. That is, all asperities release their grip on the slider, so that it moves rapidly over the surface. The mechanism for halting stick-slip events is described in chapter 6.

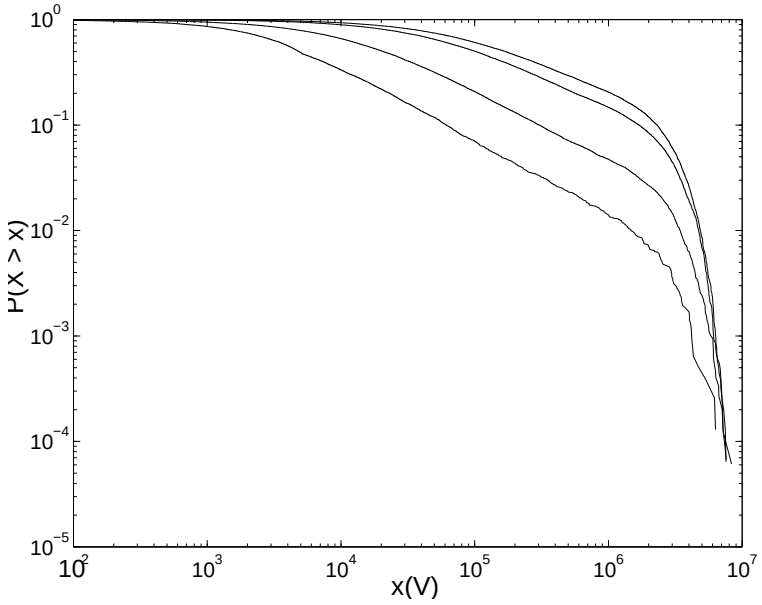

Figure 5.6: Cumulative distribution of event magnitudes x at different values of ν in the model calculation. We observe a shallowing and shortening of the power law as ν increases (from bottom to top of the plots).

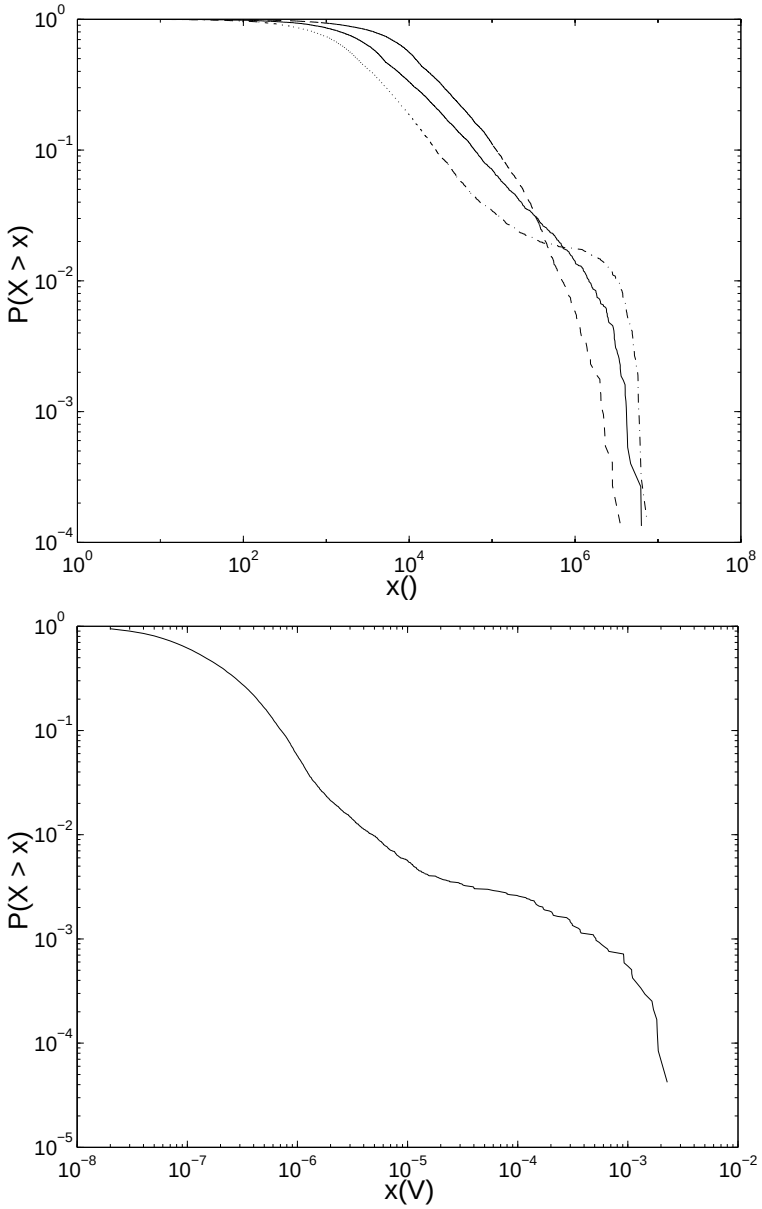

Figure 5.7: Cumulative probability distribution of event magnitudes (simulation) for $\upsilon = 0.85$ (- -), $\upsilon = 0.94$ (–), $\upsilon = 0.97$ (– · –) (top). An example of the "bent" distribution that is sometimes observed in our experiments (bottom). This experiment was carried out on a surface with very low density of loops, and where the loops were relatively thick (a doormat). This shape of the distribution is characteristic for this kind of carpets.

Chapter 6

A numerical model for halting events in stick-slip motion

We have defined stick-creep motion (SCM) as motion that occurs by stretching looped fibers that have attached to the grains on the rigid slider. In SCM, at least one fiber is gripping on the slider at all times. This kind of motion is called *stick*-creep because the slider often halts totally (becomes stuck). In our experiments using the Feder-Feder apparatus, we have encountered surfaces on which only this kind of motion occurs (experiment A). On the majority of surfaces, however, we observe also a second kind of motion, that we call stick-slip motion (SSM). Slipping motion occurs whenever all fibers lose their grip on the grains in the slider. The tension in the nylon string then causes the slider to slide over the surface of fibers until the motion halts again. SCM events last much longer than SSM events, although they have comparable magnitudes. There are two mechanisms for halting this motion, and we shall describe them in the following discussion.

6.1 Separating slips from creeps

So far we have supplied a qualitative definition of SSM and SCM that is based on the physical processes that govern the motion. We now propose a quantitative definition that can be used to distinguish these two kinds of motion in our experimental results. As we have mentioned already, in SCM we find that the event lifetimes are a power law function of the event sizes and that this power law spans three orders magnitude (see Figures 6.1 and 4.7). For the vast majority of surfaces we find a combination of SSM and SCM. In this combined behavior we expect the SCM events to be slowest (lasting longest), since the slider in that case moves only by stretching the attached fibers. Therefore, we can expect

the SSM events to always lie *below* the power law that appears in Figure 6.1, indicating that they are relatively fast. Indeed, in experiments exhibiting the combined behavior we find many events that lie below this line. Our quantitative definition for SSM, therefore, is that SSM events of magnitude m (in V) and duration time λ (s) obey approximately the following rule:

$$\lambda m^{-0.65} \leq 10^{3.8} V. \tag{6.1}$$

For one surface used in a large number of experiments we find that a small fraction of events, about 1 %, are SSM events. Figure 6.2 (top) shows a typical plot of individual event duration time versus magnitude for an experiment in which a combination of SCM and SSM occurs. A line is drawn that corresponds roughly to equation (6.1). A histogram of magnitudes for the events below this line is shown at the bottom of figure 6.2. Since the broad base in the lower left of the duration time vs. magnitudes plot in figure 6.1 probably contains only SCM events, and since this broadening appears also in the equivalent plot for SSM motion shown in Figure 6.2, we conclude that equation (6.1) applies only "roughly" in the low-magnitude regime. In Figure 6.3 we have drawn two lines to separate the SSM and SCM events. The distribution of magnitudes for the events below these lines is shown in the bottom-left of Figure 6.3. The same procedure was conducted for several experiments, and the histograms of SSM event magnitudes are shown at the bottom of Figure 6.3. Note that there is a rise in the number of SSM events toward the high magnitude regime.

Whereas we have shown that the magnitudes of SCM events clearly follow a power law distribution spanning several orders, from these figures it is clear that SSM event magnitudes do not follow a power law, but rather a distribution more like a Gaussian.

It has been suggested that power law distributions of event magnitudes in friction motion indicate that slowly-driven friction is a self-organized critical (SOC) process, such as occurs in other systems that are very slowly driven from their equilibrium states (see section 2.5). We suggest that this may in fact be the case in the context of SCM, where the triggering and comparatively slow propagation of events are perhaps a manifestation of self-organized criticality.

On the other hand, the magnitude of SSM events depend mostly upon the process that arrests the motion of the slider – a process that occurs over comparatively short time scales. It should not be surprising, therefore, that SSM does not exhibit evidence of self-organized criticality. In their original paper regarding the experiment [7], Feder and Feder did not make a distinction between stick-slip and stick-creep, and so it is not known which kind of motion was more prevalent on the surfaces they examined.

A successful model for SSM in the Feder-Feder apparatus (carpet experiment) should anticipate roughly the distributions shown in Figures 6.2 and 6.3. In particular, it should anticipate a clustering of events in the high-magnitude regime, with a small number of events in the middle range of magnitudes. The distribution in the low-magnitude regime is unclear, since this may overlap with the low magnitudes of SCM motion, as discussed earlier.

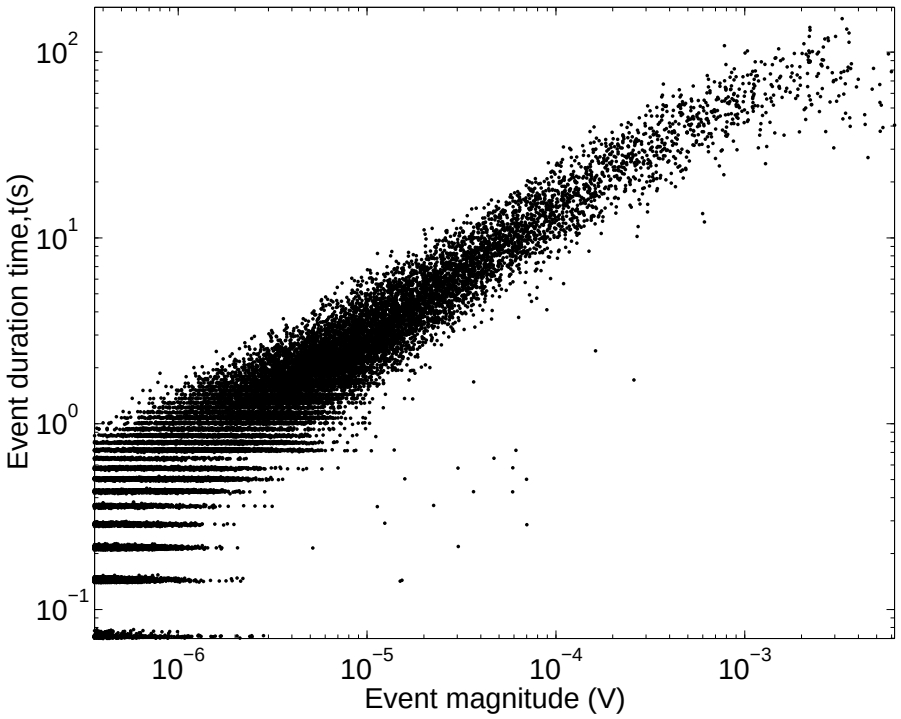

Figure 6.1: Event duration time vs. magnitudes in stick-creep motion. About $50,000$ events are plotted individually (no averaging in contrast to Figure 4.7). The banding in the lower left of the plot is a consequence of limiting measurement resolutions in time and magnitude (the event below the noise threshold have not been sorted out).

6.2 The SSM halting model

In the remainder of this chapter we shall develop a simple model which may account for the manner in which the SSM events are halted, and therefore also the distribution in magnitudes of SSM events.

An "analytical" expression for a slip

First let us consider a simple system in which a slider with mass m is pulled by the tension of a stretched nylon string with an effective spring constant $k_{\rm nl}$ along a smooth rigid surface. The string is initially stretched an amount $x_{\rm nl}$ from its equilibrium length. In the simplest case, the motion of the slider is opposed only by a constant friction term $F_{\rm fr}$.[1] The equation that governs the displacement x

[1] As discussed in section 2.4 this friction term is a function of velocity.

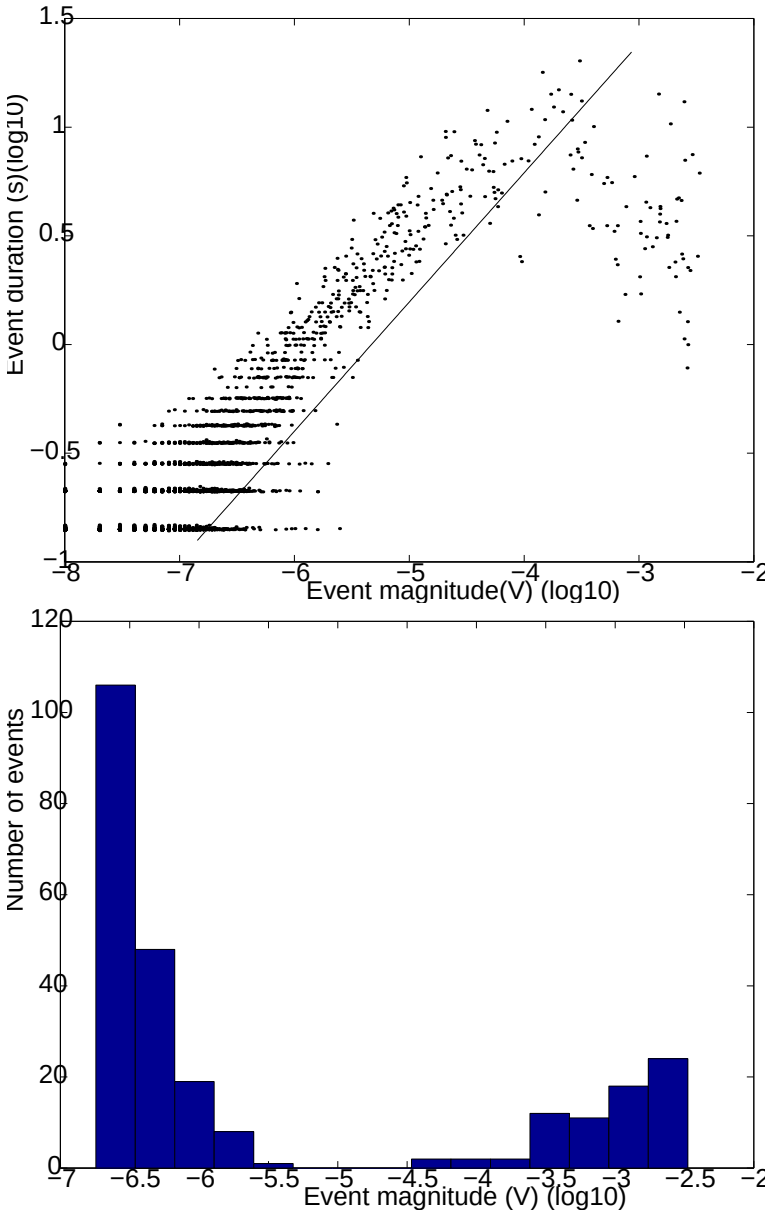

Figure 6.2: **Top:** Event duration time vs. magnitudes in an experiment that exhibits a combination of SSM and SCM. A line is drawn that corresponds roughly to equation (6.1). **Bottom:** A histogram of event magnitudes for events below the line drawn above.

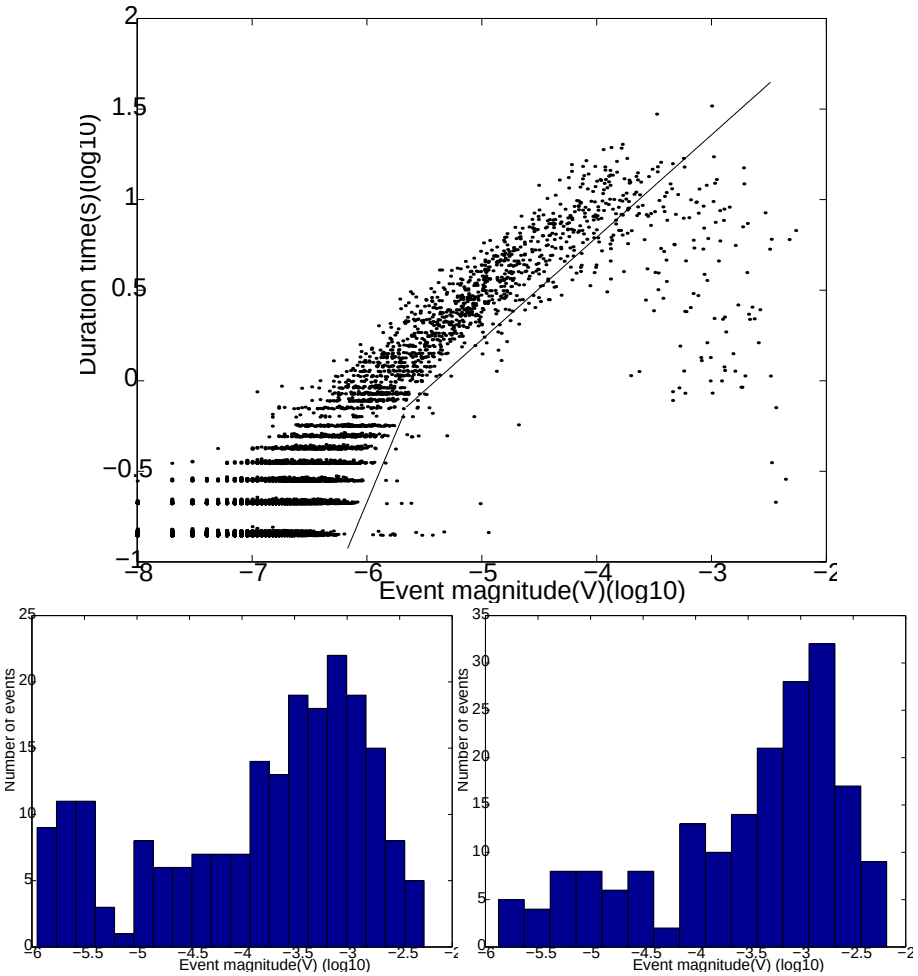

Figure 6.3: **Top:** Event duration times vs. event magnitudes in an experiment that exhibits a combination of SSM and SCM. The magnitudes corresponding to the events below the two lines are SSM events, and a histogram of these magnitudes is plotted below at the far left. **Bottom:** Histograms of SSM event magnitudes for several experiments, chosen according to the scheme shown above. The plot at the left corresponds to the experiment whose events are shown above. The other are taken from a separate experiment.

of the slider from equilibrium is just:

$$m\ddot{x} = k_{\rm nl}(x_{\rm nl} - x) - F_{\rm fr}. \tag{6.2}$$

Letting $\alpha \equiv k_{\rm nl} x_{\rm nl} - F_{\rm fr}$, and $\omega \equiv \sqrt{\frac{k_{\rm nl}}{m}}$, equation (6.2) becomes:

$$\ddot{x} + \omega^2 x = \frac{\alpha}{m}. \tag{6.3}$$

If $\dot{x}(0) = 0$ and $x(0) = 0$ the solution is given by:

$$x(t) = \frac{\alpha}{k}(1 - \cos \omega t). \tag{6.4}$$

The motion stops at a time τ when the velocity becomes zero, $\dot{x}(\tau) = 0$. The duration time τ and the total displacement Δx (a measure of the event magnitude), are given by:

$$\tau = \pi \sqrt{\frac{m}{k_{\rm nl}}}\,, \tag{6.5}$$

$$\Delta x = 2(x_{\rm nl} - \frac{F_{fr}}{k_{\rm nl}}). \tag{6.6}$$

Not surprisingly, the event magnitude (proportional to Δx) depends on the microscopic friction, the elastic properties of the nylon string, and the amount by which the string was initially stretched from its equilibrium length (where $k_{\rm nl} x_{\rm nl}$ is greater than the force of static friction on the slider). The event duration time τ, however, depends only on the slider mass and $k_{\rm nl}$. Therefore, if this simple model were correct, then all events measured for a single experiment with the same mass and nylon string would last the same amount of time. Of course we know that this is not true, and therefore clearly another mechanism aside from microscopic friction is needed to account for the halting of the slider in the carpet experiment.

We suggest that a moving slider is stopped by two processes. First, the elastic fiber loops occasionally become attached to grains in the slider and can snap or otherwise let go. If the slider velocity is small enough and the attachments are strong enough, then the attached loops can halt the motion of the slider. The second mechanism is the microscopic friction that was just illustrated, and which occurs between the unattached fibers and the slider. If no fibers become attached to the slider, then this microscopic friction can halt the slider's motion. In the absence of this microscopic friction, the tension in the nylon string could disappear totally and the slider would continue moving at a constant velocity. In our model, the microscopic friction is represented by a constant term, even though in reality it has been shown to have a velocity dependence (see text in section 2.4, and Figure 2.8).

First we provide a general description of our model, and then we list all of the steps in the algorithm used to process each time step. All parameters and variables in the model are listed in Table A.2. Note that variables whose values change in time are represented as functions of t_n, where t_n represents the time at time-step number n.

A detailed description of the halting model

The model consists of a rigid slider that is covered with small attachment sites, and a rigid surface that is covered with hooked springs that may hook onto (become attached to) the attachment sites on the slider. There is a net force F pulling on the slider at the start of the event, supplied by tension in the nylon string, given by $k_{\rm nl}x_{\rm nl}$. All quantities are positive in the direction of motion, and $x_{\rm nl}$ is the amount by which the nylon string is stretched from its equilibrium length. Changes in velocity and position are calculated at the beginning of each time step based on the current value of the net force F. Initially there are no springs attached to the slider[2] ($N_{\rm grip} = 0$), so that the total force is just the nylon spring tension minus the constant microscopic friction force $F_{\rm fr}$.

A list is maintained of $N_{\rm hs}$ springs and their displacement-from-equilibrium-lengths (that is, x_i for $i = 1, 2, ..., N_{\rm hs}$). In every time step, each of these has an equal probability of becoming attached to the slider, given by $p_{\rm grip}$. If the displacement-from-equilibrium-length x_i of spring number i that happens to be attached (so that $x_i > 0$) exceeds the maximum allowed length $\delta x_{\rm max}$, then this spring releases or snaps, so that once again $x_i = 0$. The force is re-calculated at the end of each time step as the sum of the nylon string tension, the microscopic friction, and the sum of tension in all of the $N_{\rm grip}$ attached springs. In what follows, the steps in the algorithm for processing each time step are listed in detail. Before the motion begins, $x(0) = 0$, $v(0) = 0$, $N_{\rm grip}(0) = 0$, and $F(0) = k_{\rm nl}x_{\rm nl} - F_{\rm fr}$.

1. The velocity and position are calculated from the force in the previous time-step, $n - 1$:

$$v(t_n) = v(t_{n-1}) + \frac{1}{m}F(t_{n-1})\delta t \tag{6.7}$$

$$x(t_n) = x(t_{n-1}) + v(t_n)\delta t. \tag{6.8}$$

2. Then, for each spring i of $N_{\rm hs}$ springs that are allowed to grip:

   - (a) if $x_i(t_{n-1}) = 0$ (that is, not attached), then a random number $R \in [0, 1]$ is chosen. If $R > 1 - p_{\rm grip}$ then $x_i(t_n) = v(t_n)\delta t$ (that is, now attached).
   - (b) If instead $x_i(t_{n-1}) > 0$ (that is, attached), then $x_i(t_n) = x_i(t_{n-1}) + v(t_n)\delta t$. However, if $x_i(t_n) > \delta x_{\rm max}$ (that is, spring snaps) then we set $x_i(t_n) = 0$.

3. The force is then updated as follows:

$$F(t_n) = k_{\rm nl}(x_{\rm nl} - x(t_n)) - F_{\rm fr} - k_{\rm hs}\sum_{i=1}^{N_{\rm hs}} x_i. \tag{6.9}$$

4. The total time is updated: $t_{n+1} = t_n + \delta t$, and the next time step begins.

[2]Remember, this is the definition of a slip in SSM.

Simulation results

Plots showing the behavior in time of the velocity v and position x of the slider, as well as the force F on the slider and the number of gripping springs N_{grip} are displayed for a typical calculation in Figures 6.4 - 6.7. The force and velocity decline sharply whenever a spring manages to grip on the slider. Nearing half the total duration of the event, the slider's inertia overwhelms individual springs that attach and let go, and the motion continues. The velocity eventually reaches a maximum value, after which the microscopic friction force overwhelms the string tension, and the slider begins to slow down. When one or two springs manage to grip in this low-velocity phase, they are more likely to maintain their grip and halt the motion (as happens in this case). It is of course possible for several springs to become attached in the high-velocity phase, and of course the motion is more likely to stop also in the low-velocity phase at the start of the motion.

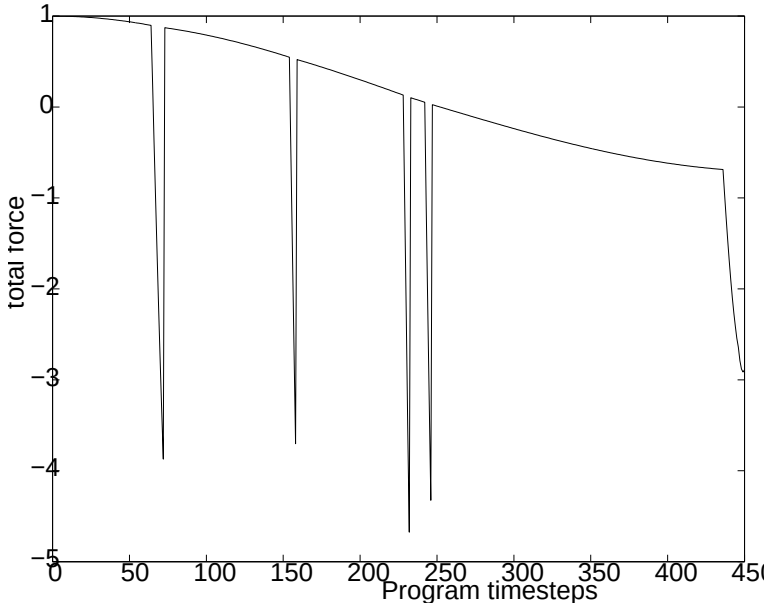

Figure 6.4: Force in time for a calculation with the following parameter settings: $m = 0.0001$, $\delta t = 0.0001$, $p_{\mathrm{grip}} = 0.002$, $N_{\mathrm{hs}} = 5$, $k_{\mathrm{hs}} = 100.0$, $k_{\mathrm{nl}} = 0.05$, $x_{\mathrm{nl}} = 12.0$, $F_{\mathrm{fr}} = 5.0$, $\delta x_{\mathrm{max}} = 0.05$. Other plots for the same calculation are shown in Figures 6.5 through 6.7. Sharp negative excursions represent individual springs attaching on the slider, and in the first several cases these subsequently lose their grip or break.

We have plotted histograms of 10 000 event magnitudes for constant x_{nl} and for different values of the gripping probability p_{grip} These magnitudes are measured in terms of total slider displacement, which is proportional to the net change in the nylon string tension (which in the experiment is inferred from

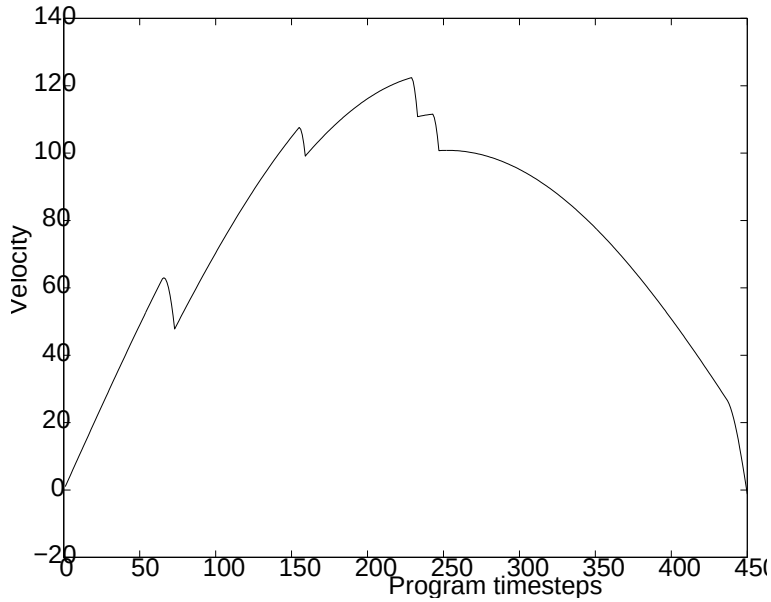

Figure 6.5: Velocity in time for the same calculation as shown in Figure 6.4 (see the corresponding caption for parameter settings). Sharp negative excursions represent individual springs attaching on the slider and then losing their grip. The velocity reaches a peak and then begins to diminish when the nylon string tension is overwhelmed by the microscopic friction term. In the low-velocity regime near the end of the event, two springs become attached and remain attached and halt the motion of the slider.

the strain gauge measurements). These histograms are shown in Figure 6.8. The exact values of p_{grip} that are used to produce histograms of these shapes depend upon the values of other parameters such as the slider mass m, the number of springs N_{hs}, and the starting force value $F(0)$ (these values are supplied in the caption to Figure 6.8). When p_{grip} is too small, nearly all events are halted by microscopic friction, and there is a tall and narrow distribution of events in the high-magnitude regime. On the other hand, when p_{grip} is too large, barely any events are able to surmount the first low-velocity phase. That is, if the gripping probability is too high, then all events are halted before the slider is able to accelerate very much. If p_{grip} is somewhere between these two extremes, then the situation resembles our experiment, in which the microscopic friction and the hooked springs combine to halt events of all magnitudes.

The model is able to reproduce the cluster of high-magnitude events observed Figures 6.2 and 6.3. Notice that in the range of values for p_{grip} that is relevant to our experiment, there is also a cluster of events in the low magnitude regime. Recall that when we count *all* events that obey equation (6.1) in an experiment, such as was done in the case of Figure 6.2, we observe a cluster of low-magnitude events for SSM in the experiment also.

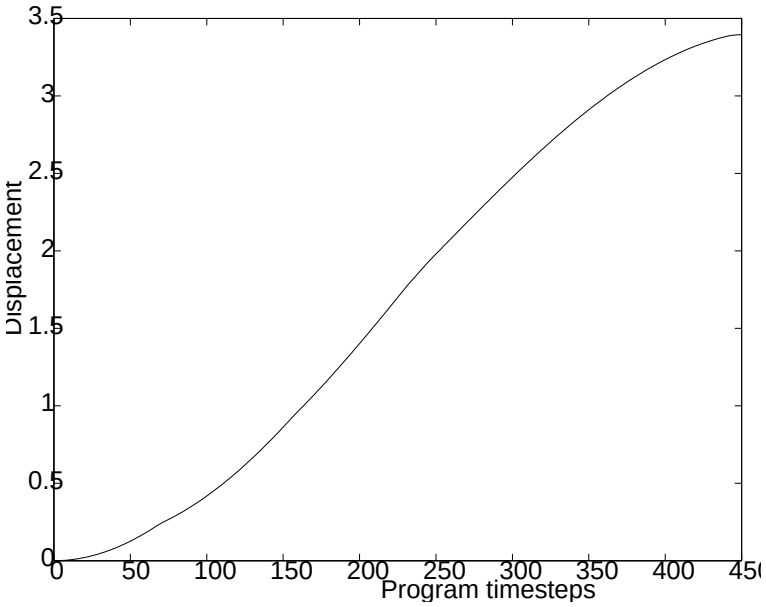

Figure 6.6: Slider displacement in time for the same calculation as shown in Figure 6.4 (see the corresponding caption for parameter settings).

The model is able to confirm the important qualitative features of the event magnitude distributions that are observed in experiments. Recall, however, that we obtain this distribution for a single value of x_{nl}. That is, the starting force value $F(0)$ is constant in these calculations.

The starting force values in reality (from experiments) follow an approximately Gaussian distribution. So far we have not tried selecting x_{nl} from a Gaussian distribution, however, we expect that this will have the effect of smearing the distribution in magnitudes and duration times. Moreover, when this step is taken, it may be interesting to plot the individual event duration times versus individual event magnitudes, where this might be expected to resemble what is found in experiments.

In sum, we have shown that the distribution in magnitudes observed in stick-slip motion (SSM) does not follow a power law distribution, and instead exhibits clustering in the high-magnitude regime. Moreover, we have presented a simple model that suggests a mechanism for the manner in which SSM events might be halted, and which reproduces an event magnitude distribution that is similar to what is observed in experiments. The MATLAB source code for this model is listed in Appendix E, with some of the variable names changed. There are several improvements that should be undertaken in the future. First, the gripping probability p_{grip} is constant in the model, although in reality it is a function of time and velocity. In particular, we expect that this probability is

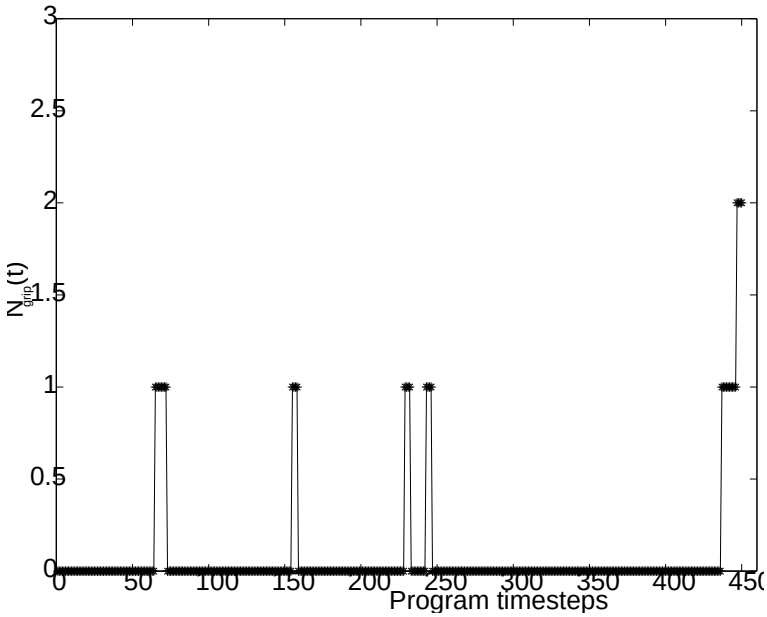

Figure 6.7: Number of attaching springs in time for the same calculation as shown in Figure 6.4 (see the corresponding caption for parameter settings).

inversely proportional to the slider speed.

Finally, one may speculate about the relevance of this model to the case of microscopic friction. In that case, one might imagine a much larger number of hooked springs representing atomic asperities (that is, in our calculations we normally use around 20), and the microscopic friction force would of course be omitted. For this last reason alone, one could expect the behavior to be very different. That is, in the microscopic case, halting of the motion would be accomplished by scores of hooked springs gripping and snapping, and there would not be a constant force term opposing the motion.

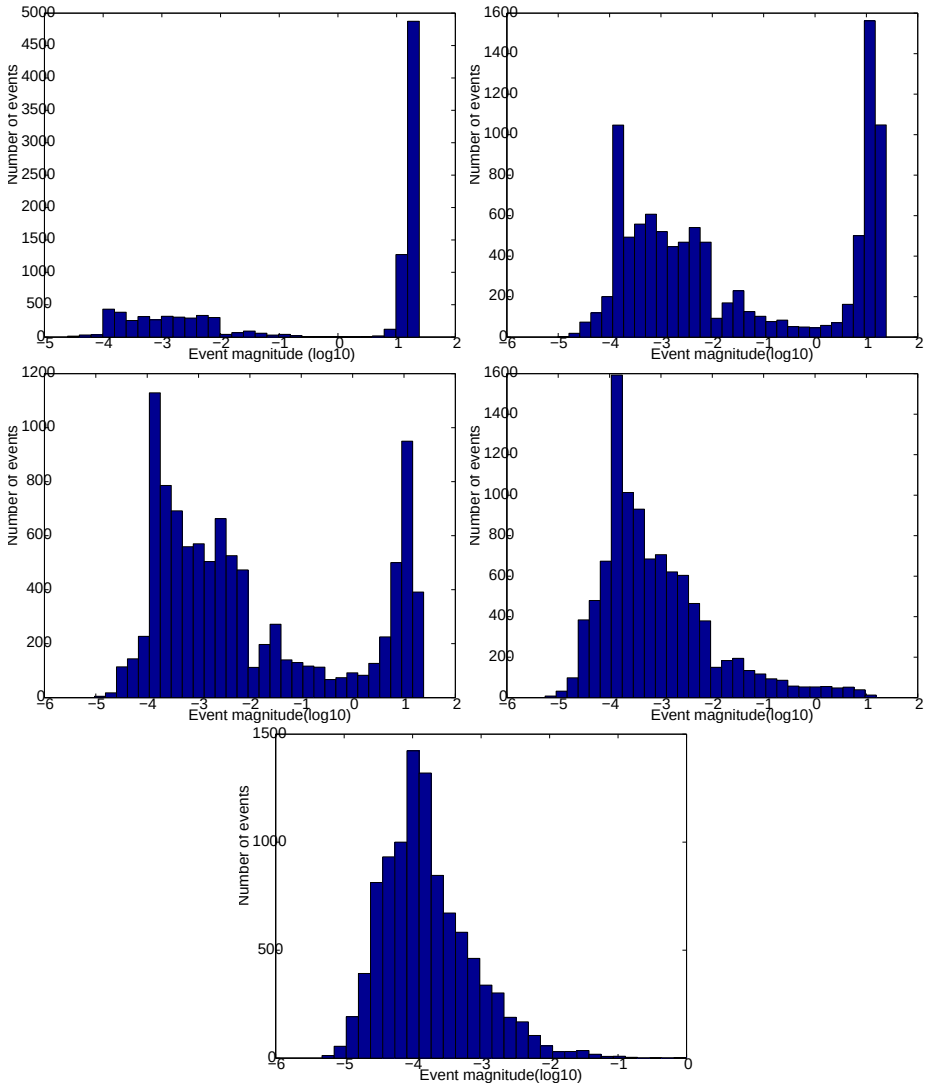

Figure 6.8: Histograms of SSM event magnitudes for several calculations. For all of these calculations, the following parameters have the same value: $m = 0.0001$, $\delta t = 0.0001$, $N_{\rm hs} = 5$, $k_{\rm hs} = 100.0$, $k_{\rm nl} = 0.05$, $x_{\rm nl} = 12.0$, $F_{\rm fr} = 5.0$, $\delta x_{\rm max} = 0.05$. From left to right, the values of $p_{\rm grip}$ are, respectively: 0.0005, 0.001, 0.00125, 0.0025, 0.005.

Chapter 7

Discussion and conclusions

In this chapter we begin by evaluating of the methods used in obtaining and analyzing data from the experiments. A discussion regarding uncertainties and errors in the data and their effect on the general results are presented. We also discuss possible improvements or changes to the different apparatuses and methods we have used. Possible conclusions and new hypotheses drawn from our experiments are discussed in section 7.2. Suggestions for further work related to the carpet experiment are presented in section 7.4.

7.1 The "quality" of data from experiments

Before we started the experiments, thorough investigations of fluctuations in the signal were made in order to understand and minimize these. In general, there are two kinds of errors, systematic and random errors. In section 3.2, where we discussed the noise in the system, we did not discern between these two groups of errors and referred to them both as noise. Without systematic errors, random errors will tend to spread successive readings about the true value of the quantity. If systematic errors are present the reading will spread about some displaced value.

Systematic errors might arise because the experimental arrangement is different from that assumed in the theory, and no correction factor is taken into account. Most of the proposed sources of noise in the experiments, can be categorized as systematic errors. Methods of reducing these was described in section 3.2. Because our experimental results have been described in a rather qualitative way, uncertainties in the slip magnitudes caused by systematic errors or random errors are believed to be of little importance. One reason for this is that whenever we calculate the exponent of the power-laws, we perform the regression for magnitudes greater than what is believed to be the noise threshold. By calculating the exponents using both the density function and the cumulative function we can roughly estimate the value within ± 0.05. The main source of uncertainty in the power-law exponents does not originate from the estimation

of the probability density or the cumulative distribution, but rather in the range that we choose to fit the linear regression. The few judgments made on the basis of different values of the power-law exponents, have been well justified within this uncertainty.

However, there remain experimental observations that have not been explained, and which might be related to systematic errors in the experiments. For example, in most experiments there are clusters where the density (in time) of low magnitude slips[1] is much lower, or higher than in other parts of the experiment. Possible physical mechanisms for this phenomenon were discussed in section 4.2. A strong candidate for the cause of these effects, is the motor that is used to pull the slider. A more powerful and robust pulling system should be a natural upgrade of the experimental apparatus. A linear motor, connected directly to the elastic string could be a good substitute for the current method of pulling.

In section 3.3 we described novel methods of recording information from the carpet experiment. These were: a microphone for recording the sound produced by the breaking fibers, and an IR-camera for measuring, among other things, dissipation. It is important to stress that these methods of exploring friction are only exploratory, and the results that have been presented in this thesis were only in order to show the feasibility of the methods. Additional improvements of these methods must be made before they can be used to extract more useful information. Such improvements will be discussed in section 7.4.

7.2 Strange kinds of friction

Through experiments, observations and simulations we have found that the frictional mechanisms in the carpet experiment can be described through a "hooked-spring rigid-medium" model. This makes the carpet experiment a rather "hard to grasp" -analogy to sliding friction, for several reasons:

- In the carpet experiment, the otherwise very complex mechanism of junction-interactions [2] is replaced by stretching, breaking and re-gripping of nearly elastic springs (fibers).
- Interactions between the asperities on each surface, that is, between sand grains and between carpet fibers, are extreme. That is, the interaction among the asperities is based upon the principle of equal load sharing, a mean field type of interaction.
- The bulk of the contacting materials is of little importance: only the properties at the contact interface appear to matter.

On the other hand, our experiments show many of the same properties as sliding friction do. First of all, the dissipation when an asperity breaks or loosen its

[1] slips less than the estimated "noise threshold".

[2] which in general friction might involve mechanisms such as both plastic and elastic deformation, plowing, adhesion, work hardening, aging, and even the total history of the sliding.

grip, is easily heard or measured with an IR-camera. As in normal friction, the real contact area is much smaller than the apparent contact area (as visualized with the IR-camera) and the normal friction force resisting relative motion, stems from the details at the interface between the surfaces. The behavior in the first part of our experiments, namely when the force builds up and then suddenly drops to a steady state regime, is quite characteristic for normal friction experiments (compare Figure 2.5 and 3.4).

Other friction experiments

Other stick-slip friction experiments have also found a power-law distribution of slips using surfaces with similar properties as in the carpet experiment. In [24] the surfaces have a well defined artificial roughness and elasticity. The roughness is created by steel spheres (d = 2mm). The spheres are mounted rigidly onto one surface, and into silicon rubber on the other. The elastically mounted spheres are allowed to move only in the plane of the surface. Whether the spheres in silicon can be said to interact on a local or purely global scale is not sure, but a power-law distribution of slips, with an exponent $\beta \sim 1.6 - 1.8$ was reported. Power-law distributions of slip magnitudes have also been reported for paper on paper [20] and steel on steel [17], although with a dynamical range of the power-laws spanning only ~ 1.5 orders of magnitude. Therefore, it is no doubt that a power-law distribution of slips is not restricted to the special friction case in the carpet experiment: it might be that this special property of friction must be added to the list of refined friction laws on page 18.

Other simulation results

The authors in [20, 24] suggest that the stick-slip dynamics observed on rocks and paper, is well described by phenomenological state- and rate-dependent friction model (SRF). That is, at a multi-contact interface (MCI) they use the revised friction laws (described on page 18) for each contact point. The SRF model has been extensively validated on very different materials, such as paper and polymer glasses [49].

The much sited Olami-Feder-Christensen model (OFC) [25], also mentioned in section 5, is known to produce events that are power-law distributed. The events (or avalanches) in this model, take place through contiguous domains of moving blocks. It is known that the power-law exponent of events in the OFC-model can be tuned by varying the dissipation factor [53].[3] It is interesting to note that in the carpet experiments we are also able to "tune" the power-law exponent by changing the carpet type. Although we have found power-laws for only two different types of carpet, we believe it is possible to obtain other exponents by tuning the surface types. Of great relevance to this, is the fact that the Guthenberg-Richter law of earthquakes does give a power-law exponent that

[3]However, this is the case only for certain boundary conditions [53], where there is a convergence towards a constant exponent for various values of the dissipation factor. Whether or not the OFC model is critical or not, is also heavily debated.

is not universal. That is, the exponent b (equation 3.1), is highly dependent on both the size of the event and its location worldwide. Smaller earthquakes tend to be described by a smaller value of b, than bigger events do. It is not clear what decides the value of the exponent, but it has certainly something to do with the nature of the surfaces in contact. A more systematic study of the value of β in our experiments might tell us something about the connection between surface properties and the value of the exponent.

Different classes of stick-slip friction

The statistical distinction we have made between stick-creep motion (SCM) and stick-slip motion (SSM) (see definition on page 82) has not been extensively studied by others. These fundamentally different definitions of a slip-event might represent a way to categorize different stick-slip systems, as we have seen from the fundamentally different slip statistics of the two systems. Both SCM- and SSM-systems have been reported, as well as a mixture of these. It would be interesting to find out whether the reported experiments that produce power-law distributions of slips [20, 24] consist of SCM or SSM (or a mixture of both), and whether the temporal aspects of the slips has been investigated. Another interesting avenue is to explore earthquake data and determine whether there is a fundamental difference in both the spatial and temporal propagation in earthquakes, depending on which fault zone is investigated.

7.3 Conclusions

The first aim of this thesis was to reproduce the experimental results obtained in [7]. Slight modifications to the original experimental setup were introduced, such as keeping the elastic string at constant length and fastening the carpet with a double sided tape. Other type of carpets were also explored.

For several surfaces (carpets) we found a power-law distribution of (slip and creep) event magnitudes, although with a lower exponent β than reported in [7]. No clear dependence has been found between the value of β and parameters other than carpet type. For the carpet with the high density of gripping loops (experiment A) we found $\beta \sim 1.65 \pm 0.05$, while for the carpet with the lower density of loops (experiment B) we found $\beta \sim 1.45 \pm 0.05$. In addition to reproducing the results found in [7], we have also explored the temporal properties of the events. For surfaces with a high number of gripping points (like experiment A) the distribution of event duration times is equally well described with a power-law. We have also found that the slips are statistically independent by calculating the waiting time between the slips. A relationship between the event magnitude and its duration time has also been found to be described by a power-law. The value of the exponent for this relation is found to be consistent with a scaling relation for the joint distribution.

The observed stick-slip motion has been divided into two classes, stick-creep motion(SCM) and stick-slip motion(SSM), where only systems exhibiting SCM

(experiment A) or a mixture of SCM and SSM (experiment B) will produce a well defined power-law distribution of slips.

The broad range of event magnitudes that we observe in our experiments, can be attributed to a self-similarity, where the friction laws look the same at different length scales. This self-similarity is expressed through power-laws, and should lead to a method for scaling experimental data. In the general case this leads to universal scaling functions – where some predict the real power lies [6]. By varying parameters such as the normal force, sandpaper rating, and pulling string elasticity we have investigated how the characteristic length scale of the system has responded to these perturbations. A data collapse of the event distributions and possible universal scaling laws has however not been found. There are two possible reasons why a scaling law of the distributions has not been found :

- There is too little data. Data from several identical experiments must be collected in order to obtain a well defined crossover scale. This is necessary in order to do a data collapse.
- Because of the mean-field character of the system, the finite-size effects of the system are only visible as a constraint to the maximum event magnitude, and not as a crossover scale to an exponential-like decay of the power-law.
- The system might simply not be large enough for finite-size effects to be prominent.

Although no finite-size scaling function of the event distributions has been found, we have observed how the maximum event magnitude in most cases varies systematically with the changed parameter, without altering the power-law exponent. This can be taken as a sign that we really observe a finite-size effect and that a scaling function should be possible to find with more data available. A further discussion of whether this is the case or not, is out of the scope of this thesis, but in the next section we propose several experiments with the aim of exploring this.

By investigating the slips using both a microphone and an IR-camera, we have gained insight into the fine temporal details, the dissipation and the geometry of the slips. Based on observations using these techniques, we have developed a model of SCM. This model reproduces the experimentally observed results, not including the temporal domain since this is not included in the model as yet. We have also produced a model that describes the halting of SSM events.

From the SCM model and our experimental results we have found that systems that respond globally to a local perturbation might exhibit many of the same properties as SOC-systems do. We are also the first to report of a power-law distribution of event duration times in connection with stick-slip phenomena. Most explanations for the connection between SOC and friction have taken the form of spring-block models where local interactions are held responsible for the scale invariance observed in simulations [7, 54, 25]. This lack of local interactions

in our model and most probably the experiments might supply new insight to the discussion regarding whether friction can be sufficiently modeled and simulated without the complex interaction between the contacting asperities and the rest of the material [50].

7.4 Future projects

Many of the topics, experimental methods, models, and theories presented in this thesis have, because of limited time and unlimited curiosity, not become fully developed and explored. A lot of ideas and projects are therefore ready to be carried on. Some of the projects have already been mentioned in the text, but we will try to summarize them in this section.

Experimental projects

- Improvements to the experimental apparatus include a bigger and more stable motor and driving system. A linear motor would be perfect for this job. A mechanism for avoiding the platform to drift should be added as well.

- Attempts at finding finite-size effects or crossover scales should be carried out in a more rigorous fashion. Selecting only a few parameters to be explored and then run multiple identical experiments (at least 5) to collect enough data for good statistics, is important. The parameters that should be varied are:

  - The area of the slider
  - The normal force
  - The slider speed
  - The elasticity in the pulling string, for finding a crossover between power-law and another distribution of slips.

  Different strain gauges for higher or lower loads are available at the lab and should be used to optimize the dynamical range

- We have not conducted experiments at higher pulling velocities to see if the classical and the refined laws of friction (see section 2.4), that is, whether velocity weakening and strengthening, is valid with the carpet experiment.

- Recording the sound from the experiments has proven very interesting, but because of attenuation of the sound over the slider, several microphones (at least 3) are needed in order to correctly assign sound amplitudes to both slip localizations and slip magnitudes. Techniques of real-time filtering out only the interesting "clicks" (cutting off the background noise) have been developed, but must be improved if a perfect correlation with the force readings should succeed.

– The methods of recording the dissipation with an IR-camera should be improved a lot, and should be tested on other material combinations as well.

– Using a slider/sandpaper which is much more elastic in both the plane of sliding and in bulk could be interesting in connection to the localization and propagation of slips (and IR recording of them), and how this will affect the distribution of slips.

– Stick-slip experiments should be carried out with different materials to explore the validity of the SSM halting model. High speed recording of both force, audio and IR should then collect very interesting information about single slips. A high speed video recording would also be interesting to find out more about the halting mechanism.

Simulation projects

– Find out whether the amount of parameters in the SCM model can be reduced without a loss of validity.

– Introduce time into the SCM model. In this way the temporal aspect of the experimental results can be more rationalized and tested. Since there is no time scale in our SCM model, the effects of velocity and time on friction, have not been studied.

– The halting model should be explored further, together with the new experiments (see experimental projects).

Appendix A

List of symbols

Latin

F	The friction force
$F(t)$	The pulling force
$F'(t)$	The derivative of the pulling force
x	The event magnitude in our experiments
N	The normal force
M	Mass of slider and platform (all moving parts in the experiment), page 37
g	Gratviational constant
m	The seismic moment of an earthquake
b	The Guthenberg-Richter exponent
P	Cumulative probability function
p	Probability density
A_a	The apparent area of contact
A_r	The real area of contact
K	Material parameter for elastic contact
p_m	Yield pressure of material
p_S	Shear strength of material
R	Radius of adhering sphere
v	Sliding speed
k_1	Spring constant of the nylon string
k_2	Total spring constant of the gripping fibers
k_2'	Combined spring constant
k_3	Effective spring constant for strain gauge, slider and platform
x_1	The elongation of the nylon string
x_3	Deflection of the strain gauge
x	Position of the slider on the platform, page 37
x^*	Characteristic event scale of the system 68
a	Exponent setting the "sharpness" of the cutoff effect 68
$\ddot{x}$	Accelleration of the platform relative to the ground, page 37
v	Pulling speed

v^*	The velocity for which velocity strengthening occur
D_0	characteristic slding length for which all contacts have been renewed
t	time
f	frequency
ΔL	Change of length in the conductor(strain gauge)
R	Resistance of the conductor in strain gauge
$V_{out/in}$	Voltage in and out of the strain gauge
k	Boltzmann constant
T	Temperature
ΔT	Quiet-time allowed between pulses in order to merge into one event (page 51)
r_{line}	Thickness of the elastic string
$G(x)$	suitable scaling function
$\dot{n}$	Average time between events
E	Energy stored in an elastic string
F_c	The pulling force required for an event to be triggered
K	spring constant for measuring device in Figure 4.21
K'	The effective spring constant of the pulling string in the experiments
Δx	Spring elongation in measuring device in Figure 4.21
A	Amplitude of ground motion measured with seismograph (page 148)
T	dominant wave period from earthquake (page 148)
M_S	Seismic magnitude
M_0	Seismic moment

Greek

μ	coefficient of friction (dynamic)
μ_s	The (static) coefficient of friction at the onset of sliding
μ_k	The coefficient of friction while sliding (dynamic)
ε	Surface energy in connection with adhesion theory
β	Exponent event the magnitude probability density
α	Exponent in cumulative event magnitude distribution
τ	Exponent in event duration time probability density
ι	Exponent in event duration time CDF
κ	Power-law exponent for describing the relation between event magnitude and event duration time
φ	Exponent for describing the power-spectrum in SOC systems
δ	Scaling exponent for the joint distribution of event magnitudes and duration time
α	Material parameter – adhering properties of material (page 11)
ϵ	strain
σ	Slope of F(t) – elasticity in the pulling system
Δf	noise bandwidth
ϕ	Examples of critical exponents describing the scaling of the distribution function

Abbreviations, SCM-model paramters and description of experimental components

Table A.1: Abbreviations used in the text

Abbr.	Description
SSM	Stick-slip motion
SCM	Stick-creep motion
CDF	Cumulative distribution function
PDF	Probability density function
SOC	Self-organized criticality
FSE	Finite Size Effects

Table A.2: SSM and SCM - model parameters and variables

Variable	Description
ϵ	Strain in fiber.
ϵ_{th}	Strain threshold in fiber.
N_g	Number of gripping fibers.
ν	Strain update in each macro timestep.
υ	The fraction of strain that is distributed to the other fibers.
$F(t_n)$	Force on the slider in time step n.
$v(t_n)$	Velocity of the slider.
$N_{\text{grip}}(t_n)$	Number of springs that are attached.
$x_i(t_n)$	Amount by which spring i is stretched from equilibrium length.
x_{nl}	Amount nylon string is initially stretched from equilibrium length.
F_{fr}	Constant microscopic friction force.
N_{hs}	Number of asperities that may be attached at a given time.
p_{grip}	Constant probability in time that a single spring becomes attached.
k_{hs}	Spring constant of the hooked springs.
k_{nl}	Spring constant of the nylon string.
$\delta x_{\max}$	Maximum displacement length of hooked springs before snapping.
L	Characteristic length of the system
δt	Constant time-step size.
m	Mass of the slider.

Table A.3: Details about the components in the experimental setup

Component	Description	Details
LCL-010	Strain gauge	Obtained from Omega, costs about 60$
Metrix AX322	Power supply	
Keithley 2002	Multimeter	Keithley instruments

Appendix B

Explorations in sampling from a power law distribution

In this section we investigate how the shape of a measured power law distribution is influenced by sample size (number of events) and the presence of a limiting magnitude (which might for example be the consequence of a finite-size effect). We discuss some simple calculations that involve sampling random numbers from a power law distribution. These calculations demonstrate under what conditions it is possible to infer accurately the limiting magnitude cutoff (that is, the largest magnitude) from distributions of measured event magnitudes in the Feder-Feder experiment.[1]

Sampling from a power-law

A power law distribution can be sampled using a random number generator for a uniform probability distribution [46]. Let R represent a random number chosen from such a distribution, on the interval from 0 to 1. Let us assume a power law density function that has the form x^{-b} for $b > 1$. In order to populate a *cumulative* distribution of the form x^{1-b} with N points, we must find values of x for N different values of R. These values for x are thus obtained from the equation:

$$x(R) = ((R_2 - R_1)R + R_1)^{\frac{-1}{b-1}} . \tag{B.1}$$

where $R_2 > R_1$ and $x_{\min} \equiv R_2^{\frac{-1}{b-1}}$ and $x_{\max} \equiv R_1^{\frac{-1}{b-1}}$ are the smallest and largest magnitudes in the desired distribution, respectively (see Figure B.4). First we set $R_1 = 0$ (that is, $x_{max} \to \infty$) and plot the cumulative distribution for different values of N, where $b = \frac{3}{2}$ (see Figure B.1). It is clear from these plots that there

[1] We have later learnt, and confirmed, that the results we have found in this section are very well described by a "branch" of statistics called "Order statistics".

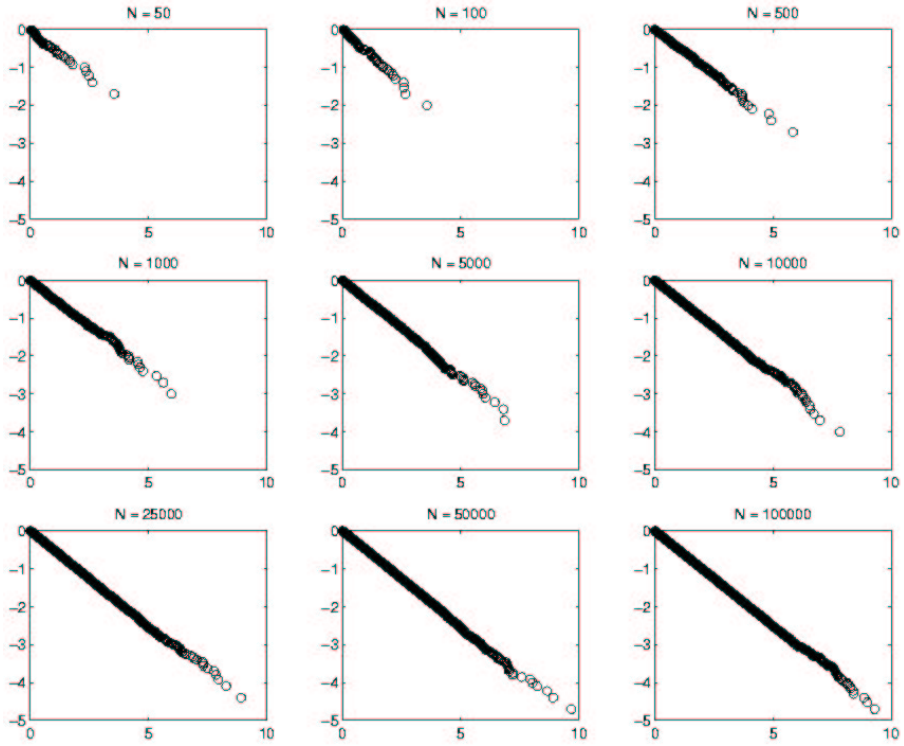

Figure B.1: Sampled cumulative distributions (loglog scale on axis) with no high-magnitude cutoff imposed, for different values of the sample size N.

is no obvious transition to a different behavior in the high-magnitude regime. Instead, the distribution extends in a straight line as the value of N increases (with some noise amid the highest magnitudes).

In reality there is always a high-magnitude cutoff that "feels" the size of the system. That is, in the real world $R_1 > 0$ and $x_{\max}$ is finite. We are interested to find the difference between a measured cutoff (the largest value obtained) and the imposed high-magnitude cutoff $x_{\max}$ for different values of $x_{\max}$ and N. We have plotted these distributions for different values of N and $x_{\max}$ (Figures B.2 and B.3). There is an obvious change in behavior in the vicinity of $x_{\max}$. The value of x at which there is a departure from power law behavior approaches the high-magnitude cutoff as N increases and $x_{\max}$ decreases.

It is clear (and not surprising) that the difference between a measured cutoff and $x_{\max}$ diminishes with increasing N and increases with increasing $x_{\max}$. In order to examine the competition between these two effects, we have also plotted the distribution in measured cut-offs for 10^4 generated distributions, for different values of N and $x_{\max}$. These distributions in measured cutoffs are plotted

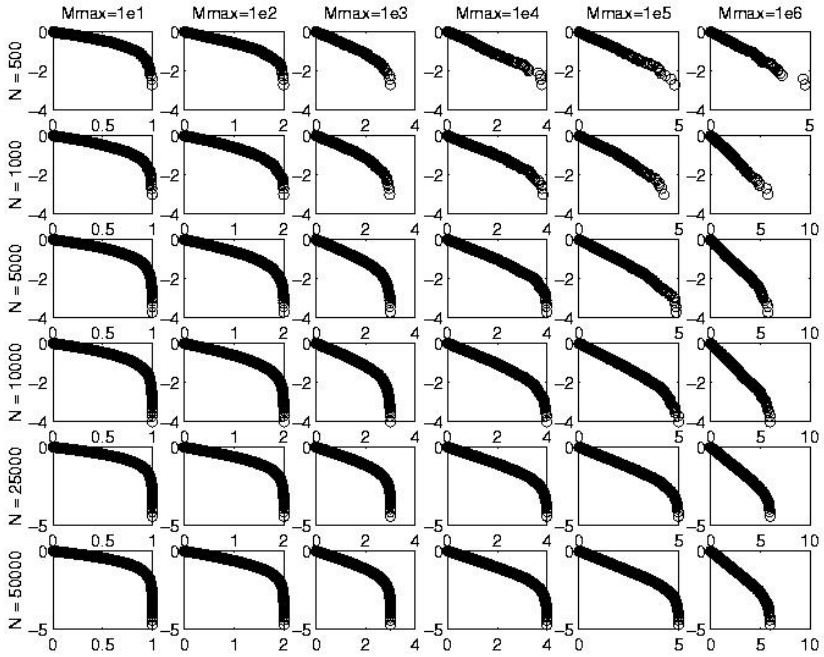

Figure B.2: Sampled distributions with a high-magnitude cutoff imposed, for different values of the sample size N and the cutoff $x_{\max}$. (In this figure, $x_{\max}$ is represented by Mmax.) The axes have been rescaled according to the total domain and range in each set of values.

as histograms in Figure B.5. From this we can see that the center of the distribution for measured cutoffs shifts from the low- to the high-magnitude regime for increasing N and constant $x_{\max}$, and this trend is reversed for constant N and increasing $x_{\max}$.

In Figure B.6 we have plotted these distributions for the range in N and $x_{\max}$ that is relevant to measurements obtained for the Feder-Feder experiment. In that case, an experiment of average duration will have about $N = 40,000$ events and the event magnitudes will span a range from about 10^{-8} to 10^{-2} (which is the corresponding range we expect event magnitudes be in). In this regime, the distribution in measured cutoffs is centered in the high-magnitude region, meaning that we can accurately estimate the high-magnitude cutoff, as well as the error of our estimate. For example, the error for a measured high-magnitude cutoff where $N = 10,000$ and $x_{\max} = 10$ mV is about 2 mV.

These sampling calculations do not take into consideration and cannot account for the presence of a finite-size effect, which is purely physical. That is, in these calculations there is no crossover length at which the probability density function makes the transition from power law behavior to exponential decay.

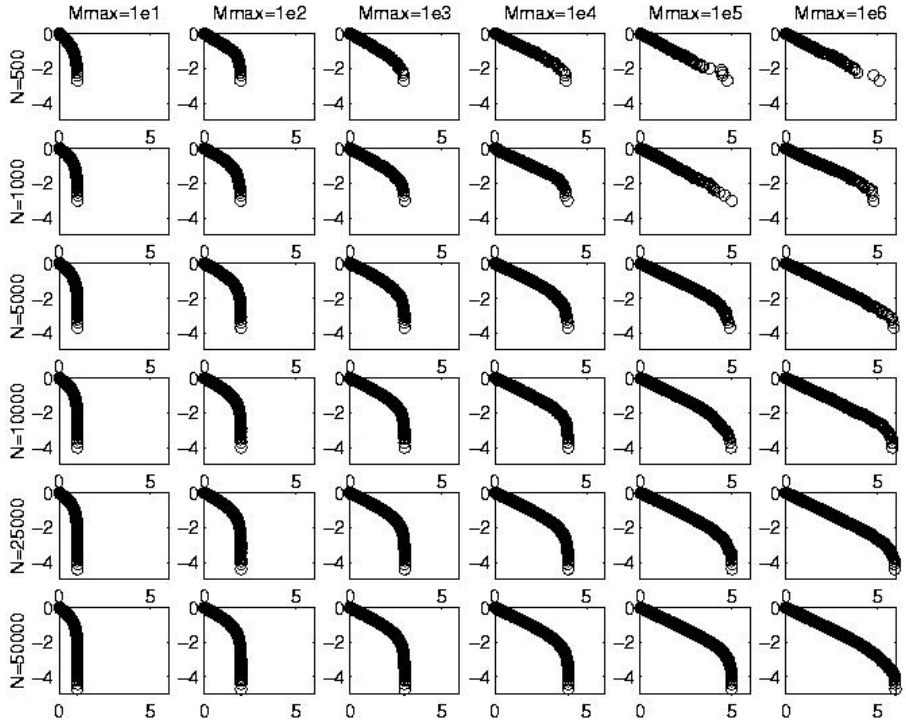

Figure B.3: Sampled distributions with a high-magnitude cutoff imposed, for different values of the sample size N and the cutoff $x_{\max}$. (In this figure, $x_{\max}$ is represented by Mmax.) The same axis scale has been used in each case.

Therefore, the conclusions drawn from this discussion are strictly valid only in the case where the crossover length (that is, crossover magnitude) is very close to the magnitude cutoff.

Analytical result of the high magnitude cutoff

The aforementioned trend in N and $x_{\max}$ can be anticipated by a simple analytical result. If we impose a high-magnitude cutoff $x_{\max}$ then the cumulative probability function $P(X > x)$, which gives the probability that a sampled value X exceeds x, is given by:

$$\begin{aligned} P(X > x) &= (x^{1-b} - x_{\max}^{1-b}) \\ \text{where} \quad x &\in [x_0, x_{\max}] \\ \text{and} \quad x_0 &\equiv (1 + x_{\max}^{1-b})^{\frac{1}{1-b}} \\ \text{so that} \quad P(X > x_0) &= 1 \\ \text{and} \quad P(X > x_{\max}) &= 0. \end{aligned} \tag{B.2}$$

The probability that $N-1$ sampled points are *less than* x is given by:

$$P(\max(\{X_0, X_1, ...X_{N-1}\}) < x) = (1 - P(X > x))^{N-1}. \tag{B.3}$$

The probability density function $p_{\max}(x)$ for the probability that in N sampled points there is just one value that exceeds x is then given by:

$$\begin{aligned} p_{\max}(x) &\equiv \alpha^{-1} p_0(x), \\ \text{where} \quad p_0(x) &\equiv P(X > x)\,(1 - P(X > x))^{N-1} \\ &= \left(x^{1-b} - x_{\max}\right)\left(1 + x_{\max}^{1-b} - x^{1-b}\right)^{N-1}, \end{aligned} \tag{B.4}$$

where α is a normalization constant,

$$\alpha \equiv \int_{x_0}^{x_{\max}} p_0(x)dx. \tag{B.5}$$

The function $p_0(x)$ is plotted in Figure B.7 for several values of N and $x_{\max}$. The trends observed in Figure B.5 are apparent in these plots also. If we do not impose a cutoff then the cumulative distribution function $P^*(X > x)$ is just:

$$P^*(X > x) = x^{(1-b)} \tag{B.6}$$

$$\begin{aligned} \text{where} \quad x &\in [1, \infty) \\ \text{so that} \quad P^*(X > 1) &= 1 \\ \text{and} \quad \lim_{x \to \infty} P^*(X > x) &= 0. \end{aligned} \tag{B.7}$$

The unnormalized probability density function $p_0^*(x)$ corresponding to $p_0(x)$ is given by:

$$p_0^*(x) = x^{1-b}(1 - x^{1-b})^{N-1} \tag{B.8}$$

It can be seen in Figure B.8 that this expression produces a trend in N that is similar to what is found in the former case for p_0.

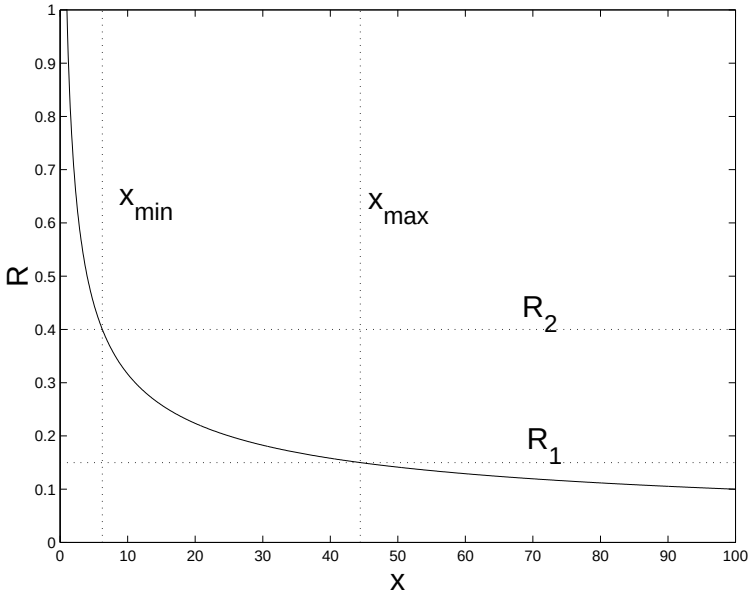

Figure B.4: Cumulative distribution (solid line) and the bounds R_1 and R_2 imposed upon R, and the resulting bounds $x_{\min}$ and $x_{\max}$ of x.

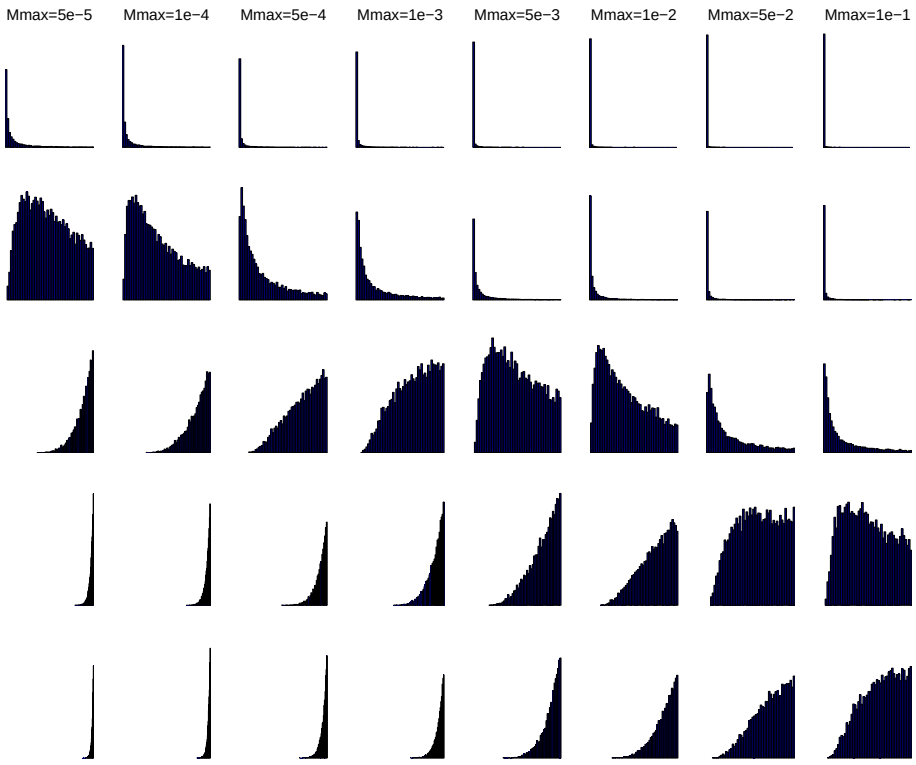

Figure B.5: Histogram distributions of the measured high-magnitude cutoff for different values of $x_{\max}$ (displayed as Mmax) and different values of N. From top to bottom, the calculations in each row were generated using sample sizes $N = 10, 100, 1000, 5000,$ and 10000, respectively.

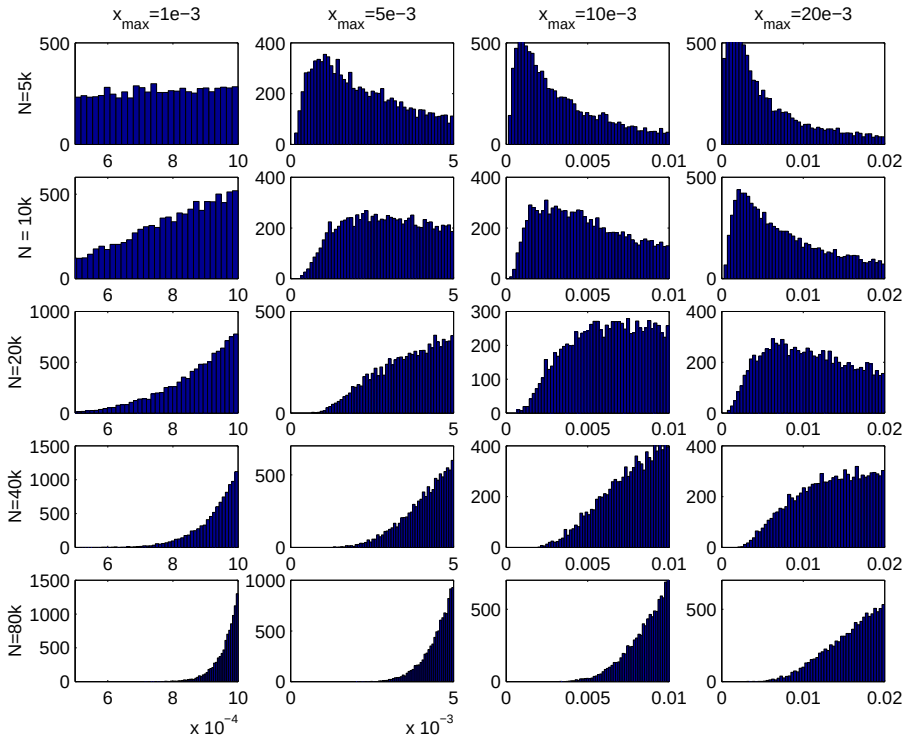

Figure B.6: Histogram distributions of the measured high-magnitude cutoff for different values of $x_{\max}$ and different values of N, in the range relevant for the Feder-Feder experiment.

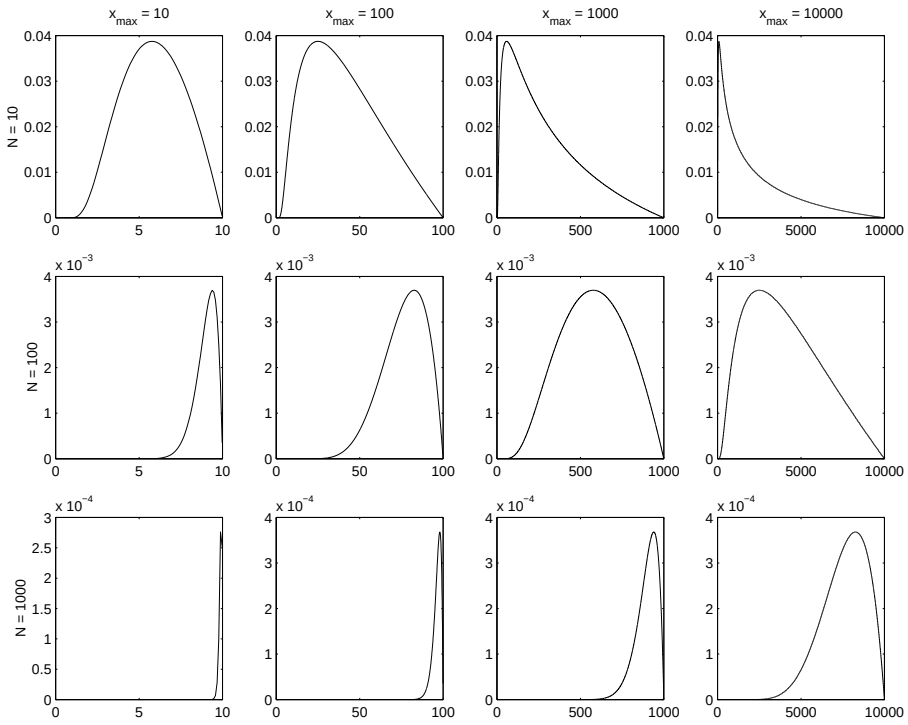

Figure B.7: Plots of equation (B.4) for $p_0(x)$. The trends observed in Figure B.5 are apparent here also.

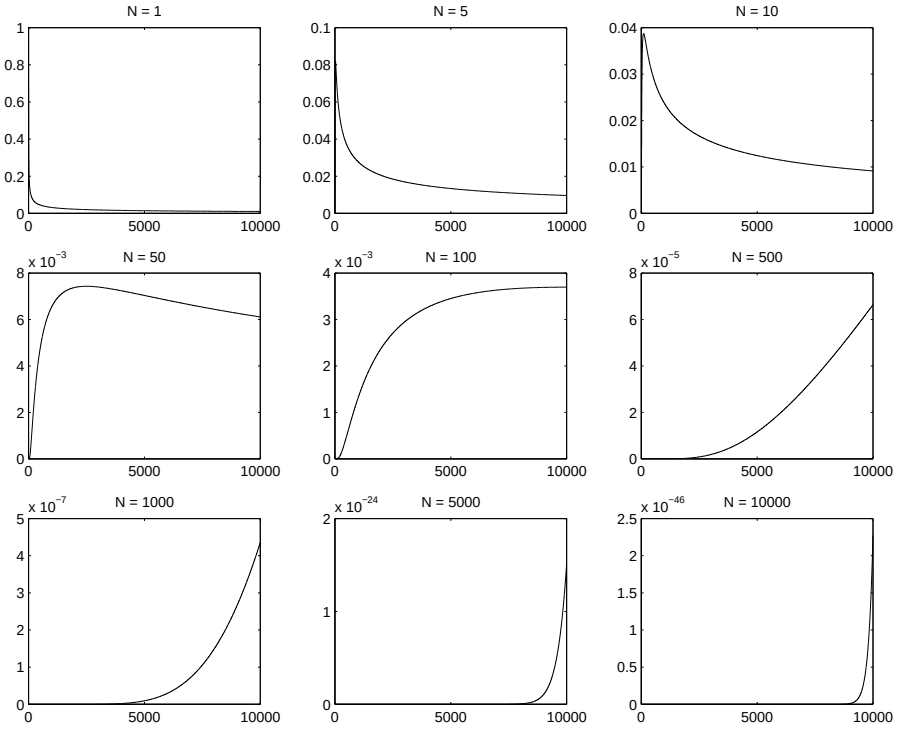

Figure B.8: Plots of equation (B.8) for $p_0^*(x)$. The trend in N observed in Figures B.5 and B.7 is apparent here also.

Appendix C

Calculation of the output voltage in the strain gauge

Equation 3.3 can be found by using the basic rules of electromagnetism. All variables refer to figure 3.9. We know that the voltage drop from A to C is,

$$V_{in} = V_{ABC} = V_{ADC} \Rightarrow I_{ABC}(R_2 + R_1) = I_{ADC}(R_3 + R_4). \tag{C.1}$$

From Ohm's law we have that:

$$V_{AB} = R_2 I_{ABC} \quad = \quad R_2 \frac{V_{in}}{R_1 + R_2} \tag{C.2}$$

$$V_{AD} = R_3 I_{ADC} \quad = \quad R_3 \frac{V_{in}}{R_3 + R_4}. \tag{C.3}$$

The voltage drop across any closed path in the circuit equals 0 (known as Kirchhoff's second rule):

$$V_{out} = V_{AB} - V_{AD} = V_{in} \frac{R_2 R_4 - R_1 R_3}{(R_1 + R_2)(R_3 + R_4)} = V_{in} \left[\frac{R_2}{R_1 + R_2} - \frac{R_3}{R_3 + R_4} \right] \tag{C.4}$$

which is the same as equation 3.3. In the experiments we look at changes in the resistances of the gauges. Suppose we measure a change ΔV_{out}. That is:

$$V_{out} + \Delta V_{out} = V_{in} \frac{(R_2 + \Delta R_2)(R_4 + \Delta R_4) - (R_1 + \Delta R_1)(R_3 + \Delta R_3)}{(R_1 + \Delta R_1 + R_2 + \Delta R_2)(R_3 + \Delta R_3 + R_4 + \Delta R_4)} \tag{C.5}$$

To find out how the change in V_{out} depends on the change in resistances, we set $V_{out} = 0$ in equation C.4 and find that

$$R_2 R_4 = R_1 R_3 \Rightarrow \frac{R_2}{R_3} = \frac{R_1}{R_4} = r \tag{C.6}$$

This can further be used to simplify equation C.4 (when $V_{out} = 0$) and we get

$$\Delta V_{out} = \frac{r}{(1 + r)^2} \left[\frac{\Delta R_1}{R_1} - \frac{\Delta R_2}{R_2} + \frac{\Delta R_3}{R_3} - \frac{\Delta R_4}{R_4} \right] (1 + \nu) V_{in} \tag{C.7}$$

where

$$\nu = \frac{1}{1 + \frac{1+r}{\Delta R_1/R_1 + \Delta R_4/R_4 + r(\Delta R_2/R_2 + \Delta R_3/R_3)}} \tag{C.8}$$

When the resistance changes are small ($< 5\%$) the value of ν is approximately 0 and can be ignored. Equation C.7 can be simplified by assuming that the resistances have almost equal values that is $R_1 \sim R_2 \sim R_3 \sim R_4 = R$, and we can write $r \sim 1$. This finally gives us a practically looking answer for the change in V_{out} when there is a change in the variable resistances.:

$$\Delta V_{out} \sim \frac{\Delta R_1 - \Delta R_2 + \Delta R_3 - \Delta R_4}{R} V_{in} \tag{C.9}$$

From this equation we see that if for example R_1 and R_3 are in compression (positive Δ), and R_2 and R_4 are in tension (negative Δ) the total change in V_{out} is proportional to the sum of all the strains measured separately. Since the gauges are very sensitive to changes in temperature the Wheatstone bridge acts as temperature compensater as well as an amplifier for small changes in the resistances.

Appendix D

The Periodogram method for calculating the power spectrum

By inspecting the power spectrum of the signal it is possible to learn something about the temporal correlations in the signal, and therefore a much used tool in signal analysis. The power spectrum, or power spectral density, of a function $c(t)$ can be estimated by taking the modulus-squared of the Fourier transform of the function. This is basically the same thing that is done in the periodogram method we have used, but some attention will be focused on the details. The periodogram method goes as follows. We pick out a sample of N-points ($c_i, ..., c_N$) ,at equal intervals from $c(t)$, and use the FFT (fast Fourier transform) to obtain the Fourier coefficients:

$$C_k = \sum_{j=0}^{N-1} c_j e^{2\Pi ijk/N}, k = 0, ..., N-1 \tag{D.1}$$

Note that the coefficients C_k are periodic in k, with period N. This means that $C_{-k} = C_{N-k}$ for $n = 1, 2, ...$ See [44] for more information about the FFT. The periodogram estimate ($P(f_k)$) of the power spectrum is defined at $N/2+1$ frequencies as:

$$P(0) = P(f_0) = \frac{1}{N^2}|C_0|^2 \tag{D.2}$$

$$P(f_k) = \frac{1}{N^2}(|C_k|^2 + |C_{N-k}|^2), k = 1, 2, ..., (N/2-1) \tag{D.3}$$

$$P(f_c) = P(f_{N/2}) = \frac{1}{N^2}|C_{N/2}|^2 \tag{D.4}$$

Equation D.2 is normalized so that the sum of the $N/2+1$ values of P is equal to the mean squared amplitude of the signal $c(t)$ (see [44] for details). The

frequencies f_k are defined only for the positive values

$$f_k \equiv \frac{k}{N\Delta} = 2f_c\frac{k}{N}, k = 0, 1, ..., N/2 \tag{D.5}$$

where Δ is the number of samples recorded per second, and f_c is the Nyquist frequency given by $f_c \equiv \frac{1}{2\Delta}$. If the signal $c(t)$ is not bandwidth limited to less than f_c, it turns out that all of the power spectral density outside f_c is moved into to the frequency range D.5. This effect is called aliasing, and is hard to do anything with once you have sampled the signal. One way to find out to what degree aliasing has happened is to see whether the Fourier transform approaches 0 when the frequencies approach f_c. If the Fourier transform closes in on some finite value for frequencies near f_c can we assume that frequencies outside f_c has been folded back over into the critical range of frequencies. The variance of the PSD at a given f_k ,calculated using the described periodogram method, is always equal to the square of the expectation value at that frequency. This means that the standard deviation is always 100% of the PSD value, independent of the number of sampled points N. One way to reduce the standard deviation is to split the signal into K segments of contiguous sample points, and FFT each separate segment. Say we want M discrete frequencies in the range 0 to f_c, then the segments should each contain $2M$ points. The power spectrum is then found for each segment using D.2, and finally the segments are averaged at each frequency. This procedure reduces the standard deviation by $\sqrt{K}$, and makes the calculation of the power spectrum faster since it's more efficient to take many short FFT's than one big. The number of sample points, M , should be a power of two, because this increase the speed of the FFT algorithm a great deal.

Appendix E

The seismic magnitude and moment

The surface-wave magnitude caused by an earthquake, M_S (measured with a seismograph), is given by

$$M_S \sim log_{10}(\frac{A}{T}) \ , \tag{E.1}$$

where A(μm) is the amplitude of ground motion, and T (s) is the dominant wave period. The ratio A/T is a measure of the strain amplitude in a seismic wave, while the flux of elastic energy passing any point is proportional to its square. By integrating complete seismic waveforms, an empirical relationship between magnitude and energy, E (joules), is obtained [18]:

$$M_S \sim log_{10}(E) = 1.44M_S + 5.24 \ , \tag{E.2}$$

For very large earthquakes ($M_S > \ 8$), the M_S scale saturates and does not discriminate between different earthquakes. Another measure for characterizing earthquakes has therefore been introduced, namely the *seismic moment*, M_0:

$$M_0 = \int_A \mu S da \simeq \mu \bar{S} A \ (joules) \ , \tag{E.3}$$

where μ is the shear modulus of the faulted medium, and $\bar{S}$ is the average slip across a fault area A. A revised scale for magnitudes, based on the seismic moment, has been developed,

$$M_0 = 0.69 log_{10}(M_S) - 6.4 \ . \tag{E.4}$$

Appendix F

Autocorrelation function, power spectra and 1/f noise

Some signals occurring in nature, and in laboratories, show in their frequency domain very similar behaviors called "1/f noise". The term arises due to the fact that by looking at the absolute squared of the signal Fourier-transformed, called the power spectrum or spectral density, the frequencies will distribute themselves approximately as $f^{-\varphi}$ where the value of φ normally takes a value between 1 and 2. Signals first shown to exhibit this kind of behavior were sampled in the context of studying current fluctuations of electronic emission in a thermionic tube (1925), therefore the term "1/f noise". Another term also used is "flicker noise". Later the same type of current spectrum was also found in carbon microphones, various semiconductor devices and superconductors. For many classes of conductors the properties of "1/f noise" is known, but the problem in general can be said to be considerably unsolved. Other systems in nature which shows "1/f noise" are for example sunspot activity, the flow of rivers, total activity in sandpiles, turbulence, and friction [55]. Some of the mentioned systems also exhibit, in addition to scaling in time (1/f noise), scaling in space. This spatio-temporal scaling behavior has been proposed as a condition for self-organized criticality (SOC), but this has been hotly debated [56, 28].

What makes the power spectrum such a useful tool in studying what seem to be random signals, is its connection to the autocorrelation function. The autocorrelation function is given by:

$$G(\tau) = \langle N(\tau_0)N(\tau_0+\tau)\rangle_{\tau_0} - \langle N(\tau_0)\rangle^2_{\tau_0}, \tag{F.1}$$

where $N(\tau)$ is the value of the signal at time τ and the square brackets means the average is taken over all τ_0s. The power spectrum of the signal is given by:

$$S(f) = \lim_{T\to\infty} \frac{1}{2T}\left|\int_{-T}^{T} d\tau N(\tau)e^{2i\pi f\tau}\right|, \tag{F.2}$$

and this is related to the autocorrelation function through the Wiener-Khintchine theorem:

$$S(f) = 2\int_0^\infty d\tau G(\tau)\cos(2\pi f\tau). \tag{F.3}$$

If we assume that $S(f) \sim f^{-\varphi}$ and $G(\tau) \sim \tau^{-\beta}$ it follows from (F.3) that $\varphi \sim 1-\beta$. When we observe a power spectrum with φ close to 1, it means that $G(\tau)$ decays very slowly, almost logarithmic. This again means that there exist long time correlations in the signal for which the power spectrum has a slope close to unity. As a general rule it can be said that the temporal correlation in the signal decreases with increasing φ. What may be the causes that "$1/f^\varphi$ noise" shows up in many different natural phenomena? It can be shown that a 1/f power spectrum can be constructed by superimposing weighted Poisson processes [6]. That is, assuming we know the functional form of the individual correlation functions for the different processes, and the probability density of the correlation times, we get:

$$S(f) = \int_0^\infty d\tau_0 S_{\tau_0}(f)P(\tau_0), \tag{F.4}$$

where,

$$S_{\tau_0}(f) = \frac{4A\tau_0}{1+(2\pi f\tau_0)^2} \sim \lim_{\tau\to f_c}\frac{1}{1+(\frac{f}{f_c})^2} \tag{F.5}$$

is the power spectrum (F.2) of the individual correlation functions that make up the signal:

$$G(\tau_0) = Ce^{-\frac{\tau}{\tau_0}}. \tag{F.6}$$

The density of the correlation times $P(\tau_0)$ must be formed in a rather ad hoc way to produce a power spectrum S(f) with $\varphi \sim 1$. In the case of sandpiles where grains added cause avalanches, we can construct time profiles $f_{A_i}(\tau)$ of how many sites are toppled (dissipation rate) at time step τ for the individual avalanches of type A_i, and say that the total activity in the sandpile ($J(\tau)$) is a super-position of all time profiles randomly started:

$$J(\tau) = \sum_{\tau_i<\tau} f_{A_i}(\tau-\tau_i) \tag{F.7}$$

In the spirit of equation (F.4), we can construct the power spectrum of J:

$$S_J(f) = \frac{C}{f^2}\int_0^\infty d\tau L(\tau)sin^2(f\tau\pi) \sim \frac{C}{f^2}\int_0^\infty d\tau e^{-\frac{\tau}{\tau_0}}\tau^a sin^2(f\tau\pi) \tag{F.8}$$

and using the distribution of avalanche lifetimes $L(\tau)$. This will give a power spectrum:

$$S_J(f) \sim \begin{cases} f^{-(3+a)} & : \quad a<-1 \\ f^{-2} & : \quad a>-1 \end{cases} \tag{F.9}$$

In (F.7) it is required that all the avalanches are statistically independent. Questions can be raised as to whether this is the case in a real sandpile (or in the

carpet experiment). Even though we in our experiments observe a power spectrum $S(f) \sim f^{-\varphi}$ with $\varphi \sim 2$ (see figure F.1), it is dangerous to make an analogy between the carpet experiment and sandpiles, and with a super-position of randomly-started and uncorrelated Poisson processes.

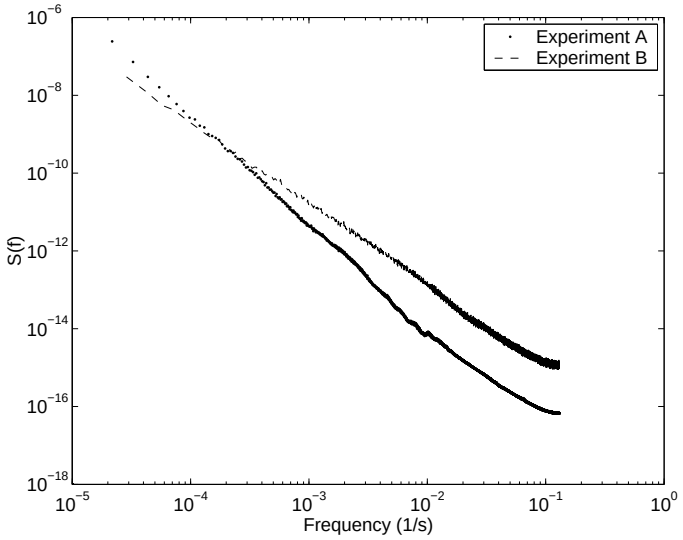

Figure F.1: The power spectrum calculated for experiment A and B, using the Periodogram method with 50 frequencies averaged in each bin. The plots resembles power-laws and a linear regression over the log-log linear region yields $\varphi = 2.8$ for experiment A, and $\varphi \sim 2.0$ for experiment B.

There is an abundance of systems showing $1/f^{\varphi}$ with $\varphi > 2$ in their power spectrum, and in many of these cases the behavior can be ascribed to a high frequency limit of some Poisson process as in (F.6), and with a spectrum as described in equation (F.5). Despite the heavily debated correlation between SOC systems and an observed power-law in the power-spectrum we have chosen to not discuss the issue in this thesis.

Appendix G

Source code for the SSM model

```
% qarr_ver2.m -- Quake Arrest, version 2.0
%                 For Matlab version 5.3
%
% A model for arresting quake events in stick-slip motion.
% Version 2, for the looped-fiber and sandpaper system.
% Microscopic friction is added as a constant term.
%
% W.A. Watters Farfan & Haakon Nordhagen.
% 6 juin 2001
%
% ---- Generating the asperities list ---------------------------------------

for j = 1: N_asp,

   Asps(j) = 0;

end

% ---- Primary loop ---------------------------------------------------------

while del_x > 0 ,  % i.e., Continue as long as the slider is moving.

  del_v =  (1/m) * F_total * del_t;

  v_total = v_total + del_v;
  v_vals(t) = v_total;

  del_x =  v_total * del_t;  % Finds del_x based on v_total
                             % from current timestep.
```

```
  x_total = x_total + del_x;
  x_vals(t) = x_total;

%.... Calculation of N(t), managing asperities
.............................

  N = 0;
      total_fiber_force = 0;
      for j = 1: N_asp,
          if Asps(j) == 0
          p = rand(1,1);
              if p > (1-prob_grip)
                Asps(j) = Asps(j) + del_x;
              end
          else
      Asps(j) = Asps(j) + del_x;
              if Asps(j) > max_strain;
                 Asps(j) = 0;
              end
          end
  if Asps(j) > 0
     total_fiber_force = total_fiber_force + kf*Asps(j);
             N = N + 1;
          end
      end

% .... Updating changes in total force
.....................................

  x_fromequil = x_fromequil - del_x;
  F_total = ks * x_fromequil - total_fiber_force - F_fr;
  F_vals(t) = F_total;

  if x_fromequil > 0
     onoff = 1;
  else
     onoff = 0;
     if N == 0
        F_total = 0;
        if terminate_when_relaxed == 1
            fprintf(1,'\n\nDriving force has relaxed totally!\n\n');
            pause;
        end
     end
  end

  N_vals(t) = N;

  t = t + 1;
  total_time = t*del_t;
```

```
end   % End of quake-arresting program


%-------------------------------------------------------------------------
%
%
% Modular script that contains input parameter settings to qarr_ver2.m
% W.A. Watters Farfan and H. O. Nordhagen
% 13 juin, 2001
%
%
%----- Global parameters
-----------------------------------------------------

debug = 0;                    % Whether debug mode is engaged (1 if yes)
prob_grip = 0.00005;          % Probability of inidividual asperities
gripping;

del_t = 0.0001;               % Timestep size
m = 0.0001;                   % Mass of slider

max_strain = 0.05;            % Maximum strain allowed before slip of
                              % individual asperities.

ks = 0.5;                     % String/strain gauge combined spring
constant.
kf = 100;                     % Asperity spring constant.

terminate_when_relaxed = 1;   % Terminate when the string relaxes totally if
1.
N_asp = 20;                   % Total number of asperities that can grip.

% ---- Initial conditions
-------------------------------------------------

N = 0;                        % Initial number of gripping asperities
(zero).
t = 1;                        % Initial value of timestep counter.
F_total = 6;                  % Total force counter (initial value gives
      % initial total force value).
F_fr = 5;                     % Constant friction force.
v_total = 0;                  % Initial velocity (zero).
x_total = 0;                  % Initial displacement (zero).
del_x = 100000000;            % Changed immediately after loop is entered.

x_fromequil = F_total / ks;   % Distance from equilibrium position of
string.
F_total = F_total - F_fr;     % Subtracting the constant friction force.
```

```
% ---- Vector initializations
------------------------------------------------

F_vals = [];
x_vals = [];
v_vals = [];
N_vals = [];
```

Appendix H

Source code for the SCM model

```
/*
* NW_model.c  ver4 (with variable asperity strain thresholds and different
* gripping probabilities for macro and micro time steps), and conservation
* of overstrain on/off.
*
* Module containing function definitions for use in NW_model.c,
* Haakon Nordhagen and Wesley Andres Watters Farfan, juin 2001
*
*/
#include <stdio.h>
#include <stdlib.h>
#include <math.h>
#include "lib.h"

/* first argument to main should be the input file */
int main (int argc, char *argv[])
{
  /* Variables ************************************************** */


  double new_num;

  /* Local variables */

  int i, j, k, count4shrink = 0;
  int asp_num,TOTAL_TIME,wait_time;
  long start_time;

  int is_slip, is_quake, is_creep = 0,num_slips, new_num_slips,
asp_num_gripping, is_first;
```

```
  double total_strain, chosen_num, strain_redist, new_strain,
strain_threshold;
  double last_total_strain, peakval, bottval;



  /* Variables that will be passed to this function.
***********************/

  int asp_num_active, start_index, end_index, shrink_factor,
conserve_overstrain;
  double max_strain_threshold, fraction_redist, strain_update, p_grip_micro,
p_grip_macro;
  double  P_GRIP, MAX_INIT_STRAIN;
  double max_init_strain_macro,max_init_strain_micro;
  long idum; /* Random number generator */

  double **asp_list; /* Contains the list of the asperities and their
properties */

  char out_filename[50], trial_label[10], file_mags[50];

  FILE *force_out, *params_in, *mags_outfile; /* in-out files

  /* End variables
********************************************************** */

  /* Opening and reading in the parameters from filename given at command
line */
  if((params_in = fopen(argv[1],"r")) == NULL) {
    printf("Cannot open output file for writing.\n");
    exit(1);
  }

  fscanf(params_in,"%*s %s\n",&trial_label);  /* The experiment number */
  fscanf(params_in,"%*s %lf\n",&fraction_redist); /* How much is conserved
when one snaps */
  fscanf(params_in,"%*s %lf\n",&strain_update); /*The speed, or strain
update in macrotimesteps */
  fscanf(params_in,"%*s %lf\n",&max_strain_threshold);/* the max. strain
before springs snap */
  fscanf(params_in,"%*s %d\n",&asp_num); /* Number of active,possibly
gripping sites */
  fscanf(params_in,"%*s %lf\n",&P_GRIP); /* prob. of gripping at initial
conditions */
  fscanf(params_in,"%*s %lf\n",&p_grip_micro); /* prob. of gripping in micro
timestep */
  fscanf(params_in,"%*s %lf\n",&p_grip_macro); /* prob. of gripping in macro
timestep */
  fscanf(params_in,"%*s %lf\n",&MAX_INIT_STRAIN); /*% of The maximum strain
```

```
at initial cond. */
  fscanf(params_in,"%*s %lf\n",&max_init_strain_micro);/*% of max strain
assigned asperity in mts */
  fscanf(params_in,"%*s %lf\n",&max_init_strain_macro);/*% of max strain
assigned asperity in mats*/
  fscanf(params_in,"%*s %d\n",&TOTAL_TIME); /* How many macro timesteps to
run */
  fscanf(params_in,"%*s %d\n",&wait_time); /* How many timesteps to run
before start recording */
  fscanf(params_in,"%*s %ld\n",&idum); /* The random number generator seed
used */
  fscanf(params_in,"%*s %d\n",&shrink_factor); /* how many times to shrink
the raw signal output */
  fscanf(params_in,"%*s %d\n",&conserve_overstrain);/*if strain on asperity
exceeds its threshold
      conserve the excess strain (1) og do not (0) */
  /* Max_strain_threshold is given in % of MAX_INIT_STRAIN to assign
asperities */
  MAX_INIT_STRAIN = MAX_INIT_STRAIN * max_strain_threshold;

  TOTAL_TIME = TOTAL_TIME + wait_time; /* For initializing system, for the
macro-loop to work  */

  /* asp_list goes as:
     col0 : row_number (unused, no geometry)
     col1 : strain
     col2 : strain_threshold
     col3 : number of connected sites (unused, no geometry)
     */
  asp_list = (double **) matrix(asp_num,4, sizeof(double));


  /* In future, this will be supplied by the movement function*/
  start_index = 0;  /* but now all sites are active */
  end_index  = asp_num - 1;


  /* ***************** Open the magnitude and raw data files  ********** */
  sprintf(file_mags,"magsmod%s",trial_label);

  if((mags_outfile = fopen(file_mags,"w")) == NULL) {
    printf("Cannot open the mags output file for writing.\n");
    exit(1);
  }

  sprintf(out_filename,"slips_mod%s.dta",trial_label);

  if((force_out = fopen(out_filename,"w")) == NULL) {
    printf("Cannot open output file for writing.\n");
    exit(1);
```

```
  }


  /* ****************** First generating the points on the surface for the
initial
   conditions. Every asperity grips with probability P_GRIP and is assigned
a random threshold  */
  for(i = start_index; i <= end_index; i++)
    {
      chosen_num = ran0(&idum);
      if ( chosen_num > (1-P_GRIP)) new_num = ran0(&idum)*MAX_INIT_STRAIN;
      else new_num = 0;
      asp_list[i][0] = 1; /* row number (unused for now) */
      asp_list[i][1] = new_num*ran0(&idum); /* The initial strain */
      asp_list[i][2] = new_num; /* The strain threshold */
      asp_list[i][3] = 0; /* Connected sites (not used) */
    }
  /* ******************** End generating the asp_list for initial
conditions ************** */


/* ---- Start of macro-timestep loop (loop will be eliminated) ---*/
for (j=0; j<TOTAL_TIME ; j++)
   {

     /* ---- Start of macro time-step procedures
-----------------------------------------  */

     is_slip = 0;        /* Switch that indicates a slip event */
     num_slips = 0;      /* Used to count the number of slip events. */
     new_num_slips = 0;  /* Used to count the number of slip-provoked
slips.*/


  /* This loop visits all asperities in the list and counts the number that
are gripping.
     This is needed in order to calculate the strain that must be added to
all gripping
     asperities in the next loop. New asperities that make contact are also
counted */

     asp_num_gripping = 0;

     for(i = start_index; i <= end_index; i++)  /* go through all asperities
*/
       {
 chosen_num = ran0(&idum);

 if ( asp_list[i][1] > 0.0 ) asp_num_gripping++;
```

```
 else if( chosen_num > (1 - p_grip_macro) ) /* give the asperity a chanse
to grip */
   {
     asp_list[i][2] = ran0(&idum)*max_strain_threshold; /*assign random
strain threshold */
     asp_list[i][1] =
ran0(&idum)*asp_list[i][2]*max_init_strain_macro;/*ass rand. strain*/
     asp_num_gripping++;/* count the number of asperities gripping */
   }
       } /* end giving chance to grip for nongripping asperities*/


     /* This for loop visits all asperities in the list and updates their
strains(by strain_update)
        if they are gripping, and checks to see if they have started
gripping otherwise. */
     for (i = start_index; i < end_index + 1; i++) {
       /* If this site is gripping (strain greater than 0), then update the
strain. */
       if (asp_list[i][1] > 0) asp_list[i][1] += ((double) strain_update)/
((double)asp_num_gripping);
       /* Checks to see if we have the beginning of a creep */
       if ( asp_list[i][1] > asp_list[i][2]  ) is_slip = 1;  /*at least one
asperity exceeds thre.*/
     }


     /* --- Commencing updates for micro-timesteps
-----------------------------------
      micro-timestep only run if is_slip == 1, i.e at least one asperity has
exceeded its
     threshold */
     is_quake = 0; /* Switch that indicates a quake event */
     is_first = 1; /* Used in microtimestep as a switch (not important) */

     /* Run until there are no more asperities exceeding their thresholds */
     while( is_quake == 0 && is_slip == 1) /*is_quake used only for SSM
(always == 0) */
       {
 /* The first for loop counts and resets all asperities that have slipped,
    and counts the number that are gripping. The total amount of strain to
be
            redistributed bacuse of slipping asperities is also calculated.
 */
 num_slips = 0;
 is_slip = 0;
 asp_num_gripping = 0;
         strain_redist = 0;

    /*   Go through all asperities (could be more than one asperity which
```

```
has
 slipped. Start_index and end_index stay constant*/
 for(i = start_index; i <=  end_index; i++)
   {
     /* If an asperity is not currently gripping, then find out if it
                 starts gripping now.  If so, then assign to it a random
strain < its threshold.*/

     if (is_first == 0) {  /* Only run this for the first slipping asperity
*/

       if( asp_list[i][1] == 0 ){

 chosen_num = ran0(&idum);
 if ( chosen_num > (1-p_grip_micro))
   {
     asp_list[i][2] = ran0(&idum)*max_strain_threshold;/*Assign random
threshold*/
     asp_list[i][1] =
ran0(&idum)*asp_list[i][2]*max_init_strain_micro;/*strain */
   }
       }
     } /* end of if(is_first) */

     /* If a site exceeds the strain_threshold, then reset and count as
slip.*/
     if (asp_list[i][1] > asp_list[i][2])
       {
 if(conserve_overstrain == 1)    /* What to do with the overstrain ??*/
   strain_redist += asp_list[i][1]; /* distribute the total strain on the
asperity*/
 else strain_redist += asp_list[i][2]; /* or only the asperity threshold
*/
 asp_list[i][1] = 0; /* Asperity is no longer gripping */
 num_slips++; /* for counting slips in this macrotimestep */
       }

     /* Checks if gripping, and counts if that is so. */
     if (asp_list[i][1] > 0) asp_num_gripping++;

   } /* end for counting the redistribution of strain after some have
slipped */

 is_first = 0;

 /* The second loop redistributes the strain calculated in the last for
loop,and decides
             if there are any new slips. */
 for(i = start_index; i < end_index + 1; i++) /* Spread strain on all
gripping asps */
```

```
   {
     if (asp_list[i][1] > 0) /* Is it gripping? */
       {
 /* assign its part of the global perturbation caused by slipping
asperities */
 asp_list[i][1] += ( (double)fraction_redist * (double)strain_redist) /
((double) asp_num_gripping);
                 if (asp_list[i][1] > asp_list[i][2]) is_slip = 1;/*Is this
causeing a new slip ?*/
       }
   } /* for i = ... */
       } /* end (while(is_slip == 1)) of micro time-step */
     /* micro-step continues until is_slip == 0 */
     /* ------- End of micro timestep loop ---------------------------------
*/

     last_total_strain = total_strain; /* used in picking out mags */


     total_strain = 0.0;

     /*  This loop sums the total strain contained in all asperities
         for the current macro time-step */
    for(i = start_index; i < end_index + 1; i++) total_strain +=
asp_list[i][1];

     /* get_mags: Check to see if a decrease in strain is underway */
    if( total_strain < last_total_strain && is_creep == 0) /* An event has
started */
       {
       is_creep = 1;
       start_time = j;
       peakval = last_total_strain;
       bottval = total_strain;
       }
    else if (total_strain <= last_total_strain && is_creep == 1)
       {
 bottval = total_strain;  /* Strain in the system is still decreasing */
       }
    else if (total_strain > last_total_strain && is_creep == 1) /*Are we at
bottom of event ? */
       {
 is_creep = 0; /* total strain is no longer decreasing, all asps are stuck
*/
         /* Print out the calculated magnitude */
 fprintf(mags_outfile,"%.2lf %lf %.2lf %lf %ld %ld\n", (double)j-1, peakval
- bottval, (double)((j-1) - start_time), peakval, j-1,
start_time);
       }
```

```
     /* If the requisite number of counts has passed, then print a line of
"raw" data.
        This is for looking at the "raw" data, and so that this file does
not become too big */
     count4shrink++;
     if (j > wait_time && count4shrink >= shrink_factor) {

         fprintf(force_out,"%.2lf %lf\n",(double)j,total_strain);
         count4shrink = 0;
     }

     /* ------- End of macro timestep procedures --------------------*/
   } /* End of macro timestep for loop */

/* Close all files that has been written to or read from */
fclose(force_out);
fclose(params_in);
fclose(mags_outfile);

} /* End main! ****************************************** */
```

SCM Model parameters used

```
frac_redist=0.940,
%update = 800.0
max_strain_threshold=100000.0
asp_num(number of asperities)=500,
P_GRIP(prob. of regripping at initial
conditions) = 1.0
p_grip_micro(gripping_prob_microstep) = 0.5
p_grip_macro(gripping_prob_macrostep) = 0.1
MAX_INIT_STRAIN(max_start_strain_initial_cond) = 1.0
max_init_strain_micro(fraction_of_threshold) = 0.05
max_init_strain_macro =  0.01
total_time = 500000
wait_time(init_time) = 100000
idum(seed_for_ran0) = -1
shrink_factor = 20
conserve_strain(1=yes,0=no) = 0.
```

Bibliography

[1] D. Dowson. *History of tribology*. Professional Engineering Publishing, 1998.

[2] G. Amontons. *De la resistance causé dans le machines.* Histoire de l'Académie Royale des Sciences avec les Memoires de Mathematique et de Physique, 1699.

[3] F. P. Bowden and D. Tabor. *The friction and lubrication of solids, volume 1 of The international series of monographs in physics*. Clarendon Press, Oxford, 1950.

[4] B. N. J. Persson. *Sliding Friction*. Springer Verlag, 2000.

[5] P. Bak. *How Nature Works*. Cambridge University Press, 1996.

[6] H. J. Jensen. *Self-Organized Criticality*. Cambridge University Press, 2000.

[7] H. J. S. Feder and J. Feder. Self-organized criticality in a stick-slip process. *Phys. Rev. Lett.*, 66:2669, 1991.

[8] E. Bergli. *A Simple Model for the Physics of Surface COntact and Adhesion. Thesis presented for the degree of Candidata Scientiarum*. University of Oslo, 2001.

[9] H. Hertz. Ueber die berührung fester elastischer körper. *Journal für die reine und angewandte Mathematik*, 92:156–171, 1881.

[10] E. Rabinowicz. *Friction and Wear of Materials,Second Edition*. John Wiley & Sons, 1995.

[11] M. M. Koura. The effects of surface parameters on friction. *Wear*, 73:235–246, 1981.

[12] J.A Ogilvy. Numerical simulation of friction between contacting rough surfaces. *J. Phys. D*, 24:2098, 1991.

[13] J. F. Archard. Elastic deformation and laws of friction. *Proceedings of the Royal Society*, A243:190–205, 1957.

[14] E. Tosatti B. N. J. Persson. *Physics of sliding friction*. NATO ASI series E, 1995.

[15] M. Mardar E. Gerde. Friction and fracture. *Nature*, 413:285, 2001.

[16] E. Rabinowicz. The determination of the compatibility of metals through static friction tests. *ASLE Trans.*, 14:198–205, 1971.

[17] J. S. Larsen A. Johansen, P. Dimon. Dynamic phases in a spring-block system. *Phys. Rev. E*, 48(6):4779, 1993.

[18] C. H. Scholz. *The mechanics of Earthquakes and Faulting.* Cambridge University Press, 1990.

[19] E. Rabinowicz. *Proc. Roy. Soc. London*, 371:668, 1958.

[20] T. Baumberger F. Heslot and B. Perrin. Creep, stick-slip, and dry-friction dynamics experiments and a heuristic model. *Phys. Rev. E*, 49:4973, 1994.

[21] P. Nozieres C. Caroli. Dry friction as a hysteretic elastic response. *NATO ASI series E*, 311:27–49, 1995.

[22] G. Grinstein. Scale invariance and self organized criticality. *NATO ASI series B*, 344:261, 1995.

[23] B. Gutenberg and C. F. Richter. *Ann. Geophys. (C.N.R.S)*, 9:1, 1956.

[24] C. Laroche S. Cliberto. Experimental evidence of self-organized criticality in the stick-slip dynamics of two rough elastic surfaces. *J. Phys. I*, 4:223, 1994.

[25] K. Christensen Z. Olami, H. J. S. Feder. Self-organized criticality in a continuous nonconservative cellular automaton modeling earthquakes. *Phys. Rev. Lett.*, 68:1244, 1992.

[26] B. Mandelbrot. *The fractal geometry of nature (updated).* Freeman, 1999.

[27] C. Tang P. Bak and K. Wiesenfeld. Self-organized criticality: An explanation of 1/f noise. *Phys. Rev. Lett.*, 59:381, 1987.

[28] C. Tang P. Bak and K. Wiesenfeld. Self organized criticality. *Phys. Rev. A*, 38:364, 1988.

[29] W .H . Press. Review of 1/f noise in astronomy and elsewhere. *Commun. Mod. Phys*, C7:103, 1978.

[30] J. Feder. *Fractals.* Plenum Press, 1988.

[31] H .E . Stanley. Scaling, universality and renormalization: Three pillars of modern critical phenomena. *Rev. of Modern Physics*, 71:S358, 1999.

[32] V. Frette et al. Avalanche dynamics in a pile of rice. *Nature*, 397:49, 1996.

[33] J. S. Langer J. M. Carlson. Mechanical model of an earthquake fault. *Phys Rev. A*, 40:6470, 1989.

[34] D. Spasojevic et al. Barhausen noise: Elementary signals, power laws, and scaling relations. *Phys. Rev. E*, 54:2531, 1996.

[35] J. Pitt S. Field. Superconducting vortex avalanches. *Phys. Rev. Lett.*, 74:1206, 1995.

[36] H. E. Stanley S. Zapperi, A. Vespignani. Plasticity and avalanche behaviour in microfracturing phenomena. *Nature*, 388:658, 1997.

[37] H. E. Stanley B. Suki. Avalanches and power-law behavior in lung inflation. *Nature*, 368:615, 1994.

[38] S. Zapperi A. Vespignani. How self-organized criticality really works: A unified mean-field picture. *Phys. Rev. E*, 57:6345, 1998.

[39] H. Flyvbjerg. Simplest possible self-organized criticality system. *Phys. Rev. Lett.*, 76:940, 1996.

[40] C. Hauert J. Nagler. Self-organized criticality in a nutshell. *Phys. Rev. E*, 60:2760, 1999.

[41] J. B. Johnson. Thermal agitation of electricity in conductors. *Phys. Rev.*, 32:97, 1928.

[42] H. Nyquist. Thermal agitation of electric charge in conductors. *Phys. Rev.*, 32:110, 1928.

[43] D. K. C. MacDonald. *Noise and fluctuations: an introduction*. John Wiley & Sons, 1962.

[44] S. A. Teukolsky W. H. Press, B. P. Falnnery and W. T. Vetterling. *Numerical Recipes*. Cambridge University Press, 1990.

[45] Ole Peters and Kim Christensen. Rain: Relaxations in the sky. *Phys. Rev. E*, 66:36120, 2002.

[46] P. Meakin. *Fractals, scaling and growth far from equilibrium*. Cambridge University Press, 1995.

[47] J. Sethna. Crackling noise. *Nature*, 410:242, 2001.

[48] E. J. Ding. Analytical treatment for a spring-block model. *Phys. Rev. Lett.*, 70:3627, 1993.

[49] P. Berthoud and T. Baumberger. Physical analysis of the state and rate-dependent friction law: Static friction. *Phys. Rev B*, 59:14313–14327, 1999.

[50] A. Volmer and T. Nattermann. Towards a statistical theory of dry friction. *Z. Phys. B*, 104:363–371, 1997.

[51] P.C. Hemmer M. Kloster, A. Hansen. Burst avalanches in solvable models of fibrous materials. *Phys.Rev.E*, 56:2615, 1997.

[52] J.B. Gomez Y. Moreno. Soc in a fiber-bundle-type model. *Physica A*, 274:400, 1999.

[53] Stefano Lise and Maya Paczuski. Self-organized criticality and universality in a nonconservative earthquake model. *Phys. Rev. E*, 63:036111, 2001.

[54] A. Sornette and D. Sornette. Self-organized criticality and earthquakes. *Europhys. Lett.*, 9:197, 1989.

[55] M. B. Weissman. *Rev. Mod. Phys.*, 60:537, 1988.

[56] K. Christensen H. J. Jensen and H. C. Fogedby. a. *Phys. Rev B*, 40:R7425, 1989.